AN ABSTRACT OF THE DISSERTATION OF

Andriy Zakutayev for the degree of Doctor of Philosophy in Physics presented on April 26, 2010.

Title: BaCuChF (Ch = S, Se, Te) *p*-type transparent conductors

Abstract approved: _____

Janet Tate

BaCuChF (Ch = S, Se, Te) materials are chalcogen-based transparent conductors with wide optical band gaps (2.9 – 3.5 eV) and a high concentration of free holes (10^{18} – 10^{20} cm^{-3}) caused by the presence of copper vacancies. Chalcogen vacancies compensate copper vacancies in these materials, setting the Fermi level close to the valence band maximum. BaCuChF thin film solid solutions prepared by pulsed laser deposition (PLD) have tunable properties, such as lattice constants, conductivity and optical band gaps. BaCuSF and BaCuSeF materials also feature room-temperature stable 3D excitons with spin-orbit-split levels. BaCuTeF has forbidden lowest-energy optical transitions which extends its transparency range. BaCuChF surfaces oxidize when exposed to the air, but can be protected using Ch capping layers. Polycrystalline BaCuSeF thin films have a 4.85 eV work function, a 0.11 eV hole injection barrier into ZnPc, and 0.00 eV valence band offset with ZnTe. BaCuSeF should have similar band offset and similar interfacial properties with CdTe and $Cu(InGa)Se_2$, and BaCuSF should have no valence band offset with Cu_2ZnSnS_4, according to the transitivity rule. Therefore, BaCuSeF is suitable for applications a *p*-layer in organic light-emitting diodes, *p*-*i*-*n* double-heterojunction and tandem chalcogenide solar cells.

BaCuChF (Ch = S, Se, Te) *p*-type transparent conductors

by

Andriy Zakutayev

A DISSERTATION

submitted to

Oregon State University

in partial fulfillment of
the requirements for the
degree of

Doctor of Philosophy

Presented April 26, 2010
Commencement June, 2010

Doctor of Philosophy dissertation of Andriy Zakutayev presented on April 26, 2010.

APPROVED:

_____

Major Professor, representing Physics

_____

Chair of the Department of Physics

_____

Dean of the Graduate School

I understand that my dissertation will become part of the permanent collection of Oregon State University libraries. My signature below authorizes release of my dissertation to any reader upon request.

_____

Andriy Zakutayev, Author

ACKNOWLEDGEMENTS

First I would like to acknowledge Prof. Janet Tate for being the best adviser in the World. I truly appreciate Janet's ability to give graduate students all the freedom they need to make their own mistakes and draw their own conclusions. I admire Janet's patience in dealing with my bold statements and in correcting all *a*-s and *the*-s in my writing. I would also like to thank Janet for the continuous RA support through the grants NSF DMR-0804916 and ONR N00014-07-1-0457, which gave me an opportunity to focus on research.

Second, I would like to thank my mentors: Oksana Ostroverkhova for picking me out of hundreds of candidates for the graduate program, for her teaching talents and for giving the example of how to work hard and remain energetic at the same time; David H. McIntyre for supervising my optics work; David P. Cann for introducing me to the of defects; Guenter Schneider for guiding me through the DFT defect calculations; Douglas A. Keszler for his chemical wisdom and for re-discovering BaCuChF materials that became the main topic of this work; Andreas Klein for finding me at the MRS meeting, for a SFB 595 scholarship and for everything I know about PES and band offsets; Brady J. Gibbons for sharing his experience in PLD and for his extremely friendly attitude; Henri J. F. Jansen for useful discussions on the electronic structure of the materials and on the DFT calculations. Separate acknowledgements also go to my teaching supervisors: William M. Hetherington, Chris M. Coffin and Jim E. Ketter. I would also like to acknowledge several people for providing technical support with instrumentation: John J. Donovan for help with EPMA, Sujing Xie for assistance with TEM, Ted E. Hinkey for machining and parts, Joe Magner for the electronic equipment support and Jack Rundel for the assistance with a laser-cutting tool.

Third, I would like to acknowledge help and support of many students I was fortunate to collaborate with: Robert Kykyneshi, Heather Platt, Annette Richard, Paul Newhouse, Kai Jiang, Daniel Harada, Josh Russell, Evan DeBlander, Joseph Kinney, Morgan Emerson, Cheol-Hee Park, Morgan Ferguson, Chris Dandeneau, Debra Gail, Pete Hersh, Andrew Smith, Faye Barras, Jason Vielma, Joon-Chul Moon, Dmytro

Khvostenko, David Foster, Vorranutch Jieratum, Jason Francis, Chris Reidy, and George DeBeck. Also I would like to thank my graduate classmates Denny Jackson, Landon Prisbrey and Austin Van Sickle for sharing all the joys of days and nights of the first year of the graduate program, and my xUSSR and ESA friends for pulling me out of the labs to enjoy the Nature of the Northwest.

Finally, I would like to thank all my Ukranian family, friends and mentors that shaped my character. Most importantly I thank my wife Viktoriya Olinyk for being with me and supporting me during these years.

CONTRIBUTION OF AUTHORS

Brady Gibbons helped with XRD measurements and interpretation in Chapter 2. David McIntyre assisted with the optical measurements in Chepters 2, 3 and 6. John Donovan helped with EPMA measurements and interpretation in Chapters 2, 4 and 5. Cheol-Hee Park and Heather Platt from the research group of Douglas Keszler provided the PLD targets used in Chapters 2-5. Doug Keszler originally provided the idea to work on this family of materials. Joseph Kinney contributed to early stages of work described in Chapter 3. Andreas Klein, Thomas Mayer, Wolfram Jaegermann, Alireza Barati and Corinna Hein provided help with PES experiments described in Chapters 4 and 5. Guenter Schneider assisted with DFT calculations in Chapters 2, 3 and 6, and Robert Kykyneshi helped with DFT calculations and PLD experiments in Chapters 2 and 3. Henri Jansen and David Roundy gave useful hints for DFT calculations in Chapter 6. Evan DeBlander and Morgan Emerson assisted with PLD experiments in Chapter 6. Gregory Rorrer, Debra Gail and Oksana Ostroverkhova assisted with the PL measurements and interpretation in Chapter 6. Janet Tate contributed to all aspects of this work and helped with writing of all the chapters.

TABLE OF CONTENTS

TABLE OF CONTENTS (continued)

LIST OF FIGURES

LIST OF FIGURES (continued)

LIST OF FIGURES (continued)

LIST OF TABLES

.

LIST OF APPENDIX FIGURES

To my Mom. I wish you were here.

PREFACE

The research described in this work sprang from early results of Robert Kykyneshi on development of BaCuChF thin films by pulsed laser deposition (PLD). Robert was a graduate student when I joined the group of Prof. Janet Tate and I was very encouraged by his success with thin films of these materials. Later on, I inherited a project on related BiCuOSe thin films from a Paul Newhouse, who was also a graduate student at that time. Results of the BiCuOSe project are submitted for the publication.

BaCuChF and BiCuOSe projects were never my main focus time-wise. I spent most of the time at OSU developing $SnZrCh_3$ thin films from targets prepared by Annette Richard and Daniel Harada. $SnZrCh_3$ is a very interesting narrow-bandgap material with possible ambipolar doping, but the thin films turned out to be notoriously difficult to deposit *in-situ*. The results of my $SnZrCh_3$ work ended up mostly in internal publications of the group, but bits of it will be published soon. Nevertheless, as it always happens with not-so-successful projects, I learned a lot about PLD making $SnZrCh_3$ thin films.

Along my graduate way, I contributed to several other project led by various people. In my 2nd year, I did a lot of optical characterization of solution-processes thin films (TiO_2, Nb_2O_5, "AlPO", IGZO, ZTO, IZO, HfO_2, "HafSOx", "ZircSOx") for the group of D. Keszler, sputtered thin film (IGZO, ZTO, SnO) for the group of J. Wager and sol-gel-derived ZnO for the group of B. Gibbons. In particular, the work with Kai Jiang on solution processed TiO_2 films and TiO_2/AlPO dielectric mirrors was recently published. Finally, I contributed to the work of Paul Newhouse of Cu_3TaCh_4 powders, thin films and single crystals by studying their optical properties. The results of this work are published.

In my 3rd year, I contributed to 4 projects led by others. The first project on $CuAlO_2$ single crystal was led by visiting scholars, J. C. Moon and H. L. Ju. I did the thermopower and optical measurements for this project. This results were recently published. The second project on Fe_3MS_4 (M = Si, Ge) pressed pellets led by Heather Platt. I did electrical and thermopower characterization for this project. The paper is currently in preparation for the submission. Also, I found a way to turn Kai's solution-deposited insulating TiO_2:Nb films into *n*-type transparent conductors, but the results ended up in the internal publications. Finally, I attempted to prepare thin films of new inorganic blue pigments $Y(Mn_xIn_{1-x})O_3$ discovered by A. Smith in M. Subramanian's group, but with limited success.

In my final 4th year, I was involved in several still ongoing side-projects. The first, on the development of SnS thin films and SnS-based PV devices, sprang from the $SnZrCh_3$ project. The second is on development of BaCuChF thin films on flexible substrates. The third, on development of BiCuOTe thin films, was initiated by Cheol-Hee Park, a former student and post-doc of D. Keszler, and currently a researcher at LG Chem in Korea. I wish I had more time to finish these three projects, but I hope they will become a good starting point for new graduate students in a group of Prof. Janet Tate.

Andriy Zakutayev
April 1st, 2010, Corvallis (OR), USA

CHAPTER 1

Introduction

Wide-bandgap semiconductors (also known as transparent conductors, or transparent conductive oxides (TCOs)[1]) is a class of materials that combines optical transparency with electrical conductivity. This combination of properties is rare but desirable for application in electronics.[2] Possible use of wide-bandgap (>3 eV) semiconductors includes active applications, such as channels in field-effect transistors (FETs), and passive applications, such as contacts and buffer layers in photovoltaic (PV) devices and in light-emitting devices (LEDs). The active applications are nicely described in literature,[3] so mainly the passive applications are considered below.

Both light-emitting diodes and solar cells are *p*-*n* junctions optimized for certain functionality. The most prominent examples that have been commercialized are Si PV homojunctions, CdTe/CdS PV heterojunctions, GaN homojunction LEDs, and NPB/Alq_3 heterojunction LEDs. The structure and operational principles of the homojunctions have been studied for the last 60 years, but design issues related to heterojunctions are less understood.[4]

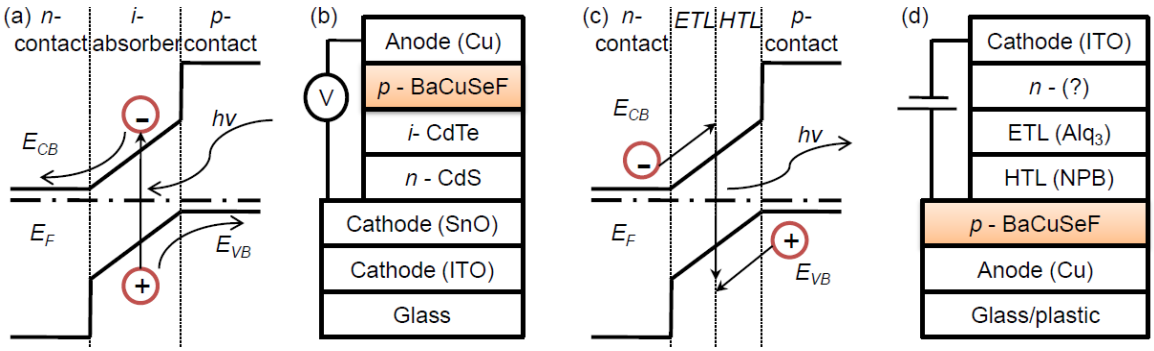

FIG. 1.1 (a and c) Band diagrams and (b and d) schematic drawings of (a and b) *p*-*i*-*n* solar cell and (c and d) organic light-emitting diode.

PV heterojunction efficiency can be improved by using a *p*-*i*-*n* solar cell design,[5] schematically shown in Fig. 1.1 (a and b). A *p*-*i*-*n* solar cell consists of a thin, almost intrinsic (*i*) narrow-bandgap semiconductor active layer sandwiched between wide-bandgap *p*-type and *n*-type passive contacts, also known as windows or membranes (Fig. 1.1a). A *p*-*i*-*n* solar cell has the following model of operation: incident light passes through a contact layer, and generates an electron-hole pair in the absorber (Fig. 1.1b). These electrons and holes move towards the *n*- and *p*-contacts due to the built-in potential

at the *i*-*n* and *i*-*p* interfaces, respectively. In reality, the structure of a *p*-*i*-*n* solar cell would involve buffer layers between the absorber and the contacts, because the ideal interface properties between them are rarely achieved

LED heterojunctions are often fabricated using organic active materials (transport layers) and inorganic passive materials (contacts), as shown in Fig. 1.1 (c and d). The simplest organic light-emitting diode (OLED) consists of active electron-transport and hole-transport layers sandwiched between the corresponding passive contacts (Fig. 1.1c). [6] An OLED has the following model of operation: electrons and holes injected from the contacts into their transport layers move towards the organic junction and recombine there, emitting a photon that escapes from the device. (Fig, 1.1d) In reality, the design of an OLED is more complicated than shown in Fig. 1.1, and often involves minority charge carrier blocking layers between the transport layers and the contacts.

Light-absorbing and light-emitting *p*-*n* junctions (PV devices and OLEDs) have a similar set of requirements for contacts:

1. At least one contact should be transparent for light to get in or out of the device. Transparency can be achieved by using a wide-bandgap semiconductor or a very thin layer of metal.

2. Both contacts should be sufficiently conductive not to limit the current. If a wide-bandgap semiconductor does not meet this requirement, it is used as a thin buffer layer in a PV device or as a thin blocking layer in OLEDs in conjunction with more conductive contacts.

3. Both contacts should reflect minority charge carriers. This requires having a large conduction band offset with an active layer for a *p*-contact, and a large valence band offset with an active layer for an *n*-contact.

4. Neither contact should affect the majority charge carrier flow. This requires having no VB offset with an active layer for a *p*-contact, or no CB offset with an active layer for an *n*-contact.

5. Contacts should not lead to formation of trap states at the interface with an active layer. For inorganic active layer in (PV devices), trap-free interfaces require either

lattice match, as found in epitaxial multi-junction solar cells, or a graded, interdiffused interface, as in CdS/CdTe heterojunctions.

6. Both contacts should be chemically compatible with the active layer and not cause its deterioration over time. Examples of poor compatibility are CdTe PV devices with Cu contacts, and OLEDs with In_2O_3 contacts.

There is a lack of wide-bandgap semiconductors that meet all these criteria. Therefore, high-workfunction metals are often used as *p*-contacts in PV devices, such as Au (5.10 eV) and Cu (4.65 eV) to CdTe, Mo (4.6 eV) to CIGS and CZTS. For the same reason, low-work-function metals are used as *n*-contacts in OLEDs, such as Ba (2.7 eV) and Ca (2.9 eV) to Alq_3. The list of work functions of different metals can be found in reference books.[7] Clearly, these metals do not meet many of the aforementioned requirements for contact applications.

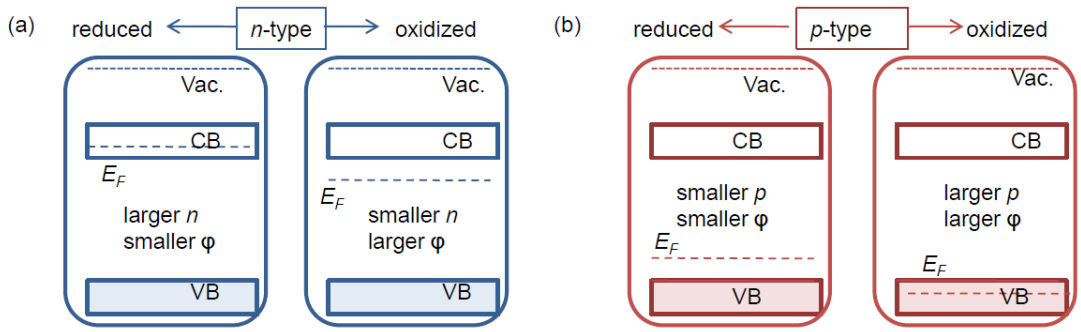

FIG. 1.2 Modulation of the Fermi level in (a) *n*-type and (b) *p*-type semiconductors

An additional advantage of using wide-bandgap semiconductors for contact applications is the possibility to tune their work functions and thereby affect the conductivity and the band lineup. Examples of hypothetical wide-bandgap *n*-type and *p*-type semiconductors are shown in Fig. 1.2. In an *n*-type semiconductor, decrease of the work function causes an increase in the concentration of electrons and hence the conductivity (Fig. 1.2a). Both low work function and low conductivity are favorable for *n*-type contact applications. In a *p*-type semiconductor, increase of the work function causes an increase in the concentration of holes and hence the conductivity (Fig. 1.2b). Both high work function and low conductivity are favorable for p-type contact

applications. These considerations lead to the trivial conclusion that *p*-contacts should be made of appropriate *p*-type semiconductors, and *n*-contacts should be made of appropriate *n*-type semiconductors. Nevertheless, *n*-type TCOs are conventionally used as *p*-type contact in OLEDs.

Often, it is difficult to change the work function of a wide-bandgap semiconductor by doping,[8] so oxidation/reduction surface treatments are used.[9] This however, alters the chemical composition of the surface,[10] and may lead to long-term degradation of optoelectronic devices.[11]

The difficulty in doping wide-bandgap materials is often caused by Fermi level pinning. If the Fermi level cannot be changed over a wide enough range by applying an electric field, the channel of a field effect transistor cannot be turned on and off. Therefore, the possibility of large Fermi level modulation is the main requirement for use of wide-bandgap semiconductors in transparent FETs. The next two requirements are large band discontinuities between the channel and the gate electrode to avoid the leakage current. The remaining requirements are similar to the six requirements listed above for passive applications: the channel material has to be transparent, non-reactive, must have no interfacial states, and have a proper band lineup with the source and drain electrodes.

This work is focused on a family of wide-bandgap *p*-type semiconductors BaCuChF (Ch = S, Se, Te).[12] BaCuSF and BaCuSeF materials were discovered by Zhu et. al. in 1994.[13] More recently, the center of studies of these materials moved to Oregon State University (OSU). Yanagi *et. al.* reported synthesis of BaCuSF and BaCuSeF pressed pellets,[14] valence band structure of these materials,[15] and *ex-situ* processed BaCuSF thin films.[16] Park *et. al.* synthesized BaCuTeF,[17] and showed that the bandgap of these materials in powder form can be modulated.[18] Kykyneshi *et. al.* deposited epitaxial thin films of BaCuTeF,[19] and Spies *et.al.* assessed application of this materials in solar cells.[20] Besides the research efforts at OSU, Ba-Cu-S-F powders and thin films of a questionable phase were reported by Frantz et.al.[21] Powders of related SrCuChF materials were reported by Kabbour et.al.,[22] and Yanagi et.al.[23] Finally, a whole body of work by the group of H. Hosono exists on isostructural LaCuOCh wide-bandgap *p*-type semiconductor,[24] and iron-based high-temperature superconductors LaFeOAs.[25]

One goal of this work is to evaluate the possibility of application of BaCuChF materials in electronic devices. To achieve this goal, relevant physical properties of BaCuChF were studied and compared to the aforementioned requirements for applications. Another goal is to investigate fundamental physical properties of BaCuChF wide-bandgap *p*-type semiconductors and understand the origin of the change of different properties in the S-Se-Te series. Research presented in this work resulted in five new publications on BaCuChF materials, each of which constitutes one chapter of this work. BaCuChF thin films prepared by pulsed laser deposition are suitable for application as *p*-contact in PV devices and OLEDs because they have wide band gaps, tunable optical and electrical transport properties,[26] and form good contact to organic[27] and inorganic[28] semiconductors used in optoelectronic devices. In addition, BaCuChF have some rare and interesting fundamental physical properties, such as spin-orbit-split room-temperature excitons in BaCuSF and BaCuSeF, and forbidden lowest-energy optical transitions in BaCuTeF.[29] According to the results of density functional theory defect calculations, BaCuChF materials are not suitable for *p*-channel applications in TFETs due to a high concentration of free holes and narrow Fermi level pinning range caused by the presence of defects.[30] This work also includes five appendices that describe in more detail the methods used to complete this work, such as pulsed laser depositon, thin film post-processing, experimental characterization techniques, photoemission spectroscopy methods and density functional theory defect calculations, and address their availability for the users at Oregon State University.

References

[1] For a review see MRS bsulletin, August 2000

[2] C. G. Granqvist, Sol. Energy Mater. Sol. Cells **91**, 1529 (2007).

[3] J. F. Wager, D. A. Keszler, and R. E. Presley, *Transparent Electronics* (Springer, 2007).

[4] A. Luque and S. Hegedus, *Handbook of Photovoltaic Science and Engineering* (John Wiley and Sons, 2003).

[5] W. Jaegermann, A. Klein, and T. Mayer, Adv. Mater. **21**, 4196 (2009).

[6] L. S. Hung and C. H. Chen, Mater. Sci. Eng. R **39**, 143 (2002).

[7] D.R. Lide, *CRC Handbook of Chemistry and Physics* (CRC Press, 2004).

[8] S. Lany, J. Osorio-Guilln, and A. Zunger, Phys. Rev. B **75**, 241203 (2007).

[9] Z. Z. You and J. Y. Dong, Appl. Surf. Sci. **249**, 271 (2005).

[10] H. Hiramatsu, I. Koizumi, K.-B. Kim, H. Yanagi, T. Kamiya, M. Hirano, N. Matsunami, and H. Hosono, J. Appl. Phys. **104**, 113723 (2008).

[11] Y. Gassenbauer and A. Klein, J. Phys. Chem. B **110**, 4793 (2006).

[12] J Tate, P. F. Newhouse, R. Kykyneshi, P. A. Hersh, J. Kinney, D. H. McIntyre, and D. A. Keszler, Thin Solid Films **516**, 5795 (2008).

[13] W. J. Zhu, Y. Z. Huang, F. Wu, C. Dong, H. Chen, and Z. X. Zhao, Mater. Res. Bull. **29**, 505 (1994).

[14] H. Yanagi, J. Tate, S. Park, C.-H. Park, and D. A. Keszler, Appl. Phys. Lett. **82**, 2814 (2003).

[15] H. Yanagi, J. Tate, S. Park, C.-H. Park, D. A. Keszler, M. Hirano, and H. Hosono, J. Appl. Phys. **100**, 083705 (2006).

[16] H. Yanagi, S. Park, A. D. Draeseke, D. A. Keszler, and J. Tate, J. Solid State Chem. **175**, 34 (2003).

[17] C.-H. Park, R. Kykyneshi, A. Yokochi, J. Tate, and D. A. Keszler, J. Solid State Chem. **180**, 1672 (2007).

[18] C.-H. Park, D. A. Keszler, H. Yanagi, and J. Tate, Thin Solid Films **445**, 288 (2003).

[19] R. Kykyneshi, D. H. McIntyre, J. Tate, C.-H. Park, and D. A. Keszler, Solid State Sci. **10**, 921 (2008).

[20] J. A. Spies, R. Schafer, J. F. Wager, P. Hersh, H. A. S. Platt, D. A. Keszler, G. Schneider, R. Kykyneshi, J. Tate, X. Liu, A. D. Compaan, and W. N. Shafarman, Sol. Energy Mater. Sol. Cells **93**, 1296 (2009).

[21] J. A. Frantz, J. S. Sanghera, V. Q. Nguyen, S. S. Bayya, S. B. Qadri, and I. D. Aggarwal, Mater. Lett. **62**, 1582 (2008).

[22] H. Kabbour, L. Cario, S. Jobic, and B. Corraze, J. Mater. Chem. **16**, 4165 (2006).

[23] E. Motomitsu, H. Yanagi, T. Kamiya, M. Hirano, and H. Hosono, J. Solid State Chem. **179**, 1668 (2006).

[24] K. Ueda, H. Hiramatsu, M. Hirano, T. Kamiya, and H. Hosono, Thin Solid Films **496**, 8 (2006).

[25] K Ishida, Y Nakai, and H Hosono, J. Phys. Soc. Jpn. **78**, (2009).

[26] A. Zakutayev, D. H. McIntyre, G. Schneider, R. Kykyneshi, D. A. Keszler, C-H. Park, and J. Tate, Thin Solid Films (2010), in press

[27] A. Zakutayev, J. Tate, H. A. S. Platt, D. A. Keszler, C. Hein, T. Mayer, Andreas Klein, Wolfram Jaegermann, J. Appl. Phys., (2010) in press

[28] A. Zakutayev, J. Tate, H.A. S. Platt, D. A. Keszler, A. Barati, A. Klein, W. Jaegermann, Appl. Phys. Lett., (2010) in press

[29] A. Zakutayev, R. Kykyneshi, G. Schneider, D. H. McIntyre and J. Tate, Phys. Rev. B. (2010), in press

[30] A. Zakutayev, J. Tate, G. Schneider, in preparation

CHAPTER 2

Tunable properties of wide-bandgap *p*-type $BaCu(Ch_{1-x}Ch'_x)F$ (Ch = S, Se, Te) thin film solid solutions

A. Zakutayev, D. H. McIntyre, G. Schneider, R. Kykyneshi, D. A. Keszler, C-H. Park, and J. Tate

Accepted to Thin Solid Films

2.1 Introduction

Transparent *p*-type semiconductors constitute a class of materials in which hole conductivity coexists with optical transparency, a combination useful for optoelectronic applications. In photovoltaics (PV), realization of *p*-*i*-*n* double heterojunction solar cells with CdTe or Cu(InGa)$(SSe)_2$ intrinsic (*i*) absorbers depends on the development of a highly doped, *p*-type, wide band gap window layer with an appropriate ionization potential.[1] Besides these requirements, an ideal anode layer for *p*-*i*-*n* chalcogenide thin film solar cells should be able to form interdiffused, graded interfaces with the absorber.[2] Other types of thin film photovoltaic devices, such as tandem and multi-junction solar cells, would also require a *p*-type transparent semiconductor. *P*-type transparent semiconductors are also useful for organic light-emitting diodes (OLEDs). Sn:In_2O_3 (ITO), an *n*-type transparent conductive oxide (TCO), is usually used as the transparent anode in OLEDs. *P*-type wide bandgap materials typically have higher work functions than their *n*-type counterparts and thus are suited better for hole-injection in OLEDs. Insertion of a *p*-type layer between an *n*-type TCO and organic layers can improve performance by reducing the operating voltage of OLEDs.[3] Replacement of the *n*-type anode with a single transparent conductive *p*-type layer is also beneficial. Threshold voltage and current density are improved by using *p*-type transparent LaCuOSe:Mg instead of ITO.[4] A *p*-type transparent conductor will be of commercial interest for OLEDs if it does not contain rare and expensive elements such as In.

High hole conductivity is not easy to achieve in wide-gap binary oxides. For example, there are many reports on *p*-type doped ZnO, but the reproducibility and long-term stability is challenging.[5] The valence band of most binary oxides is derived from deep, localized oxygen 2*p* states, which results in low mobility of the holes if *p*-type conductivity can be achieved. A few binaries, such as NiO, Cu_2O and SnO, have broader valence bands, partially derived from the cation atomic orbitals. These materials have been demonstrated as functional *p*-type layers,[6] but their band gaps are not large enough for high transparency over the whole visible range. Cu-based mixed-cation ternaries offer a means to increase the transparency of *p*-type oxide semiconductors.[7] In these materials, Cu *d* states hybridize with O *p* levels, which broadens the valence band. Numerous

reports on Cu-based ternary oxides of $CuMO_2$ (M = Al, Ga, In, Cr, Sr, Ba, Y, Sc *etc*.) and $AeCu_2O_2$ (Ae = Ba, Sr, Mg, Ca) structures are found in the literature.[8] The ternaries usually have better transparency than the binaries, but transport properties of the two groups of materials are similar.

Chalcogenides (sulfides, selenides and tellurides) offer another prospect for simultaneous high transparency and conductivity. The *p*-levels of the chalcogen atoms are higher than oxygen *p*-states, and hybridize better with some cation levels, which results in broader valence bands and more stable *p*-type conductivity.[9] Well-known *p*-type chalcogenides are based on monovalent copper, such as $Cu_{2-x}Ch$ (Ch = S, Se, Te), but these simple binaries have too narrow a band gap to be considered transparent. Ternary Cu-based *p*-type chalcogenides, such as $BaCu_2Ch_2$, have wider bandgaps, but they are still somewhat colored.[10] Only quaternary Cu-based mixed-anion chalcogenides, such as chalcogeno-fluorides BaCuChF (Ch=S, Se, Te)[11] and oxy-chalcogenides LnCuOCh (Ln = La, Pr, Nd)[12] have bandgaps wide enough to be considered fully transparent. The increased band gap results from a weakening of Cu-Cu interactions due to the layered crystal structure with covalent Cu-Ch sheets stacked along the crystallographic *c*-axis alternating with ionic Ba-F or Ln-O layers. (Fig. 2.1a). The chalcogenide-fluorides discussed in this paper show high native concentration of holes (10^{18}-10^{20} cm^{-3}) with reasonable mobilities (up to 10 cm^2/Vs in the epitaxial thin film form).[13]

An advantage of chalcogenides over oxides is tunability of their physical properties. For example, the chalcogen content of II-VI semiconductors can be continuously tuned from S through Se to Te, which changes the electronic structure, the band gap and related properties over the entire range. Similar tunability is characteristic for pnictides (for example III-V semiconductors III = Al, Ga, In, V = N, P, As, Sb). Oxides do not feature this ready tunability, although, for example, the band gap of (Zn,Mg)O thin film solid solutions can be tuned from 3.6 eV to 4.2 eV in the wurtzite $(Zn_{1-x}Mg_x)O$ crystal structure with up to 34 at. % Mg, and from 7.8 eV to 6.7 eV in the rock-salt $(Mg_{1-y}Zn_y)O$ crystal structure with up to 18 at. % Zn.[14] The limited tunability of oxides is unfortunate, because generally oxides are much more robust than chalcogenides

and pnictides, which is a big advantage in applications and processing. Quaternary mixed-anion compounds are often layered, which offers an additional degree of freedom for finding diverse physical properties. It is possible to replace a whole layer with another, preserving the total charge, for example replacing the Ln-O layer with a Ba-F layer or replacing the Cu-Ch layer with an Fe-As layer (Fig. 2.1a). This flexibility results in large chemical diversity of layered mixed-anion compounds, which resulted in the discovery of Fe-As-based high-temperature superconductors .[15]

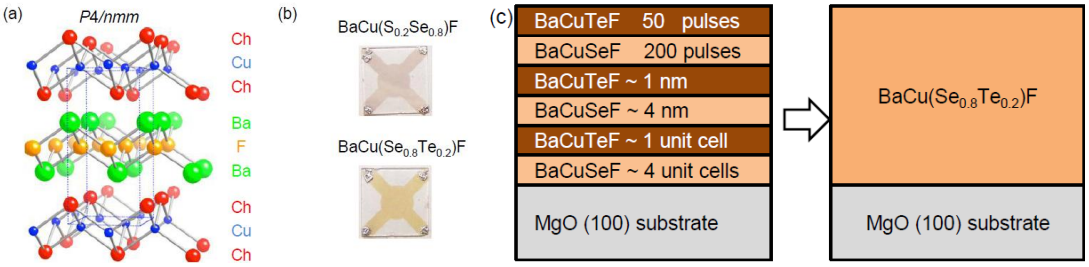

FIG. 2.1. (a) Crystal structure of BaCuChF, (b) photographs of the $BaCu(Ch_{1-x}Ch'_x)F$ thin films, (c) alternating pulsed laser deposition technique.

Many copper-based chalcogenides exhibit *p*-type conductivity without intentional doping. Controllable extrinsic *p*-type doping of these materials is desirable but challenging. K-doping in Ba-Cu-based chalcogeno-fluorides improves the conductivity of bulk pellets, but is more difficult to realize for thin films.[16] Degenerate hole concentration has been observed in ultra-thin Mg-doped La-Cu-based oxy-chalcogenides films, but the degeneracy is attributed to Cu vacancies.[17] An alternative to the extrinsic doping approach to control the electrical properties of *p*-type transparent chalcogen-based semiconductors is to use the differences in the native defect chemistry of sulfides, selenides and tellurides to control the conductivity. This concept is implemented by *in-situ* alloying of different BaCuChF materials with each other in a thin film form.

In this paper we describe a preparation technique for $BaCu(Ch_{1-x}Ch'_x)F$ thin film solid solutions, report on their structural, optical and electrical transport properties, and discuss the results of the density functional theory calculations. The resulting solid solutions show a conductivity change of more than three orders of magnitude. This is moderate compared to the potential of conventional extrinsic doping, but it is an

important step towards understanding doping of such thin films. Formation of thin film solid solutions also offers the ability to tune the unit cell and band gap, which are relevant to optoelectronic applications.

2.2 Methods

BaCuChF thin films were prepared by pulsed laser deposition (PLD) from pre-polished, pre-ablated, phase-pure BaCuChF targets. A 248-nm KrF excimer laser operating at 1 J/cm^2 (quite typical for chalcogenides as opposed to oxides where the laser beam intensity is usually higher) at repetition rates between 3 and 7 Hz was used for the deposition. Thin films were grown on amorphous silica (*a*-SiO_2) and (100)-cut single crystal magnesium oxide (MgO) substrates. Prior to deposition, the substrates were cleaned in an ultrasonic bath for a total of 30 min. The films were patterned for electrical measurements using the Hall cross mask (Fig. 2.1b).

$BaCu(Ch_{1-x}Ch'_x)F$ thin film solid solutions were prepared by PLD of alternating layers of ultra-thin BaCuChF films (Fig. 2.1c) at elevated substrate temperature. Each layer thickness was typically less than 10 nm or less than 10 unit cells and the total film thickness was typically 150 nm. A similar layering technique was used for room temperature deposition of LaCuOS-LaCuOSe multilayered stacks in the *ex-situ* processing of $LaCuO(S_{1-x}Se_x)$ solid solutions by reactive solid-phase epitaxy.[18] In this work, $BaCu(Ch_{1-x}Ch'_x)F$ thin film solid solutions were prepared in a one-step process *in-situ* deposition on heated substrates. $BaCu(Se_{-x}Te_x)F$ films were deposited at 600 ˚C and a 6.5-cm target-substrate distance in an Ar atmosphere (0.133 Pa). Films in the $BaCu(S_{1-x}Se_x)F$ series were deposited at a substrate temperature of 400 ˚C in ultra-high vacuum (~0.133 x 10^{-4} Pa during the deposition) using a 5-cm target-substrate distance. These conditions minimized the loss of sulfur, a common problem for this process. After the deposition, the samples were cooled to room temperature at 10 ˚C/min. The base pressure in PLD chamber at room temperature before deposition was 3×10^{-7} Pa.

The stoichiometry of the thin films was investigated using Cameca-50 electron probe microanalysis (EPMA) at three different electron accelerating voltages: 10, 15 and 20 kV. For this study, samples were coated with a 5-nm layer of graphite to prevent

possible charging of the films. The EPMA data were analyzed using MicroProbe and Stratagem software; the estimated statistical accuracy was 1%.

X-ray diffraction (XRD) analysis of the films on MgO in the range $2\theta = 5 - 65^{o}$ was performed on a Rigaku MiniFlex and Bruker AXS D8 diffractometers using Cu K_{α} radiation. The *c*-axis lattice parameter was carefully determined from the positions of all observed XRD peaks using the $\cos^2(\theta)$ extrapolation function.[19] θ-2θ XRD patterns of the films on *a*-SiO_2 were measured on Rigaku Rapid diffractometer in grazing incidence configuration. The surface of the films was imaged using multimode atomic force microscopy (AFM) in contact mode. The AFM data were plotted and analyzed using Nanoscope software.

Optical measurements were performed using a custom-built spectrometer with a Xe discharge lamp source, double-grating monochromator and Si detector connected to a powermeter. The monochromator was calibrated using a HeNe laser. The absorption coefficient α was calculated from the measured transmitted (I_{trans}) and reflected (I_{refl}) light intensities using $\alpha = - \ln(T/(1-R))/d$, where $T = I_{trans}/I_{inc}$ is transmittance and $R = I_{refl}/I_{inc}$ is reflectance of the sample. The thickness *d* and refractive index *n* of the thin films were obtained by numerical least squares fitting of the model to the experimental interference pattern, not taking into account the effects of roughness of the films.

The conductivity and the Hall coefficient of the films were measured at room temperature in the van der Pauw configuration, using a Lakeshore 7504 Hall system. Contacts to the films were formed by low-temperature soldering of In. The Ohmic nature of all contacts was confirmed by two-probe current-voltage measurements. The sign of the Hall coefficient for both directions of the magnetic field was positive.

BaCuSF, BaCuSeF, and BaCuTeF were studied using the Perdew-Burke-Ernzerhof (PBE) generalized gradient approximation (GGA) and the local density approximation (LDA) of density functional theory (DFT). The projector augmented wave (PAW) method as implemented in VASP[20] with an energy cutoff of 400 eV and an 8 x 8 x 4 Monkhorst-Pack grid for *k*-space integration was used. Internal coordinates and cell shape were fully optimized in each calculation. Calculated total energies as a function of volume were fitted to the Murnaghan equation of state[21] to obtain equilibrium lattice

parameters. Directional effective masses were calculated by fitting a parabola to the energy dispersion relation.

2.3 Results and discussion

In-situ growth of phase-pure BaCuTeF epitaxial and polycrystalline thin films has been previously reported.[13] BaCuTeF thin films align out-of-plane and in-plane with a (100) MgO substrate. It has not been possible to obtain full out-of-plane and in-plane alignment of BaCuSeF samples on the MgO substrates under the deposition conditions used for BaCuTeF growth.[11] The heteroepitaxy of BaCuSeF thin films reported here resulted from reducing the deposition rate by decreasing the repetition rate of the laser from 7 to 3 Hz. The θ-2θ XRD pattern of a representative BaCuSeF thin film on MgO substrate shows only (00*l*) peaks (Fig. 2.2a), which indicates its full out-of-plane (*c*-axis) alignment with the MgO substrate. In-plane alignment is confirmed by a φ-scan (Fig. 2.2a inset). The ω-scan full width at half-maximum of the (003) peak is 1.1°.

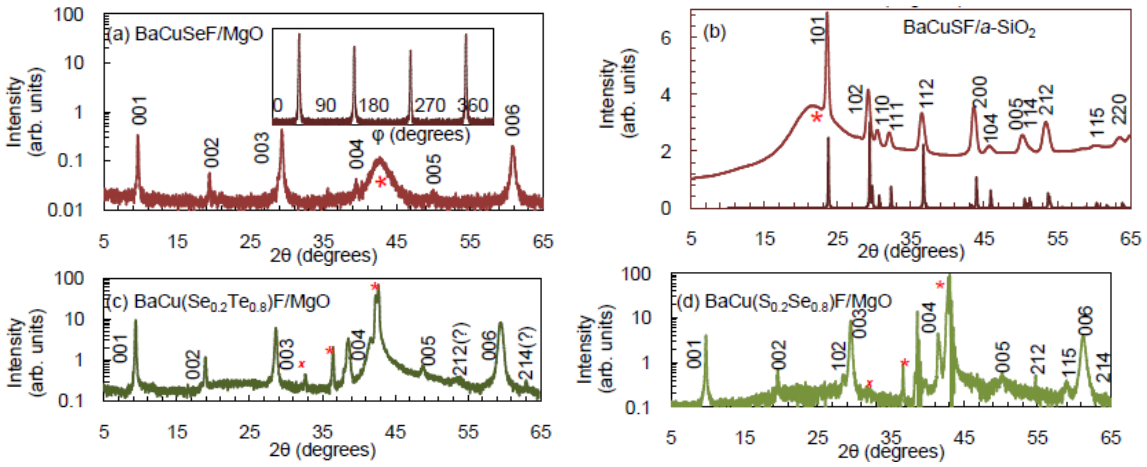

FIG. 2.2. XRD θ-2θ pattern of BaCuSeF (a), BaCuSF (b), BaCu($Se_{1-x}Te_x$)F (c) and BaCu($S_{1-x}Se_x$)F thin films. The stars and crosses indicate substrate and a substrate holder peaks. Inset (a): XRD φ-scan of BaCuSeF thin film on MgO.

BaCuSF films are even more difficult to deposit, and previously we have had to use an *ex-situ* anneal to prepare the samples with single-phase XRD patterns. However, by keeping the substrate temperature below 400 ˚C and reducing target-substrate distance

to 5 cm we have prepared phase-pure BaCuSF thin films *in-situ*, without post-processing (Fig. 2.2b). Nevertheless, full epitaxy of BaCuSF on MgO remains challenging. We attribute this difficulty to the 400 ˚C upper limit imposed on substrate temperature by the high volatility of sulfur.

The optimal conditions discussed above were used to prepare $BaCu(Se_{1-x}Te_x)F$ and $BaCu(S_{1-x}Se_x)F$ thin film solid solutions by depositing alternating ultra-thin layers of the constituents on MgO substrates. XRD indicates that the $BaCu(Ch_{1-x}Ch'_x)F$ films are predominantly *c*-axis oriented with no signs of the original layering. Thin films deposited at 600 ˚C, for example $BaCu(Se_{0.2}Te_{0.8})F$, show only (00*l*) x-ray diffraction peaks (Fig. 2.2c). Films deposited at 400^{o}C, for example $BaCu(S_{0.2}Se_{0.8})F$, are also textured (Fig. 2.2d), but the degree of *c*-axis orientation is smaller, since non-(00*l*) XRD peaks are also observed.

High substrate temperature, large kinetic energy of the species in the plume, and fine layering during the alternating PLD facilitate the interdiffusion of the layers and the formation of the solid solutions. Higher substrate temperature results in increased diffusion of the chalcogen atoms, while the high kinetic energy of the species may cause them to implant in the surface of the growing film.[22] The energy of the species impinging on the substrate can be controlled by changing the pressure in the chamber during the process (0.133 Pa of Ar for $BaCu(Se_{1-x}Te_x)F$ and 0.133 x 10^{-4} Pa base pressure during $BaCu(S_{1-x}Se_x)F$ deposition). We found that the formation of single-phase solid solutions results either from the combination of higher substrate temperature (600 ^{o}C) with a lower energy of the impinging species for Te-containing thin films, or from the combination of lower substrate temperature (400 ^{o}C) with a higher energy of the impinging species for S-containing thin films. Fine layering also facilitates good mixing due to bulk interdiffusion. Finally, in both series, the thickness of the layer that results from one deposition cycle (< 10nm) is comparable with the surface roughness of the film after the deposition (3 nm), which may promote intermixing at least during the later stages of the film growth. According to the EPMA results, the molar ratio *x* of heavy chalcogen to the total chalcogen content agrees well with the ratio of the number of laser pulses in corresponding BaCuChF targets during alternating pulsed laser deposition. For example,

a $BaCu(S_{0.2}Se_{0.8})F$ thin film prepared by 10 cycles of alternating PLD (50 pulses from the BaCuSeF target and 200 pulses from the BaCuSF target) has a Se content of $x = 0.79 \pm 0.01$.

We used atomic force microscopy (AFM) to evaluate the surface quality and identify the growth mode of the $BaCu(Ch_{1-x}Ch'_x)F$ films. $BaCu(Ch_{1-x}Ch'_x)F$ thin films are relatively smooth on the submicron scale (Fig. 2.3). Submicron-sized particles were found on larger scale images, a common disadvantage of the PLD method. A 160 nm-thin film of $BaCu(Se_{0.5}Te_{0.5})F$ composition has a 3 nm root-mean-square roughness, which corresponds to about 3 *c*-axis lattice parameters of the BaCuChF crystal structure or about 2% of the total thickness of the film. This roughness may lead to large number of surface states. Hence, the transport properties reported here may not be optimal and there is room for further improvement of the quality of the films. 100-nm-sized grains can be observed in the top-view (Fig. 2.3a) and surface cross-sectional (Fig. 2.3b) AFM images. This observation suggests that $BaCu(Ch_{1-x}Ch'_x)F$ thin film solid solutions on MgO substrates grow in either Volmer-Weber or Stransky-Krastanov mode.[22]

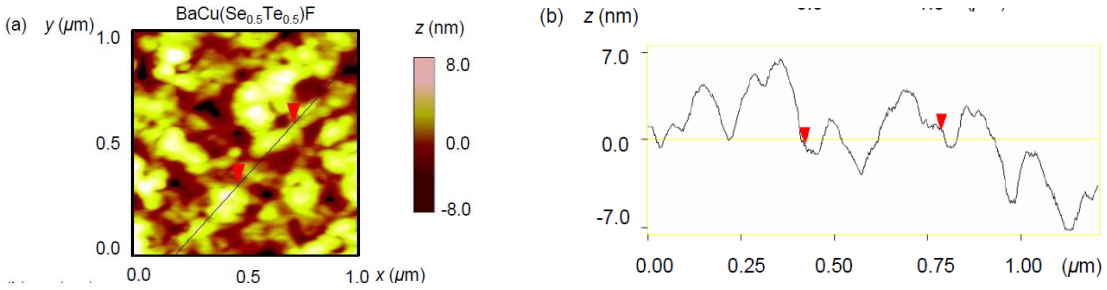

FIG. 2.3. AFM top-view (a) and surface cross-section (b) image of a $BaCu(Se_{0.5}Te_{0.5})F$ thin film.

We compared the theoretical unit-cell parameters obtained using DFT with those extracted from XRD patterns of $BaCu(Ch_{1-x}Ch'_x)F$ powders and thin films. We reported previously that for powder solid solutions,[23] the experimental *a*-axis lattice parameter and volume of the unit cell *V* increase with increasing atomic radius of chalcogen, according to Vegard's law. Results of our present calculation show that on average, LDA DFT underestimates *a* by 2.4% and GGA DFT overestimates *a* by 0.7% (Fig. 2.4a). The sign

and the magnitude of these discrepancies are typical for the calculations of materials lattice parameters using these approximations. The LDA and GGA uncertainties are the same (0.7%) for dimensionless unit cell anisotropy *c/a* (Fig. 2.4b). Overall, reasonable agreement between experimental and theoretical results demonstrates that the unit cell size of $BaCu(Ch_{1-x}Ch'_x)F$ thin film solid solution can be tuned by alternating deposition from different BaCuChF targets.

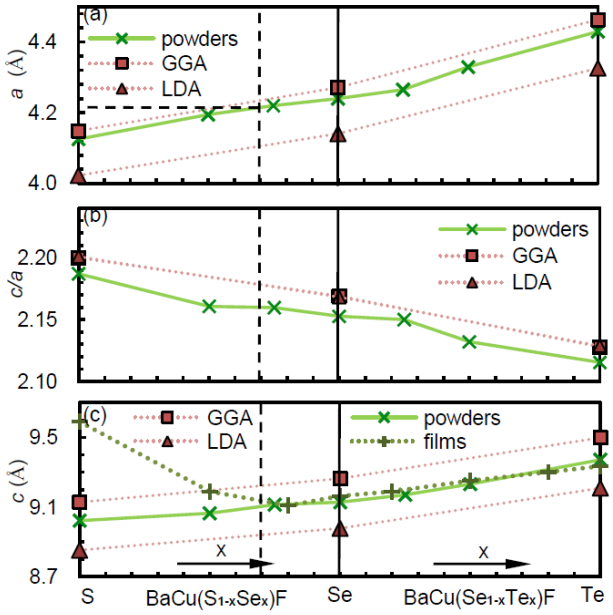

FIG. 2.4. Lattice parameters of $BaCu(Ch_{1-x}Ch'_x)F$. The lines are guides to the eye. At the composition $BaCuS_{0.3}Se_{0.7}F$, the *a*-axis lattice parameter is exactly matched to that of MgO; this is indicated by the vertical dashed line.

In all BaCuChF powders and Te-containing thin film solid solutions the experimental *c*-axis lattice parameter obeys Vegard's law,[23, 24] but S-containing thin film solid solutions do not show the same linear trend (Fig. 2.4c). Rather, BaCuSF thin films have a reproducibly larger *c*-axis lattice parameter than BaCuSeF thin films. The difference between the thin film and the powder BaCuSF *c*-axis lattice parameter is $\delta c = (c_f - c_p)/c_p = 0.064$ where c_f and c_p are *c*-axis lattice constants of the films and powders respectively. The *a*-axis lattice parameter of the powder BaCuSF is smaller than that of MgO and the mismatch is $\mu = (a_p - a_s)/a_s = -0.021$, where a_p and a_s are *a*-axis lattice

constants of powder BaCuSF and MgO respectively. Other S-containing solid solutions that were grown at 400 ˚C show the same, but weaker effect (δc = 0.014, μ = -0.004 for $BaCu(S_{0.5}Se_{0.5})F$). This effect is almost negligible in the $BaCu(Se_{1-x}Te_x)F$ series (δc = +0.004, μ = +0.007 for BaCuSeF and δc = -0.004, μ = +0.052 for BaCuTeF).

One explanation for the increase in the *c*-axis lattice parameter of BaCuSF thin films on MgO substrates compared to powders is the presence of anion vacancies. Similar effect attributed to oxygen deficiency is observed in oxides grown in energetic deposition environments such as radio frequency sputtering[25] and pulsed laser deposition.[26] The anion deficiency may lead to increased cation repulsion and therefore larger lattice parameters. The absence of a *c*-axis lattice expansion in the $BaCu(Se_{1-x}Te_x)F$ film series, points to a sulfur deficiency rather than a fluorine deficiency. Also, elemental sulfur has a much higher vapor pressure compared to selenium and tellurium and thus is more likely to be lost in the course of deposition.

An additional possible contribution to the observed *c*-axis lattice expansion in BaCuSF thin films is the micro-strain developed due to the low growth temperature (400 ˚C) and large negative mismatch μ between the BaCuSF and MgO *a*-axis lattice parameters. From a thermodynamic equilibrium standpoint, low substrate temperatures should result in a lower density of bulk point defects and hence less chance for the strain to relax through dislocations. In addition it is easier to achieve thin film growth under tensile micro-strain due to the asymmetry in the repulsive potential between atoms.[27] In contrast, the high growth temperature (600 ^{o}C) and compressive nature of the micro-strain would cause almost no *c*-axis lattice expansion in BaCuTeF thin films. However, this micro-strain argument is most likely not dominant in BaCuChF thin films. First, it is known that coherently-strained epitaxial films can be grown only to a certain critical thickness before relaxation occurs[28] and the thickness of our films (~150 nm) is much larger than a typical critical thickness (10 – 30 nm). Second, thin film deposition is usually governed by kinetic phenomena and not thermodynamic equilibrium. We also note that the thermal expansion mismatch between the substrates and films may induce macro-strain, but at present there are no thermal expansion data for BaCuChF.

The results of a typical optical measurement on $BaCu(Ch_{1-x}Ch'_x)F$ thin film solid solutions are shown in Fig. 2.5a. The $BaCu(Se_{0.8}Te_{0.2})F$ thin film is transparent to most of the visible spectrum. The modulation of the transmittance and reflectance above 400 nm is due to the interference of the light reflected from the surfaces of the 145-nm film. The interference fringes are eliminated in the normalized reflection-corrected transmittance $T/(1-R)$, which translates into the featureless absorbance of $BaCu(Ch_{1-x}Ch'_x)F$ thin films below the absorption edge, indicated by arrows in Fig. 2.5b. $BaCu(Se_{1-x}Te_x)F$ thin film solid solutions have weak near-edge absorption, and look slightly colored. The absorption edge changes monotonically with x in $BaCu(Ch_{1-x}Ch'_x)F$ thin films (Fig. 2.6a). This tunability is desirable for engineering of OLEDs and chalcogenide thin film solar cells that might contain BaCuChF.[29, 30]

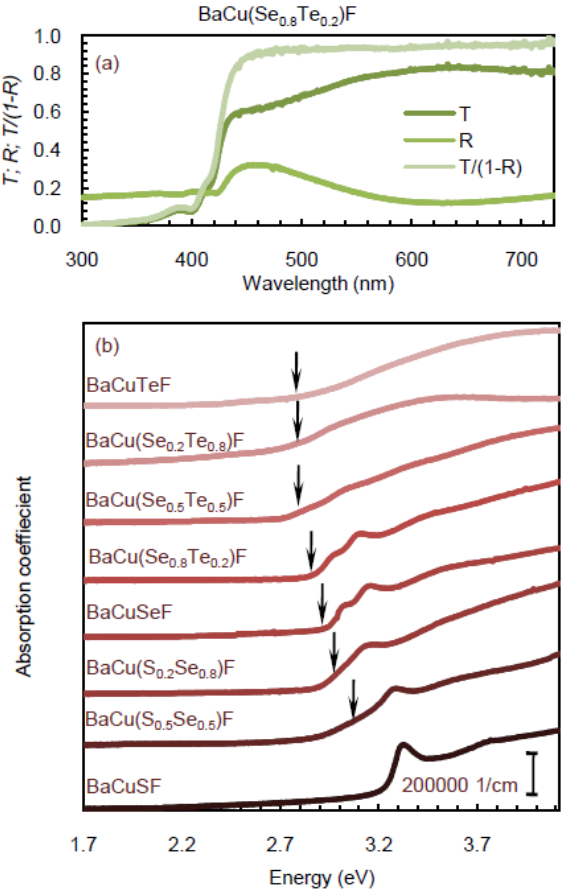

FIG. 2.5. (a) Optical transmittance T, reflectance R and normalized transmittance $T/(1-R)$ of the $BaCu(Se_{0.8}Te_{0.2})F$ thin film. (b) Optical absorption spectra of $BaCu(Ch_{1-x}Ch'_x)F$ thin films. The curves are offset for clarity.

In BaCuChF we distinguish between the energy of the absorption edge (onset of strong absorption) and the band gap, because of the presence of high-binding energy excitons, or bound electron-hole pairs, also observed in other layered mixed-anion compounds.[12] Two excitonic peaks are present in the absorption spectra of all $BaCu(Ch_{1-x}Ch'_x)F$ thin-film solid solutions that contain less than 50% of Te on the Ch site (Fig. 2.5b). Details of the optical properties will be discussed in a separate publication,[31] but briefly, we attribute the absence of excitonic peaks from the absorption spectra of $BaCu(Se_{1-x}Te_x)F$ films that contain more than 50% Te on the Ch-site to screening of the excitonic electrostatic interaction by free holes. Right above the absorption edge, $BaCu(S_{1-x}Se_x)F$ thin film solid solutions also show a much larger (~10^5 cm^{-1}) absorption coefficient than Te-containing thin films. The high absorption coefficients are attributed to the direct nature of the lowest optical transitions along with the Coulomb-enhancement effect.[32]

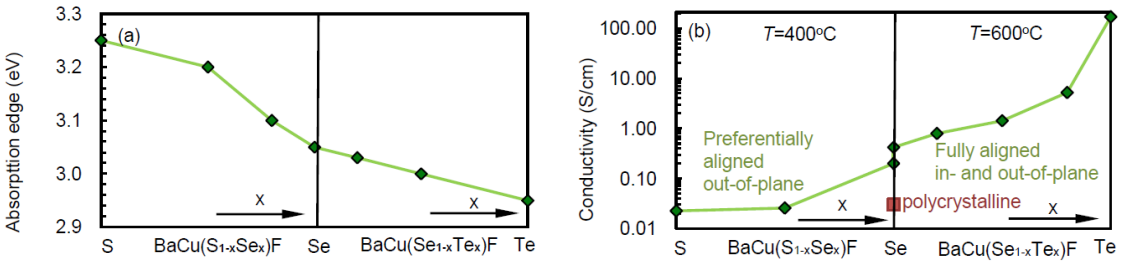

FIG. 2.6. Absorption edge (a) and conductivity (b) of $BaCu(Ch_{1-x}Ch'_x)F$ thin film solid solutions.

The transport properties of BaCuChF thin films are influenced by their alignment with the substrate. The out-of-plane (*c*-axis) orientation with MgO substrate has a strong effect on the conductivity of BaCuChF thin films. Deposited under otherwise identical conditions, *c*-axis oriented thin films on MgO substrates have larger conductivity by a factor of 20 than randomly oriented BaCuSeF films on amorphous silica substrates (Fig. 2.6). The mobility of holes in epitaxial BaCuTeF thin films (4 - 8 cm^2/Vs) is also considerably larger than in polycrystalline samples (0.2 cm^2/Vs).[13] In-plane alignment of

BaCuChF thin films with the MgO substrate seems of lesser importance because the hole mobility in the fully-aligned BaCuSeF thin films reported in this work is similar to that of films with significant 45^o in-plane misalignment and some weak (102) and (204) XRD peaks.[33] Different degrees of influence of in-plane alignment and out-of-plane *c*-axis orientation can be partially explained by the anisotropic structure of BaCuChF. The valence bands of these materials are broader in the Γ-*X* and Γ-*M* directions in *k*-space, compared to the Γ-*Z* direction.[31] These directions correspond respectively to the in-plane (*a* and *b* crystallographic axes) and out-of-plane (*c* crystallographic axis) directions of the anisotropic BaCuChF crystal structure (Fig. 2.1a). Covalent Cu-Ch sheets along the *a* and *b* axes give larger band dispersion, smaller in-plane effective mass ($|m_x| = 4.23\ m_e$ for BaCuSeF) and good lateral mobility in *c*-axis oriented BaCuChF thin films, regardless of the in-plane alignment. Alternating these layers with ionic Ba-F sheets along the *c*-axis results in a large out-of-plane effective mass ($|m_z| = 34.7\ m_e$ for BaCuSeF). Thus, the weighted average of in-plane and out-of-plane effective masses ($|m_{av.}| = |m_z|+2|m_x|)/3 = 14.4m_e$), which is the relevant effective mass when considering mobility in randomly oriented films,[34] is about factor of 3 - 4 larger than the in-plane effective mass. The effective mass difference only partially explains the order-of-magnitude lower hole mobility in randomly oriented polycrystalline BaCuChF thin films as compared to the *c*-axis oriented films. The other major cause of lower mobility in polycrystalline samples must be the presence of grain boundaries that are likely to be terminated with oxygen. Oxidized grain boundaries may create additional potential barriers for the transport of holes through polycrystalline thin films thereby causing their lower mobility and conductivity. Details of the photoelectron spectroscopy experiments that confirm oxidation of BaCuChF surfaces upon exposure to the atmosphere are discussed in a separate publication.[29]

There is a systematic evolution of the electrical transport properties of $BaCu(Ch_{1-x}Ch'_x)F$ thin films with *x*. The conductivity of the thin films increases by more than three orders of magnitude with increasing heavy chalcogen content (Fig. 2.6b). This change is quite large for materials that have not been intentionally doped. Table 2.1 shows that both the carrier concentration (p) and the carrier mobility (μ) contribute to the

conductivity (σ) trend. The telluride exhibits a carrier concentration of 10^{20} cm^{-3}, about an order of magnitude higher than the selenide, while the mobility is about a factor of four larger. The concentration and mobility of the holes in the BaCuSF thin films could not be reliably determined from Hall effect measurements. In part, the increase of mobility with increasing weight of the chalcogen in BaCuChF results from larger valence band dispersion near the maximum.[31] This effect is attributed to the higher energy of Ch *p*-levels and their better overlap with Cu *d*-orbitals[35] and results in the 10% difference of in-plane effective mass between the selenide and the telluride and 30% difference between the sulfide and the selenide,[31] which is rather moderate contribution to the mobility change. Another possible contribution to the mobility change is scattering of carriers from native defects caused by loss of chalcogen. The concentration of such defects is likely to be larger in the selenide and the sulfide than in the telluride, because the volatility of elemental Se and S is higher than that of Te. Finally, oxidized grain boundaries present in not-fully-epitaxial BaCuSF samples also may contribute to low mobility of the holes in thin film samples of this material.

Table 2.1 Concentration and mobility of holes and resulting conductivity of *c*-axis oriented BaCuChF thin films on MgO substrates. The Hall effect in BaCuSF samples could not be reliably measured.

Property	BaCuSF	BaCuSeF	BaCuTeF
μ (cm^2/Vs)	-	1.7	8.0
p (cm^{-3})	-	10^{19}	10^{20}
σ (S/cm)	0.02	0.32	128

The physical origin of change in the carrier concentration is an even more complicated question. The presence of free holes in nominally undoped BaCuChF must be caused by native defects and thus the change in carrier concentration in the S, Se, Te series must originate from the difference in the chemistry of the native defects. Four possible scenarios are (i) a decrease in formation enthalpy of the carrier-producing acceptor with increasing heavy chalcogen, (ii) different kind of acceptor for three

BaCuChF compounds, (iii) a different kind of compensating donor-like defect, and (iv) different degree of the compensation. It is not yet clear which effect is dominant, and a precise answer to this question requires careful experimental and theoretical investigation.

2.4 Summary

We report the structural, optical and transport properties of $BaCu(S_{1-x}Se_x)F$ and $BaCu(Se_{1-x}Te_x)F$ thin film solid solutions deposited on single crystal MgO (100) substrates. The films are produced by pulsed laser deposition of alternating layers of BaCuChF (Ch=S, Se or Se, Te) from single-phase targets onto heated substrates. The resulting *c*-axis oriented $BaCu(Ch_{1-x}Ch'_x)F$ thin films show no indication of original layering. The films are fully transparent with a systematic decrease in the transparency window through the BaCuSF-BaCuSeF-BaCuTeF. All the films show *p*-type conductivity, but it changes by more than three orders of magnitude through the series. Alloying of different BaCuChF materials in thin film form allows tuning of the unit-cell parameter and the absorption edge. The unit cell parameters of BaCuChF powder solid solutions obtained from XRD agree well with the results of first-principles calculations for BaCuChF materials, and those of $BaCu(Ch_{1-x}Ch'_x)F$ interpolate between them.

References

[1] J. A. Spies, R. Schafer, J. F. Wager, P. Hersh, H. A. S. Platt, D. A. Keszler, G. Schneider, R. Kykyneshi, J. Tate, X. Liu, A. D. Compaan, W. N. Shafarman, Sol. Energy Mater. Sol. Cells **93,** 1296(2009).

[2] W. Jaegermann, A. Klein, T. Mayer, Adv. Mater. **21**, 4196 (2009).

[3] S. Tokito, K. Noda, Y. Taga, J. Phys. D: Appl. Phys. **29,** 2750(1996).

[4] H. Yanagi, M. Kikuchi, K.-B. Kim, H. Hiramatsu, T. Kamiya, M. Hirano, H. Hosono Org. Electron. **9,** 890(2008).

[5] U. Ozgur, Ya. I. Alivov, C. Liu, A. Teke, M. A. Reshchikov, S. Dogan, V. Avrutin, S.-J. Cho, and H. Morkoc, J. Appl. Phys. **98,** 041301(2005).

[6] M. D. Irwin, D. B. Buchholz, A.W. Hains, R. P. H. Chang, T. J. Marks, Proc. Natl. Acad. Sci. U.S A. **105,** 2783(2008).

[7] H. Kawazoe, M. Yasukawa, H. Hyodo, M. Kurita, H. Yanagi, H. Hosono, Nature **389,** 939(1997).

[8] For a review see A. N. Banerjee, K. K. Chattopadhyay, Prog. Cryst. Growth Charact. Mater. **50,** 52(2005).

[9] K. Ueda, S. Inoue, S. Hirose, H. Kawazoe, H. Hosono, Appl. Phys. Lett. **77,** 270 (2000).

[10] S. Park, D. A. Keszler, M. M. Valencia, R. L. Hoffman, J. P. Bender, J. F. Wager, Appl. Phys. Lett. **80,** 4393(2002).

[11] J. Tate, P. F. Newhouse, R. Kykyneshi, P. A. Hersh, J. Kinney, D. H. McIntyre, D. A. Keszler, Thin Solid Films **516,** 5795(2008).

[12] K. Ueda, H. Hiramatsu, M. Hirano, T. Kamiya, H. Hosono, Thin Solid Films **496,** 8(2006).

[13] R. Kykyneshi, D. H. McIntyre, J. Tate, C.-H. Park, D. A. Keszler, Solid State Sci. **10,** 921(2008).

[14] J. Narayan, A. K. Sharma, A. Kvit, C. Jin, J. F. Muth, O. W. Holland, Solid State Commun. **121,** 9(2001).

[15] Y. Kamihara, T. Watanabe, M. Hirano, H. Hosono, J. Am. Chem. Soc.**130,** 3297(2008).

[16] H. Yanagi, S. Park, A. D. Draeseke, D. A. Keszler, J. Tate, J. Solid State Chem. **175,** 34(2003).

[17] H. Hiramatsu, K. Ueda, H. Ohta, M. Hirano, M. Kikuchi, H. Yanagi, T. Kamiya, H. Hosono, Appl. Phys. Lett. **91,** 012104(2007).

[18] H. Hiramatsu, K. Ueda, H. Ohta, M. Hirano, T. Kamiya, H. Hosono, Appl. Phys. Lett. **82,** 1048(2003).

[19] B. D. Cullity, S. R. Stock, Elements of X-Ray Diffraction (3rd Edition), Prentice Hall, Englewood Cliffs, NJ, 2001.

[20] G. Kresse, J. Furthmüller, Phys. Rev. B **54**, 11169(1996).

[21] F. D. Murnaghan, Proc. Natl. Acad. Sci. U.S.A. **30,** 244(1944).

[22] D. B. Chrisey, G. K. Graham, Pulsed Laser Deposition of Thin Films, John Wiley and Sons, New York, NY, 1994

[23] C. H. Park, D. A. Keszler, H. Yanagi, J. Tate, Thin Solid Films **445,** 288(2003).

[24] C. H. Park, R. Kykyneshi, A. Yokochi, J. Tate, D. A. Keszler, J. Solid State Chem. **180,** 1672 (2007).

[25] C. Goyhenex, H. Bulou, J. P. Deville, G. Tréglia, Appl. Surf. Sci. **177,** 238(2001).

[26] L. B. Freund and Subra Suresh, Thin Film Materials, Cambridge University Press, Cambridge, UK, 2003.

[27] B. J. Gibbons, Y. Fan, A. T. Findikoglu, Q. X., Jia, D. W.Reagor, J. Vac. Sci. Technol., A **19,** 56(2001)

[28] L. A. Knauss, J. M. Pond, J. S. Horwitz, D. B. Chrisey, C. H. Mueller, R. Treece, Appl. Phys. Lett. **69,** 25(1996).

[29] A. Zakutayev, J. Tate, H. A. S. Platt, D. A. Keszler, C. Hein, T. Mayer, A. Klein, W. Jaegermann, J. Appl. Phys. (to be published)

[30] A. Zakutayev, J. Tate, H. A. S. Platt, D. A. Keszler, A. Barati, A. Klein, W. Jaegermann, Appl. Phys. Lett. (to be published)

[31] A. Zakutayev, R. Kykyneshi, G. Schneider, D. H. McIntyre, J. Tate, Phys. Rev. B (to be published)

[32] N. Peyghambarian, S. W. Koch, A. Mysyrowicz, Introduction to Semiconductor Optics, Prentice Hall, Englewood Cliffs, NJ, 1993.

[33] R. Kykyneshi, Ph.D. Thesis, Department of Physics, Oregon State University, USA, 2007.

[34] J. E. Medvedeva: Europhys. Lett. **78,** 57004(2007).

[35] H. Yanagi, J. Tate, S. Park, C. -H. Park, D. A. Keszler, M. Hirano, H. Hosono, J. Appl. Phys. **100,** 083705(2006).

CHAPTER 3

Electronic structure and excitonic absorption in BaCuChF (Ch = S, Se, Te)

A. Zakutayev, R. Kykyneshi, G. Schneider, D. H. McIntyre and J. Tate

Phys. Rev. B **81**, 155103 (2010)

3.1 Introduction

Quaternary mixed-anion compounds with the ZrCuSiAs-type layered crystal structure (P4/*nmm* space group), such as oxychalcogenides,[1] fluorochalcogenides,[2] and oxypnictides[3] have recently received considerable attention. The large number of possible combinations of components and dopants results in interesting physical properties such as simultaneous transparency and degenerate *p*-type conductivity,[4] ferromagnetic response,[5] and high temperature superconductivity.[6] These materials have potential applications in different technological fields such as transparent electronics,[7] thermoelectrics,[8] optoelectronics[9] and photovoltaics.[10]

In this paper, we present a detailed experimental and theoretical study of the electronic and optical properties of one family in this group, Ba-based chalcogenide-fluorides BaCuChF (Ch = S, Se, Te) and their solid solutions, which show *p*-type conductivity, wide direct optical band gaps, and room temperature excitons. The structural anisotropy of BaCuChF gives rise to anisotropic effective masses of electrons and holes, and to large exciton reduced masses (0.90 m_e and 0.80 m_e in BaCuSF and BaCuSeF respectively, compared to 0.058m_e in GaAs), which lead to large exciton binding energies (95 meV and 65 meV, compared to 4.2 meV in GaAs).[11] Spin-orbit coupling in the Ch atom results in degeneracy removal at the Γ-point of the BaCuChF valence band, which in turn causes splitting of the excitonic absorption peaks. The peak splitting can be tuned by changing the chalcogen content of BaCuChF-based thin-film solid solutions. BaCuTeF thin films exhibit no excitonic absorption because the electron-hole interaction is screened by a high concentration of free holes that also cause a moderate valence band filling effect. The transparency range of thin-film BaCuTeF is comparable to that of BaCuSeF, the major reason being suppressed inter-band transitions.

The BaCuChF materials are similar to their isostructural counterparts, the La-based layered oxychalcogenides where the $[Ba_2^{2+}F_2^{1-}]^{2+}$ sheets are replaced by $[La_2^{3+}O_2^{2-}]^{2+}$ layers[12]. LaCuOCh and their solid state solutions also have spin-orbit split excitonic peaks followed at higher energies by stepwise absorption spectra with lower-intensity peaks.[13] The separation between the excitonic absorption peaks increases with increasing atomic weight of Ch (S or Se) or Ln (La, Pr or Nd) in the solid solutions, which is

attributed to spin-orbit coupling effects.[14] The exciton binding energy in LaCuOS and LaCuOSe (50 meV)[15] is smaller than in BaCuSF and BaCuSeF. While LaCuOTe develops an indirect band gap,[16] BaCuTeF retains a direct band gap at the Γ-point.

The paper is laid out as follows. The experimental and computational details are followed by a description of the BaCuChF electronic structure and optical properties. The discussion is divided into three sub-sections. First, we consider BaCuSF and BaCuSeF, analyzing the exciton absorption in terms of a three-dimensional Wannier-Mott model. Second, we consider BaCuTeF, its higher-than-expected transparency, and the absence of excitonic absorption. Finally, we discuss the absorption spectra of the $BaCu(Ch_{1-x}Ch'_x)F$ thin-films solid solutions.

3.2. Experimental and computational methods

Thin films of BaCuChF (Ch = S, Se, Te) were deposited by pulsed laser deposition (PLD) from dense, single-phase ceramic targets, and $BaCu(Ch_{1-x}Ch'_x)F$ thin-film solid solutions were prepared by alternating PLD from these targets. All the films were phase-pure, of excellent quality and highly *c*-axis oriented. BaCuSeF and BaCuTeF films also exhibited strong in-plane order. The concentration of free holes in these samples was determined using Hall effect measurements to be 10^{19} and 10^{20} cm^{-3} respectively, in close agreement with the results in Ref. 17 and Ref. 18. For BaCuSF, the carrier concentration could not be reliably measured using this method, but it was estimated to be 10^{18} cm^{-3} based on the measurement of the resistivity and on the calculation of the effective mass of the holes. More details of the preparation and characterization are described elsewhere.[18] The experimental thin film absorption spectra were determined from the transmittance and reflectance spectra, measured between 300 K and 80 K, using an analysis that removes the thin-film interference fringes that appear in the raw data in the region of the spectrum where the films are transparent.[19]

Most of the density functional theory (DFT) calculations were carried out with the Wien[20] and Flair[21] codes that use the full-potential linearized augmented plane-wave formalism within the Perdew-Burke-Ernzerhof generalized gradient approximation (GGA) of DFT. The muffin-tin radii were set to 2.5 a.u. for Ba and Cu in all BaCuChF,

2.2 a.u. and 2.3 a.u. for S and F in BaCuSF, 2.3 a.u. and 2.4 a.u. for Se and F in BaCuSeF, and 2.5 a.u. and 2.5 a.u. for Te and F in BaCuTeF, respectively. The potentials and charge densities were expanded on a *k*-mesh of 6875 points in the Brillouin zone, including 546 unique *k*-points. Inside the muffin-tin spheres, the potentials and charge densities were expanded up to $l = 10$, while in the interstitial regions, they were expanded using 3523 plane waves. The calculations were iterated until the total energies converged to better than 0.1 mRy and the total charge converged to better than $10^{-3}e$. GGA DFT results were used as input for the electronic band structure calculation that included many-body- and self-energy effects in the GW approximation[22] and is referred to as the "GW calculation" in the text. The GW calculation was performed with the VASP[23] code using the projector-augmented-wave method was used with a 6 x 6 x 3 *k*-point mesh, and a 275 eV planewave cut-off energy. The GW calculation gives a realistic band gap estimate, but it is computationally expensive, so we used GGA DFT as described above for the spin-orbit effects, absorption spectra, and effective mass calculations.

TABLE 3.1. Effective masses in BaCuChF calculated by GGA DFT. m_{av} is weighted average (2:1) of m_x and m_z. The band designations are those in Fig. 3.1.

Eff. mass	BaCuSF		BaCuSeF		BaCuTeF	
(m_e)	CB_I	VB_A	CB_I	VB_A	CB_I	VB_A
m_x	0.68	5.41	0.54	4.23	0.51	3.85
m_z	0.92	37.5	0.82	34.7	2.94	27.0
m_{av}	0.76	16.1	0.63	14.4	1.32	11.6
m_z/m_x	1.35	6.92	1.53	8.21	5.81	7.01

3.3 Results

3.3.1 Electronic structure

The GGA DFT results reported here extend our previously-reported calculations,[24] which indicated that the valence bands (VB) of BaCuChF are degenerate at the Γ point. Spin-orbit interaction effects included in the present calculation remove this degeneracy [Fig. 3.1(a)]. The separation between spin-orbit split bands *A* and *B* (VB_A and VB_B) Δ_{SO} increases from BaCuSF (22 meV) through BaCuSeF (89 meV) to

BaCuTeF (250 meV). The VBM of BaCuChF is highly anisotropic as a consequence of the layered crystal structure. The valence bands are narrow in the *ΓZ* direction, which corresponds to the crystallographic *c*-axis in the tetragonal crystal structure, but broad in the *ΓX* direction, which lies in the *ab* plane of the crystal.

All three members of BaCuChF family have similar band character near the valence band maximum (VBM) [Fig. 3.1(b)]. The VBM is composed of Cu 3*d* orbitals well mixed with Ch *np* orbitals (*n* = 3 for S, *n* = 4 for Se and *n* = 5 for Te). As the mass of the Ch atom increases, the ratio of Ch *np* to Cu 3*d* character at the VBM also increases. This can be explained by the upward shift of the Ch *np* level. The bands derived from fluorine (F) atomic orbitals lie deeper and have almost no contribution to either the VBM or the conduction band minimum (CBM).

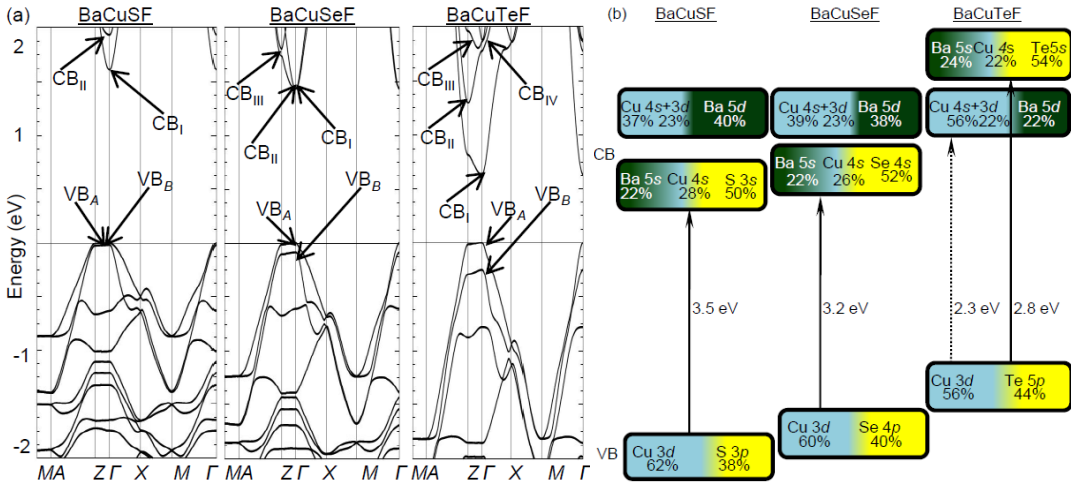

FIG. 3.1. (a) Relativistic band structure of BaCuChF calculated by GGA DFT. The spin-orbit split valence bands are labeled VB_A and VB_B, while the conduction bands are labeled CB_I, CB_{II}, CB_{III}, and CB_{IV}. (b) Schematic electronic structure of BaCuChF compounds. The band gaps in (b) are calculated using the GW approximation.

In contrast to the VB, the conduction band (CB) character of BaCuTeF is significantly different from that of BaCuSF and BaCuSeF, as shown in Fig. 3.1. In BaCuSF (BaCuSeF), two lowest conduction bands (CB_I and CB_{II}) are composed of Cu 4*s* and Ba 5*s* atomic orbitals well hybridized with S 3*s* (Se 4*s*) states, but in BaCuTeF, the corresponding band appears as the fourth conduction band (CB_{IV}). The third conduction

band (CB_{III}) in BaCuSF and BaCuSeF is derived from Cu 4*s* and Cu 3*d* atomic orbitals mixed with Ba 5*d* levels and is similar in character to the lowest conduction band (CB_I) in BaCuTeF. CB_{II} and CB_{III} in BaCuTeF are also derived mostly from Cu and Ba states.

TABLE 3.2. Theoretical electronic and optical band gaps in BaCuChF. The GW optical band gap for BaCuTeF is the difference between the VB and CB_{IV}

Band gap	BaCuSF		BaCuSeF		BaCuTeF	
(eV)	Elec.	Opt.	Elec.	Opt.	Elec.	Opt.
GGA DFT	1.63	1.63	1.49	1.49	1.02	1.49
GW	3.72	3.72	3.27	3.27	2.11	3.05

The GGA DFT directional effective masses of the holes and electrons, their ratios and averages are summarized in Table 3.1. The in-plane effective mass of the holes m_x^{VB} is significantly smaller than their out-of-plane effective mass m_z^{VB}, so the anisotropy m_z^{VB}/m_x^{VB} is large. The hole effective masses decrease with increasing atomic mass of the chalcogen in BaCuChF. The effective masses of the electrons in BaCuSF and BaCuSeF are more isotropic, as expected from the *s*-character of CB_I. This is not the case for BaCuTeF due to the contribution from directional *d*-states to CB_I. The average effective masses of the electrons and holes (m^{CB}_{av} and m^{VB}_{av}) were obtained from a weighted average (2:1) of the in-plane and out-of-plane effective masses (Table 3.1).

Band gaps of BaCuChF compounds calculated by GGA DFT and GW are summarized in Table 3.2. The "electronic" band gap refers to the energy difference between the VBM and CBM and the "optical" band gap refers to the energy where the calculated absorption coefficient begins to increase significantly. We note that: (i) GGA DFT underestimates the band gaps compared to GW calculations; (ii) according to both calculations, the electronic band gap decreases from BaCuSF to BaCuSeF to BaCuTeF, and (iii) both calculations agree that the electronic and optical band gap are the same in BaCuChF (Ch = S, Se), and that optical band gap is larger than electronic in BaCuTeF.

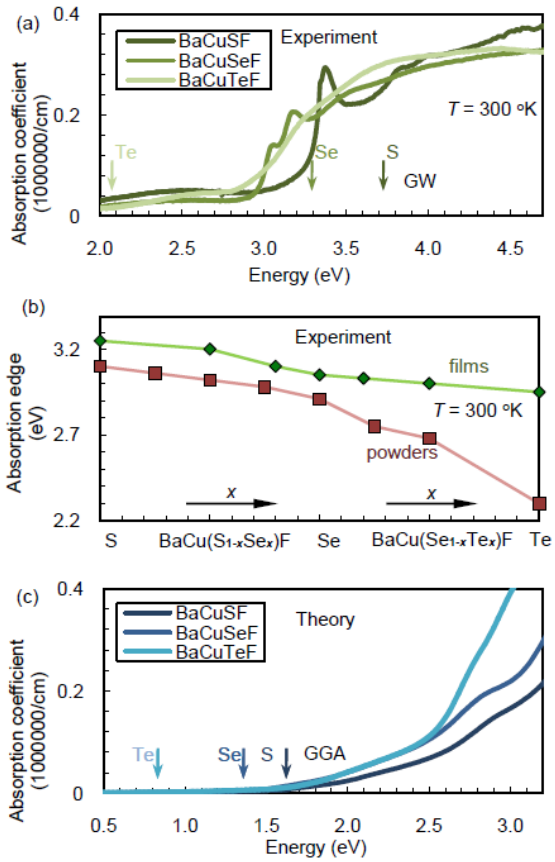

FIG. 3.2. (a) Room-temperature experimental absorption spectra of BaCuChF. (b) Experimental absorption edge of $BaCu(Ch_{1-x}Ch'_x)F$ thin films (diamonds) and powders (squares). The lines are guides to the eye. (c) Theoretical absorption spectra of BaCuSF, BaCuSeF and BaCuTeF. The arrows in (a) and (c) indicate the electronic bandgap as estimated by GW and GGA DFT calculations, respectively.

3.3.2. Optical properties

Figure 3.2(a) shows experimental room-temperature absorption spectra with the GW electronic gaps indicated by arrows. The main features of Fig. 3.2(a) are following. (i) There are narrow near-band-edge absorption peaks in the spectra of BaCuSF and BaCuSeF thin films, and these peaks are absent from the BaCuTeF absorption spectrum. (ii) The spectral position of the peaks is below the GW electronic band gap prediction for BaCuSF and BaCuSeF. (iii) The energy of the strong absorption edge in BaCuTeF thin films is similar to that in BaCuSeF and much higher than the BaCuTeF electronic gap calculated by GW. Table 3.3 and Fig. 3.2(b) summarize the positions of strong absorption edges from Fig. 3.2(a). Fig. 3.2(b) also includes similar information for

$BaCu(Ch_{1-x}Ch_x')F$ films and powders (the latter from diffuse reflection measurements). The absorption edge in BaCuChF films is at higher energies than in BaCuChF powders, and this difference is the most dramatic in BaCuTeF. Fig. 3.2(c) shows the theoretical GGA DFT optical absorption spectra, with the GGA DFT electronic gaps indicated by arrows. The BaCuSF and BaCuSeF absorption edges are close to the energy of the electronic gaps, while for BaCuTeF, the absorption edge is significantly higher.

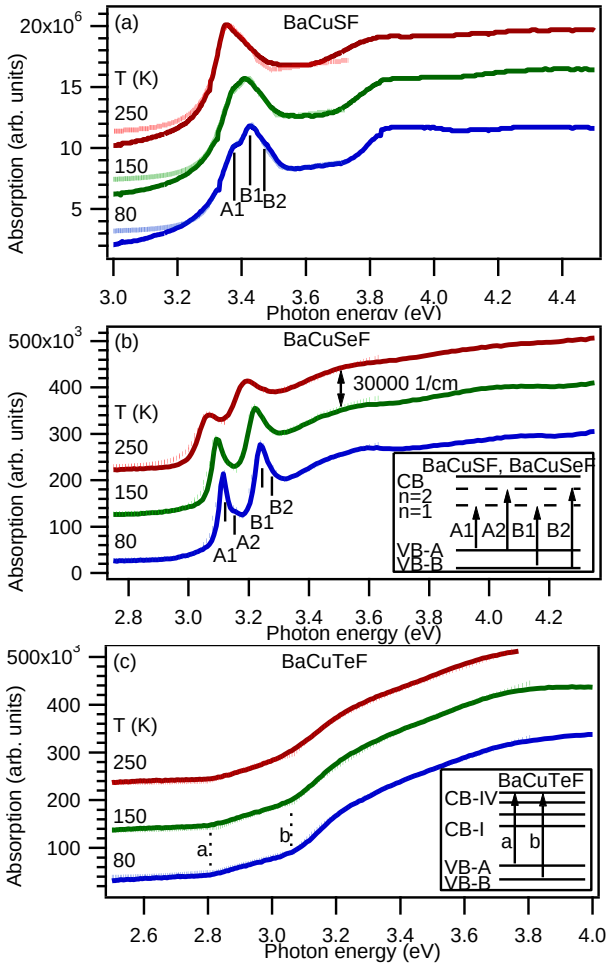

FIG. 3.3. Experimental absorption spectra of (a) BaCuSF, (b) BaCuSeF and (c) BaCuTeF at 80 K – 250 K. The dotted lines are fits based on the analysis described in the text. The spectra are offset on the vertical axis for clarity. Insets: schematic interpretation of the absorption spectra.

Figure 3.3 presents experimental optical absorption spectra of (a) BaCuSF, (b) BaCuSeF and (c) BaCuTeF thin films from 80 K to 250 K. At the lowest accessible temperature (80 K), two excitonic peaks are clearly distinct in BaCuSeF and are labeled A_1 and B_1. In addition, there is a weak shoulder on the high-energy side of each peak, and these shoulders are labeled A_2 and B_2, respectively. In the 80- K BaCuSF spectrum in Fig. 3.3(a), *A* and *B* are closer together and there is a step in the absorption spectrum close to 3.8 eV. The *A* and *B* absorptions broaden as the temperature increases, and persist to 400 K, the highest temperature attainable in the experimental setup. The BaCuTeF absorption spectra in Fig. 3.3(c) show no excitonic peaks even at 80 K, but instead there are two weakly temperature dependent absorption edges, labeled α and β. The separation of *A* and *B* and of α and β at 80 K are larger by about 30 meV, than the calculated spin-orbit splitting of the corresponding VBM. Figure 3.4 shows experimental absorption spectra of BaCu($S_{1-x}Se_x$)F and BaCu($Se_{1-x}Te_x$)F thin-film solid solutions. The excitonic absorption peaks of the mixed-chalcogen films are broader than those of the single-chalcogen samples. In general, as *x* increases, there is a gradual shift of the excitonic peaks to lower energy, an increase in peak separation, and a decrease of intensity when Te is added to the thin-film solid solution.

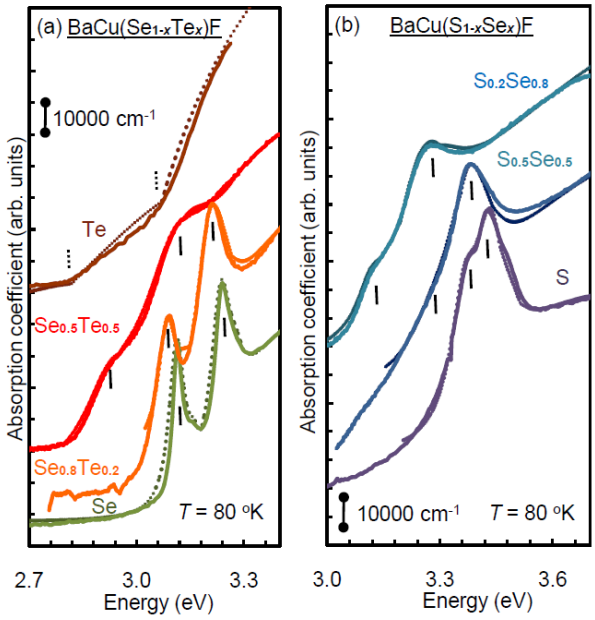

FIG. 3.4. Experimental absorption spectra of (a) BaCu($Se_{1-x}Te_x$)F and (b) BaCu($S_{1-x}Se_x$)F at 80 K. The dotted lines are fits to the data as discussed in the text. The spectra are offset on the vertical axis for clarity.

3.4 Discussion

3.4.1. BaCuSF and BaCuSeF

We attribute the *A* and *B* peaks in the experimental absorption spectra [Fig. 3.2(a)] of BaCuSF and BaCuSeF thin films to excitonic absorption. The peaks are absent from the theoretical spectra [Fig. 3.2(c)] because the GGA DFT does not include the electron-hole interaction. Furthermore, the peaks narrow as the temperature is lowered [Fig. 3.3(a) and 3.3(b)]. Since the *A*-*B* separation closely matches the calculated spin-orbit splitting, we assign the *A* and *B* absorption peaks to two different excitons, respectively associated with two spin-orbit split valence bands VB_A and VB_B [Fig. 3.1(a)]. According to this assignment, the A_1 and B_1 excitonic absorption peaks correspond to creation of the excitons in the ground state (n = 1), while the high-energy side shoulders A_2 and B_2 observed at low temperatures in BaCuSeF correspond to creation of excitons in the first excited state (n = 2), where n is a principal quantum number of the hydrogen-like excitonic energy levels.[25] In BaCuSF, absorption shoulder B_2 is also observed, but A_2 almost coincides with B_1 and cannot be resolved. The inset to Fig. 3.3(b) illustrates the assignment, with the dashed lines meant to represent the many-body exciton in a single-particle picture. We discard the alternative explanation that *A* and *B* represent the ground and excited states of a single exciton because the *A* and *B* peaks have similar intensity. High intensity spin-orbit split excitonic peaks are observed in materials other than BaCuChF, such as BaCh (Ch = S, Se, Te),[26] MCh_2 (M = W, Mo),[27] and LnCuOCh (Ln = La, Pr, Nd).[28]

TABLE 3.3. Experimental optical band gaps and absorption edges in BaCuChF. Experimental optical band gaps are extracted from fits of Eq. 2.1 to the data in Fig. 3.3 using Varshni relationship (Eq. 2.4). Experimental absorption edges are those shown in Fig. 3.2(a).

Band gap (eV)		BaCuSF	BaCuSeF	BaCuTeF
Abs. edge	Films	3.3	3.1	3.0
	Powders	3.2	3.0	2.3
Optical	VB_A	3.47	3.19	2.82
	VB_B	3.52	3.31	3.07

The experimental absorption spectra of BaCuSF and BaCuSeF [Fig. 3.3(a) and 3(b)] are consistent with a 3*D* Wannier-Mott model, because the intensities of A_2 and B_2 are about 8 times smaller than the intensities of A_1 and B_1, respectively. According to the 3*D* Wannier-Mott model, the absorption spectrum of a semiconductor with parabolic bands in the presence of electron-hole interaction has the form:[11]

$$\alpha(E) = \sum_i c_i \cdot E \cdot E_{xi} \cdot \left[\frac{\pi \cdot \exp(z_i)}{\sinh(z_i)} + \sum_{n=1}^{\infty} \frac{4}{n^3} \delta(E - E_{gi} + \frac{E_{xi}}{n^2}) \right] \qquad (2.1)$$

where c_i is a scaling factor and z_i is an energy variable parameterized by E_{xi} and E_{gi}:

$$z_i = \pi \cdot \sqrt{\frac{E_{xi}}{E - E_{gi}}} \qquad (2.2)$$

The first term in square brackets in Eq. 2.1 represents band-to-band transitions in the presence of the Coulomb interaction and causes α(*E*) to increase more rapidly near the band edge than if there were only free carrier absorption. To better fit the data in Fig. 3.3 and Fig. 3.4, the first term in Eq. 2.1 was multiplied by a broadening function B_{ci} (E, E_{gi}, Γ_{ci}) similar to that found in literature.[29] The second term in square brackets in Eq. 2.1 is a sum of delta-functions that represent transitions to discrete hydrogen-like excitonic energy levels. Each delta-function was approximated in the fits by a Lorentzian L_{xi} (E, Γ_{xi}, E_{xi}, E_{gi}, n, w_{i}), where Γ_{xi} is full width at half maximum (FWHM), and w_i is a weighting factor that accounts for the effects of structural disorder and other possible smearing factors on the intensity of the excitonic absorption. Despite the large number of parameters in the model, they are all physically reasonable.

Experimental absorption spectra of BaCuChF and BaCu($Ch_{1-x}Ch'_x$)F are in a good agreement with the 3*D* Wannier-Mott model as evidenced in Fig. 3.3 and Fig. 3.4. A 2*D* Wannier- Mott model cannot be fit to experimental data, since the ratio of n=1 and n=2 excitonic peaks in Fig. 3.3 is clearly not 27.[11, 30] The absorption spectrum in Fig. 3.3 is consistent with the superposition of two sets of absorption – one from VB_A to CB_{I} with the associated exciton (*A*-series) and one from VB_B to CB_{I} with its associated exciton (*B*-

series). Thus the *B*-series is superimposed on the continuum absorption from VB_A to CB_I. This structure appears similar to step-functions observed in LaCuOCh thin films.[28] The higher-energy absorption peaks observed in LaCuOCh samples prepared by RSPE[28] are not observed in the *in-situ* processed BaCuSF films reported in this work (Fig. 3.3a). The absence of higher energy peaks in BaCuChF samples may have to do with a different dimensionality of the excitons, or with better crystallinity of the LaCuOCh films, which are processed at a much higher temperature. We do observe a weak feature in BaCuSF spectrum at 3.8 eV (Fig. 3.3a), which could be a smeared transition from two valence bands to a higher-lying conduction band CB_{II} (Fig. 3.1a). There is no corresponding feature in BaCuSeF absorption spectrum (Fig. 3.3b) because in this material CB_{II} is almost degenerate with CB_I (Fig. 3.1a).

Experimental and theoretical parameters of the excitons extracted from the 3*D* Wannier- Mott model are summarized in Table 3.4. Experimental exciton binding energies E_{xi} were determined from the fit of Eq. 2.1 to the 80-K absorption spectra in Fig. 3.3. Next, the corresponding average excitonic radii a_{xi} and reduced effective masses μ_{xi} shown in Table 3.4 were calculated using

$$E_{xi} = \frac{E_H a_H}{\varepsilon} \cdot \frac{1}{a_{xi}} = \frac{E_H}{\mu_H \varepsilon^2} \cdot \mu_{xi} \qquad (2.3)$$

where E_H , a_H and μ_H are, respectively, the ionization potential, Bohr radius and reduced mass of the hydrogen atom, and ε is the static relative dielectric constant. Eq. 2.3 was also used to calculate the theoretical binding energies and effective radii of excitons from their theoretical reduced effective masses μ_{xi}, found from the GGA DFT average effective masses of the carriers (Table 3.1). These calculations lead to the conclusion that the high binding energies of the excitons in BaCuChF (Ch = S, Se) result from high out-of-plane effective mass of the holes. The corresponding average effective radius of the excitons is comparable to 1 *c*-axis- or 2 *a*-axis lattice constants in BaCuChF, close to the limit where macroscopic parameters such as ε are meaningful. The dielectric constant of BaCuChF was approximated by a simple average of those for barium fluoride (ε = 7.4), barium sulfate (ε = 11.4) and cupric sulfate (ε = 10.3).[31] Despite this rough approximation, the theoretical and experimental binding energies of the excitons are in

fair agreement with each other (Table 3.4). We note that the macroscopic exciton model is also valid for excitons in Cu_2O, despite their small effective radii.[11]

TABLE 3.4. Parameters of the *A*-excitons in BaCuChF. The exciton binding energy E_x is extracted from the fit of Eq. 2.1 to the experimental data in Fig. 3.3. The exciton reduced mass μ_x is calculated from the theoretical data in Table 3.1. The exciton radius a_x and the screening length r_0^{TF} are calculated using Eq. 2.3 and Eq. 2.7, respectively.

	BaCuSF		BaCuSeF.		BaCuTeF	
	Expt.	Theor.	Expt.	Theor.	Expt.	Theor.
E_x (meV)	95	105	65	87	-	171
a_x (nm)	0.87	0.70	1.1	0.85	-	0.43
μ_x (m_e)	0.49	0.90	0.45	0.80	-	1.18
r_0^{TF} (nm)		>1.1		1.1		0.20

The FWHM of the excitonic peaks Γ_{xi} and the optical band gaps E_{gi} were extracted from the fits of Eq. 2.1 to the experimental absorption spectra measured at different temperatures (Fig. 3.3). In these fits, we constrained the exciton binding to that at 80 K, and found Γ_{xi} and E_{gi} at every experimental temperature. The temperature dependence of Γ_{xi} and E_{gi} is shown in Fig. 3.5. BaCuChF optical band gaps decrease with increasing temperature. The temperature dependence of the experimental optical gaps E_{gA} and E_{gB} [Fig. 3.5(a) and 3.5(b)] was fit using Varshni relationship: [32]

$$E_{gi}(T) = E_{gi}(0) - \alpha_i T^2/(T+\beta_i) \qquad (2.4)$$

where α_A = 0.19 meV/K and α_B = 0.22 meV/K for BaCuSF, α_A = 0.36 meV/K and α_B = 0.40 meV/K for BaCuSeF, and β_i = 100 K for both materials. From these fits we find that zero-temperature experimental optical band gaps of BaCuSF and BaCuSeF $E_{gi}(0)$ (Table 3.3) are in good agreement with theoretical GW predictions (Table 3.2). In Table 3.3, BaCuChF experimental optical band gaps are also compared to the spectral positions of the optical absorption edges of the BaCuChF thin films and powders from Fig. 3.2b. The experimental optical gaps are higher than the absorption edges reported here (Fig. 3.2b) and in our previous work,[17] because of the presence of sub-gap excitonic absorption peaks in BaCuSF and BaCuSeF thin films. In BaCuSF and BaCuSeF powders, and $BaCu(S_{1-x}Se_x)F$ powder solid solutions studied by our group,[33] the

absorption edge determined from the diffuse reflectance measurements by Kubelka-Munk method[34] is 0.1 eV lower than absorption edge of thin films with the same composition, (Fig. 3.2b) possibly due to the disorder and band tail effects of materials prevalent in microcrystalline form.

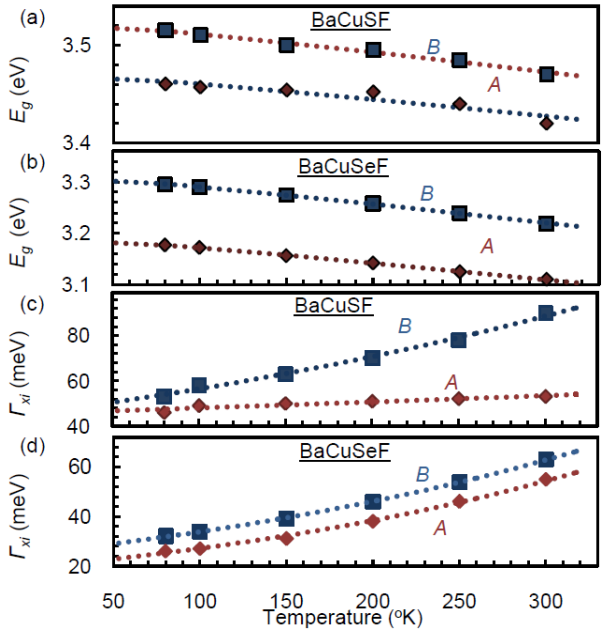

FIG. 3.5. (a and b) Band gaps and (c and d) FWHM of the excitonic peaks in BaCuSF and BaCuSeF absorption spectra for spin-orbit split valence bands *A* and *B*. The dotted lines are fits to the data as discussed in the text.

The excitonic absorption peaks broaden with increasing temperature. The temperature dependence of the FWHM of the excitonic peaks Γ_{xi} [Fig. 3.5(c) and 3.5(d)] was fit with an exponential function, since it gave a better fit than a polynomial:

$$\Gamma_{xi}(T) = \Gamma_{xi}(0) \cdot \exp(d_i \cdot T) \qquad (2.5)$$

where d_A = 3.5 mK^{-1} and d_B = 3.1 mK^{-1} for BaCuSeF, and d_A = 0.54 mK^{-1} and d_B = 2.3 mK^{-1} for BaCuSF. The thermal broadening rate of the excitonic peaks in BaCuSF is smaller than in BaCuSeF, because the exciton binding energy in BaCuSF is larger. The FWHM of the peaks in BaCuSF is larger, because the density of native defects in BaCuSF is larger (S is more volatile than Se and can be more easily lost in the pulsed laser deposition process).

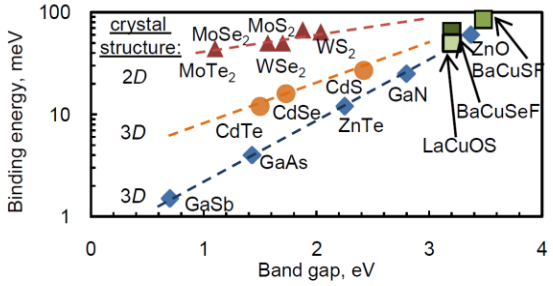

FIG. 3.6. Exciton binding energy as a function of band gap for materials with different crystal structures. Dashed lines are guides for the eye.

Finally, we compare the excitons in BaCuSF, BaCuSeF and other semiconductors. Fig. 3.6 shows an empirical plot of exciton binding energy *vs.* band gap energy for various materials. As examples of 3*D*-like materials, we present metal pnictides, oxides and chalcogenides, and as examples of 2*D*-like compounds we show transition-metal dichalcogenides and mixed-anion quaternary compounds. From Fig. 3.6 we note that: (i) 3*D* chalcogenides have larger exciton binding energies than 3*D* pnictides and oxides; (ii) 2*D*-like materials have larger excitonic binding energy than 3*D*-like compounds; (iii) the mixed-anion BaCuChF and LaCuOCh fall on the intersection of the 2*D* and 3*D* lines. The effective radius of the excitons in BaCuChF is comparable to the *c*-axis lattice parameter and to twice the *a*-axis lattice parameter (Table 3.4), which makes it difficult to use this size argument to determine the dimensionality of the excitons. At most it might be said that they are close to both 2*D* and 3*D* limits, which is consistent with the position of the BaCuChF points in Fig. 3.6. In addition we note that 2*D*-like WSe_2 has excitons that are well described by a 3*D* Wannier-Mott model,[30] so there is not necessarily a direct correlation between the dimensionality of the crystal structure and dimensionality of the excitons. As discussed in Ref.30, both the kinetic and potential energy operators in the Hamiltonian must be two-dimensional for the excitons to be truly two-dimensional. On one hand, the kinetic energy operator is usually two-dimensional for layered compounds with anisotropic carrier effective masses. On the other hand, the dimensionality of the potential energy operator depends on the local crystallographic symmetry, which is not always 2*D*-like for layered compounds. Thus the question of the

exciton dimensionality in layered materials is quite complicated and requires careful material-specific investigation.

3.4.2. BaCuTeF

Two features of experimental absorption spectrum of BaCuTeF require explanation - the large optical band gap of the films (Fig. 3.2, Tables 3.2 and 3.3) and the absence of excitonic absorption even in the highest quality epitaxial samples at the lowest accessible temperatures [Fig. 3.3(c)].

First, we turn our attention to large optical band gap in the BaCuTeF thin films. According to both GGA DFT and GW, in BaCuTeF the electronic gap is smaller than the optical gap (Table 3.2), so the probability of the lowest energy optical transitions must be small, which can be qualitatively understood as follows. Referring to Fig. 3.1(b), the VBM is primarily derived from Cu 3*d*/Te 5*p* orbitals and the CBM has mainly Ba 5*d*/Cu 4*s*/Cu 3*d* character. Transitions of the type Cu 3*d* - Cu 4*s* or Cu 3*d* - Cu 3*d* are suppressed by an electric dipole selection rule ($\Delta l \pm 1$), and transitions of the type Te 5*p* - Cu 4*s*, Te 5*p* - Ba 5*d* and Cu 3*d* - Ba 5*d* are suppressed because the initial and final Bloch states have most of their weight on different atoms and the overlap of the corresponding wave functions is small (similar to the Franck-Condon argument in molecular physics). For similar reasons, transitions from the VBM to Ba-5*d*-derived CB_{II} and CB_{III} must be also suppressed. In powders, the amount of material is large enough that these weak transitions can be detected, so an absorption edge is at 2.3 eV according to powder diffuse reflectance measurements.[35] In BaCuTeF films, the optical gap is determined by the strong VB-CB_{IV} transition. As schematically shown in the inset of Fig. 3.3(c), we attribute the two absorption edges α and β to transitions from the spin-orbit split Te 5*p*-derived VB_A and VB_B to the Te 5*s*-derived CB_{IV}. Corresponding optical band gaps (Table 3.3) are in good agreement with the results of GW calculations (Table 3.2). Similar suppressed lowest energy optical transitions enhance the transparency in the *n*-type transparent conductor In_2O_3,[36] and a family of *p*-type transparent conductors $CuMO_2$ (M = Al, Ga, In).[37]

An additional contribution to the extended transparency range of both thin films and powders of BaCuTeF comes from the Moss-Burstein band filling. Band-filling can be clearly seen in *n*-type transparent conductors with highly disperse CBs, such as In_2O_3:Sn[38] and CdO:In.[39] Since for the wide-gap *p*-type BaCuTeF the CB filling is negligible, the shift of the absorption edge may be approximated by the change in the chemical potential in a Fermi-Dirac distribution $f_{FD}(E)$, that can be found using the relationship

$$p = \int_{-\infty}^{0} D_{VB}(E)\,[1 - f_{FD}(E)]\,dE \qquad (2.6)$$

where $D_{VB}(E)$ is the density of states per unit volume, calculated from first principles using GGA DFT and p is the concentration of holes. Experimentally measured $p = 10^{20}$ cm^{-3} in BaCuTeF sets the chemical potential 0.25 eV below the VBM, in reasonable agreement with the 0.19 eV discrepancy between the GW electronic gap (Table 3.2) and energy of the powder absorption edge (Table 3.3). If the concentration of holes in BaCuTeF were 10^{21} cm^{-3}, the Moss-Burstein shift (0.54 eV) would become comparable to the shift caused by suppressed transitions, but the concentration of holes in BaCuTeF is difficult to control, so it is hard to experimentally observe this change.

We turn now to the suppression of excitons in BaCuTeF. The theoretical exciton binding energy in BaCuTeF (Table 3.4) is much higher than the 7-meV thermal fluctuations that correspond to the lowest accessible temperature of our experimental setup (80 K), but the excitons are absent from the experimental absorption spectra [Fig. 3.3(c)]. We attribute the lack of excitons in BaCuTeF to screening of the electron-hole interaction by free holes. To explain the absence of the excitonic peaks in BaCuTeF (and their presence in BaCuSF and BaCuSeF), we consider the Thomas-Fermi approximation of the screened electrostatic potential:

$$\varphi(r) = \frac{e}{4\pi\varepsilon_0\varepsilon r}\exp\left(-\frac{r}{r_0^{TF}}\right) = \frac{e}{4\pi\varepsilon_0\varepsilon r}\exp\left(-r\cdot\sqrt{\frac{6\pi e^2 p}{\varepsilon\varepsilon_0 E_f}}\right) \qquad (2.7)$$

where e is a unit charge, r is the electron-hole separation, r_0^{TF} is a screening length and E_f is the energy of the charge carriers at the Fermi surface of metal.[40] In the case of a

degenerately doped *p*-type semiconductor, E_f can be approximated by the average energy of free holes in the valence band:

$$\langle E \rangle = \left[\int_{-\infty}^{0} E D_{VB}(E) f_{FD}(E) dE \right] / \left[\int_{-\infty}^{0} D_{VB}(E) f_{FD}(E) dE \right] \quad (2.8)$$

Fermi screening length for three BaCuChF compounds is summarized in Table 3.4. The concentration of free holes in BaCuTeF is $p = 10^{19}$-10^{20} cm^{-3} at all accessible temperatures, because the conductivity change between from 300 K to 80 K is quite small.[41] The resulting screening length of 0.20 nm is smaller than the effective radius of the excitons, so free holes effectively screen the electron-hole interaction and lead to suppression of excitonic absorption in BaCuTeF thin films. In addition, CB_I in BaCuTeF has no Te character [Fig. 3.1(b)], which precludes creation of the excitons associated with the Te atom. In contrast to BaCuTeF, BaCuSF and BaCuSeF have Ch character in both VB and CB_I, and the screening length in thin films of these materials is larger than the average radius of the excitons due to a lower concentration of free holes.[17]

Since BaCuChF materials were not intentionally doped, free holes must originate from ionized native defects. The local electric fields created by these defects are not sufficient to destroy the excitons in any of three BaCuChF materials. For this calculation, the magnitude of electric field experienced by an electron (or a hole) in the exciton was compared to the electric field at a distance approximately equal to the half of the average distance between the defects. This simple order-of-magnitude estimation was done assuming no defect compensation effects and using an algorithm similar to calculation of metal-insulator transitions in semiconductors.[42]

3.4.3. BaCu($Ch_{1-x}Ch'_x$)F Solid Solutions

The splitting of the peaks in the experimental absorption spectra of the BaCuSF, BaCuSeF and BaCu($S_{1-x}Se_x$)F thin-film solid solutions indicate that that the chalcogen atom has a significant influence on the fundamental optical transitions in BaCuChF (Fig. 3.4), and GGA DFT calculations provide qualitative support [Fig. 3.1(b)]. As the fraction of the heavy chalcogen *x* increases in BaCu($Ch_{1-x}Ch'_x$)F thin-film solid solutions, the exciton peaks shift to lower energies due to the decrease of the band gap, which we

partially attribute to better overlap of the higher Ch *np* level with the Cu 3*d* atomic orbital. Also, the excitonic peaks become less intense with increase of *x*, due to increased screening of excitons by free carriers. Finally, excitonic peaks in $BaCu(Ch_{1-x}Ch'_x)F$ are broader than in BaCuChF, because of disorder created by the random filling of the chalcogen sites by Ch and Ch' in thin-film solid solutions.

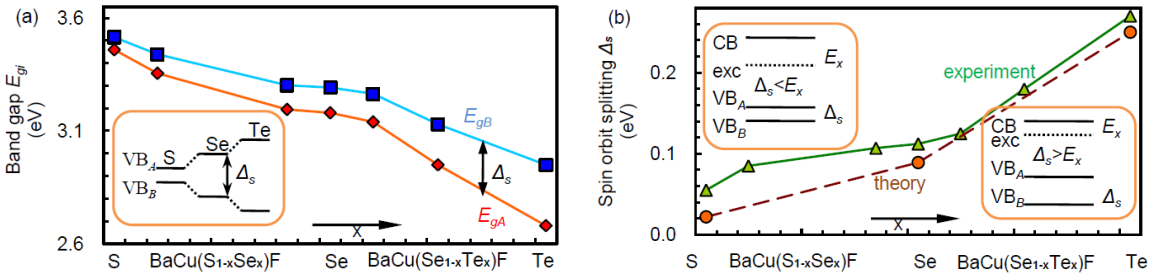

FIG. 3.7. (a) Band gaps and (b) spin-orbit splittings in $BaCu(Se_{1-x}Te_x)F$ and $BaCu(S_{1-x}Se_x)F$. Insets show schematic electronic bands and excitonic levels.

As shown in Fig. 3.7(a), the separation of the band gaps E_{gA} and E_{gB}, obtained from the fit of Eq. 2.3 to the experimental data in Fig. 3.4, increases with increasing *x* in the solid solution, reflecting the energy difference between the spin-orbit split valence bands [Fig. 3.7(a) inset]. Figure 3.7b shows the separation between E_{gA} and E_{gB} as a function of the thin-film solid solution composition. For BaCuChF (Ch = S, Se, Te), experimental separation is larger than the theoretical prediction by about 30 meV, which may be attributed to either imperfections of the thin film samples or to GGA DFT calculation artifacts. Overall, the experimental and theoretical spin-orbit splitting agree better for $BaCu(Se_{1-x}Te_x)F$ than for $BaCu(S_{1-x}Se_x)F$. This is expected,[43] since in $BaCu(S_{1-x}Se_x)F$ binding energy of the excitons is larger than the spin-orbit splitting [Fig. 3.7(b), inset].

3.5 Summary

We have built a consistent model that describes the optical properties of BaCuChF (Ch = S, Se, Te) materials based on their absorption spectra and electronic band structure. According to this model, BaCuChF have two series of 3*D* Wannier-Mott excitons associated with two spin-orbit split valence bands. Spin-orbit splitting increases

with increasing atomic weight of a chalcogen in $BaCu(Ch_{1-x}Ch_x')F$. The high binding energy of the excitons results from the large out-of-plane effective masses of the holes and causes the persistence of excitons above room temperature. In BaCuTeF, the lowest band-to-band transitions are suppressed and the excitons are screened by free holes.

References

[1] K. Ueda, S. Inoue, S. Hirose, H. Kawazoe, H. Hosono, Appl. Phys. Lett. **77**, 2701 (2000).

[2] H. Yanagi, J. Tate, S. Park, C.-H. Park and D. A. Keszler, Appl. Phys. Lett., **82**, 2814 (2003).

[3] Y. Kamihara, H. Hiramatsu, M. Hirano, R. Kawamura, H. Yanagi, T. Kamiya, H. Hosono, J. Am. Chem. Soc. **128,** 10012 (2006).

[4] H. Hiramatsu, K. Ueda, H. Ohta, M. Hirano, M. Kikuchi, H. Yanagi, T. Kamiya, H. Hosono, Appl. Phys. Lett. **91**, 012104 (2007).

[5] H. Yanagi, S. Ohno, T. Kamiya, H. Hiramatsu, M. Hirano, H. Hosono, J. Appl. Phys. **100**, 033717 (2006).

[6] Y. Kamihara, T. Watanabe, M. Hirano, H. Hosono, J. Am. Chem. Soc. **130**, 3296 (2008).

[7] J. F. Wager, D. A. Keszler, R. E. Presley, *Transparent Electronics* (Springer, Berlin, 2008).

[8] M. Yasukawa, K. Ueda, H. Hosono, J. Appl. Phys. **95**, 3594 (2004).

[9] H. Hiramatsu, K. Ueda, H. Ohta, T. Kamiya, M. Hirano, Appl. Phys. Lett. **87**, 211107 (2005).

[10] J. A. Spies, R. Schafer, J. F. Wager, P. Hersh, H. A. S. Platt, D. A. Keszler, G. Schneider, R. Kykyneshi, J. Tate, X. Liu, A. D. Compaan, W. N. Shafarman, Solar Energy Materials & Solar Cells **93**, 1296 (2009).

[11] N. Peyghambarian, S. W. Koch, A. Mysorowicz, *Introduction to Semiconductor Optics*, (Prentice Hall, Englewood Cliffs, NJ, 1993).

[12] K. Ueda, H. Hiramatsu, M. Hirano, T. Kamiya, H. Hosono, Thin Solid Films **496**, 8 (2006).

[13] K. Ueda, S. Inoue, H. Hosono, N. Sarukura, M. Hirano, Appl. Phys. Lett. **78**, 2333 (2001).

[14] T. Kamiya, K. Ueda H. Hiramatsu, H. Kamioka, H. Ohta, M.Hirano, H. Hosono, Thin Solid Films **486**, 98 (2005).

[15] H. Hiramatsu, K. Ueda, K.Takafuji, H. Ohta, M. Hirano, T. Kamiya, H. Hosono, J. Appl. Phys. **94**, 5805 (2003).

[16] K. Ueda, H. Hosono, N. Hamada, J. Phys.: Condensed Matter **16**, 5179 (2004)

[17] J. Tate, P. F. Newhouse, R. Kykyneshi, P. A. Hersh, J. Kinney, D. H. McIntyre, D. A. Keszler, Thin Solid Films **516**, 5795 (2008).

[18] A. Zakutayev, D. H. McIntyre, G. Schneider, D. A. Keszler, C. -H. Park, J. Tate, submitted to Thin Solid Films (2009).

[19] Y. Hishikawa, N. Nakamura, S. Tsuda, S. Nakano, Y. Kishi, and Y. Kuwano, Jpn. J. Appl. Phys. **30**, 1008 (1991)

[20] P. Blaha, K. Schwarz, G. Madsen, D. Kvasnicka, J. Luitz, WIEN2k, An Augmented Plane Wave + Local Orbitals Program for Calculating Crystal Properties (Karlheinz Schwarz, Techn. Universität Wien, Austria), 2001.

[21] M. Weinert, G. Schneider, R. Podloucky, J. Redinger, J. Phys.: Condens. Matter **21**, 084201 (2009).

[22] M. Shishkin, G. Kresse, Phys. Rev. B **75**, 235102 (2007).

[23] G. Kresse, J. Furthmüller, Phys. Rev. B **54**, 11169 (1996).

[24] H. Yanagi, J. Tate, S. Park, C. -H. Park, D. A. Keszler, M. Hirano, H. Hosono, J. Appl. Phys. **100**, 083705 (2006).

[25] J. I. Pankove, *Optical Processes in Semiconductors* (Courier Dover Publications, Mineola, NY, 1975).

[26] R. J. Zollweg, Phys. Rev. **111**, 113 (1958).

[27] A. R. Beal, J. C. Knights, and W. Y. Liang, Journal of Physics C: Solid State Physics **5**, 3531-3539 (1972).

[28] K. Ueda, H. Hiramatsu, H. Ohta, M. Hirano, T. Kamiya, H. Hosono, Phys. Rev. B 69, 155305 (2004)

[29] J. F. Muth, R. M. Kolbas, A. K. Sharma, S. Oktyabrsky, J. Narayan J. Appl. Phys. **85**, 7884 (1999).

[30] A. R. Beal, W. Y. Liang, J. Phys. C: Solid State Phys. **9**, 2459 (1976).

[31] http://www.asiinstr.com/technical/dielectric%20constants.htm

[32] Y. P. Varshni, Physica **34**, 149 (1967).

[33] C.-H. Park, D. A. Keszler, H. Yanagi, J. Tate, Thin Solid Films **445**, 288 (2003).

[34] S. Shionoya, W. M. Yen, *Phosphor Hanbook*, (CRC Press, Boca Raton, FL, 1998).

[35] C.-H. Park, R. Kykyneshi, A. Yokochi, J. Tate, D. A. Keszler, Journal of Solid State Chemistry **180**, 1672 (2007).

[36] A. Walsh, J. L. F. Da Silva, S.-H.Wei, C. Korber, A. Klein, L. F. J. Piper, A. DeMasi, K. E. Smith, G. Panaccione, P. Torelli, D. J. Payne, A. Bourlange, R. G. Egdell, Phys. Rev. Lett. **100**, 167402 (2008).

[37] X.Nie, S.-H.Wei, S. B. Zhang, Phys. Rev. Lett. **88**, 066405 (2002)

[38] P. F. Newhouse, C.-H. Park, D. A. Keszler, J. Tate, P. S. Nyholm, Appl. Phys. Lett. **87**, 112108 (2005).

[39] N. Ueda, H. Maeda, H. Hosono, H. Kawazoe, J. Appl. Phys. **84**, 6174 (1998).

[40] N. W. Ashcroft, N. D. Mermin, *Solid State Physics*, (Holt, Rinehart, and Winston, New York, 1976).

[41] R. Kykyneshi, D. H. McIntyre, J. Tate, C.-H. Park, D. A. Keszler, Solid State Sciences **10**, 921 (2008).

[42] M. P. Marder, *Condensed Matter Physics*, (John Wiley, New York,2000).

[43] Y. Zhang, G. M. Dalpian, B. Fluegel, S.-H. Wei, A. Mascarenhas, X.-Y. Huang, J. Li, L.-W. Wang, Phys. Rev. Lett. **96**, 026405 (2006).

CHAPTER 4

Electronic properties of BaCuChF (Ch = S, Se, Te) surfaces and BaCuSeF/ZnPc interfaces

A. Zakutayev, J. Tate, H. A. S. Platt, D. A. Keszler, C. Hein, T. Mayer, A. Klein, W. Jaegermann

Accepted to the Journal of Applied Physics

4.1 Introduction

Organic light-emitting diodes (OLEDs) and organic photovoltaic (OPV) devices commonly use In_2O_3:Sn (ITO) as a transparent anode because of its excellent transparency, high conductivity, and relatively high work function. An oxygen plasma treatment is often used to increase the work function of the anode, but this process decreases the conductivity of the surface and increases its chemical reactivity, contributing to oxidation and fatigue of functional organic overlayers. To circumvent these issues, *p*-type semiconductors could be useful alternatives to ITO (an *n*-type semiconductor) as the anode in organic optoelectronic devices. In *p*-type semiconductors, the conductivity and work function can increase simultaneously. While *p*-type oxide semiconductors have been considered an attractive approach to realizing such anodes, their *p*-type doping remains quite challenging. As a result, *p*-type oxides are most often used as interlayers between *n*-type ITO and an organic film. For example, a thin NiO layer on an ITO surface leads to increased conversion efficiency of bulk heterojunction solar cells[1] and reduction in the operating voltage of organic light-emitting devices.[2]

P-type chalcogenides appear to offer distinct advantages relative to the oxides as anode materials for organic optoelectronic devices. The chalcogenides have larger conductivities than the oxides with retention of transparency, and their ionization potentials can be broadly tuned on the basis of the chalcogen, e.g., S, Se, or Te, providing a means to tune energy barriers at interfaces. Indeed, the hole injection barrier at the interface between the oxygen-plasma-treated *p*-type LaCuOSe:Mg and N,N'-diphenyl-N,N'-bis (1,1'-biphenyl)-4,4'-diamine (NPB) has already been demonstrated to be lower than the barrier at the ITO/NPB interface.[3]

Development of OLEDs and OPVs requires fundamental understanding of the properties of the interfaces. Interfaces of organic materials with metals, binary semiconductors, and transparent *n*-type semiconductors are well-studied,[4,5] however, the number of reports addressing interfaces with inorganic wide-bandgap *p*-type semiconductors is quite limited. The chalcogenides BaCuChF (Ch = S, Se, Te) comprise one such family of wide-band *p*-type semiconductors that has potential for *p*-type anode applications. Thin films of these materials are transparent through most of the visible

spectrum, and they have a high concentration and mobility of free holes.[6] Optical and transport properties of BaCuChF may be tuned both in powder[7] and thin-film[8] forms, which is attractive for optoelectronic applications. Another significant advantage for organic devices is that the BaCuChF materials do not contain oxygen, which may lead to better contact stability and longer device lifetime.

In this paper, we present a study of BaCuChF (Ch = S, Se, Te) surfaces using photoelectron spectroscopy and report on the interfaces between BaCuSeF and zinc phthalocyanine (ZnPc). This paper is laid out as follows. Experimental details are followed by a discussion of a new synthesis route to BaCuChF powders and pellets, including their compositional, structural, and surface characterization. Next, deposition and characterization of BaCuChF thin films are discussed with a particular emphasis on the surface preparation for the photoelectron spectroscopy experiments. Finally, results of BaCuSeF/ZnPc interfacing experiments are reported.

4.2 Experiments

4.2.1. Sample preparation and characterization

BaCuSF powder was synthesized by grinding $BaCO_3$ (Cerac, 99.9%), BaF_2 (Cerac, 99.9%), and Cu_2S (Strem Chemicals, 99.5%) together in stoichiometric amounts and heating in flowing H_2S (g) (Matheson, 99.5%) at 550 ^oC for 2 h. To prepare BaCuSeF, $BaCO_3$, and BaF_2 were ground with Cu_2Se (Cerac, 99.5%) in stoichiometric proportions and reacted under a mixture of 15% H_2Se (g) - 85% Ar (g) (Air Liquide, 99.8%) flow at 550 ^oC for 2 h. The gas was then switched to Ar (Industrial Welding Supply, 99%), and the powder was heated for another 2 h at the same temperature. BaCuTeF was prepared by combining $BaCO_3$, BaF_2, and Cu_2Te (Cerac, 99.5%) in stoichiometric proportions and grinding with 5 - 20 weight % excess Te (Alfa Aesar, 99.999%) in an Ar-filled plastic glove-bag. After grinding, the mixture was heated at 550 ^oC under flowing 5% H_2 and 95% Ar (Airgas, 99.999%) for 2 h.

BaCuChF powders were cold pressed at 2.7 - 3.6 tonnes in a 25-mm die to form targets for the pulsed laser deposition. The pellets for the photoemission experiments were pressed at 1.8 tonnes in a 9.5 mm die. BaCuSF targets and pellets were heated in a

hot isostatic press (HIP, American Isostatic Presses) for 3 h under 138 MPa of Ar at 750 ^{o}C. BaCuSeF samples were treated in the HIP at 650 - 700 ^{o}C for 3 h with 103 MPa of Ar. BaCuTeF targets and pellets were heated for 2 h at 780 ^{o}C in the HIP with 103 MPa of Ar. Final densities were approximately 70% of theoretical values.

BaCuChF thin films were prepared by pulsed laser deposition (PLD) in a vacuum chamber with a base pressure of 10^{-9} Torr without introducing background gas. BaCuChF sintered targets were ablated using a pulsed 1 J/cm^2 beam from a KrF excimer laser operating at a wavelength of 248 nm with a repetition rate of 7 Hz. Si (001) and amorphous silica (*a*-SiO_2) substrates were heated to 350 ^{o}C and rotated 5 cm above the target during the deposition. The films were 200 nm thick, as measured by a surface profilometer.

X-ray diffraction (XRD) experiments were performed using a Rigaku MiniFlex II diffractometer with Cu *K*α radiation. The resulting XRD patterns were corrected for the zero-point shift using Si peaks. Electron probe microanalysis (EPMA) on the BaCuChF pellets and films was performed using a Cameca SX-100 microprobe. Each BaCuChF pellet was sampled over several hundred microns. At least fourteen points were used to calculate the final elemental ratios of the pellets, resulting in a typical standard deviation of 2 to 4 at. %. The films were measured with three accelerating voltages (12, 16, and 22 KV). The average was taken over five points on each of the films. These data were modeled using Stratagem software. The absolute uncertainty of the EPMA measurements was ±5 %.

Transport properties were measured for the thin films on *a*-SiO_2 prepared under the same conditions as the samples on Si (001) substrates. Resistivity and Hall effect were measured using a Lakeshore 7504 system in a field of 20 KG. The Seebeck coefficient was measured using a custom setup with the temperature difference of 3 - 5 K between hot and cold ends of the sample. Optical reflection and transmission of the samples were measured in the 200 - 2500 nm spectral region using an Ocean Optics visible-near infrared spectrometer.

4.2.2. Photoelectron spectroscopy

The photoelectron spectroscopy (PES) experiments were performed using the Darmstadt Integrated System for Solar energy research (DAISY-SOL).[9] Before acquiring data, the surfaces of the BaCuChF pressed pellets were polished with 1000-grit sandpaper. The polishing procedure took 5 minutes, and the samples were in a vacuum of 10^{-6} mbar within about 5 minutes of polishing.

BaCuChF thin films were protected from ambient atmosphere during transportation from Corvallis (OR), USA to Darmstadt, Germany. For this purpose, amorphous 1000-nm Se capping layers were prepared by PLD without breaking vacuum. The samples were also contained in plastic vacuum packaging during the transportation. BaCuSeF samples were decapped by heating in vacuum (10^{-8} mbar) for 10 minutes at 200 ^{o}C (T_{melt} (Se) = 221 ^{o}C). Higher temperatures increased surface non-stoichiometry, and shorter heating times left Se islands on the surface, as confirmed by EPMA. Decapping of BaCuSF and BaCuTeF samples was followed by sputter-cleaning with an additional subsequent heating for recrystallization of the surfaces. The sputter-cleaning was done by rastering a 1-μA beam of 1-keV Ar ions incident at 45° to the surfaces over a 25 mm^2 area of the sample.

X-ray- and ultraviolet photoemission spectroscopy experiments (XPS/UPS) were performed in an Escalab-250 system using the *K*α line of an Al x-ray source with a monochromator (1486.6 eV, 0.4 eV energy resolution) and He I line from a He discharge lamp (21.2 eV, 0.2 eV energy resolution). During the UPS measurements, an electric potential of - 6 V was applied to the samples. The Fermi level of the system was calibrated with the $3d_{5/2}$ line of a clean Ag sample (368.27 eV). XPS core level spectra were recorded over an energy range at least 10 eV larger than the full width at half maximum of each peak, but only a portion of each spectrum is shown. The work function and the valence band maxima were found from extrapolation of the linear portion of the secondary electron cut-off and the valence band onset to background level. The uncertainty of the binding energy determination was ± 0.05 eV. The surface stoichiometry of the BaCuChF films was determined from the integrated area under the

XPS core level peaks using sensitivity factors for the system. The absolute uncertainty of the surface composition determined this way was typically ±10 %.

4.2.3. Interfacing experiments

ZnPc layers were deposited at room temperature on decapped BaCuSeF thin film surfaces by thermal evaporation of ZnPc powders heated at 393 ^{o}C. After each deposition step the samples were transferred in vacuum to the PES chamber and XPS/UPS spectra were recorded. ZnPc was deposited until the layer was thick enough that no significant changes in the binding energies of the XPS peaks of Zn, N, and C were observed.

The spectra of the BaCuSeF valence band (VB) and the ZnPc HOMO were obtained by subtracting the UPS reference spectra of the clean BaCuSeF films and that of a thick ZnPc layer from the measured BaCuSeF/ZnPc spectra for each step of the interfacing experiment. The energy differences between the UPS HOMO/VB and the XPS core levels in the reference spectra were assumed to be constant during the course of the interfacing experiment. These energy differences were used to determine the bending of the BaCuSeF valence band maxima (VBM) and ZnPc highest occupied molecular orbital (HOMO) from the XPS data. Throughout this paper, we use the ZnPc HOMO maximum, but the HOMO onset (0.4 eV higher) was used for the calculation of the hole injection barrier as often reported in the literature.[10,11] The hole injection barrier was calculated at 25 Å coverage, where all the ZnPc core levels started shifting in parallel.

For ZnPc thickness calculations, the area under the XPS peaks A_i was fit using expressions $A_i = A_{i0}\, exp\,(- r_i\, t / d_{i0})$ for BaCuSeF peaks, and $A_i = A_{i0}\, [1 - exp\,(- r_i\, t / d_{i0})]$ for ZnPc peaks, where i is peak index, t is ZnPc deposition time, r_i is the deposition rate and d_i is the energy-dependent inelastic mean free path (IMFP). The IMFP of electrons in ZnPc was calculated using NIST Electron Inelastic-Mean-Free-Path Database (v. 1.1). Deposition rates r_i extracted from these fits averaged to 0.2 Å/sec, which was used to calculate the thickness of ZnPc layer for each deposition step.

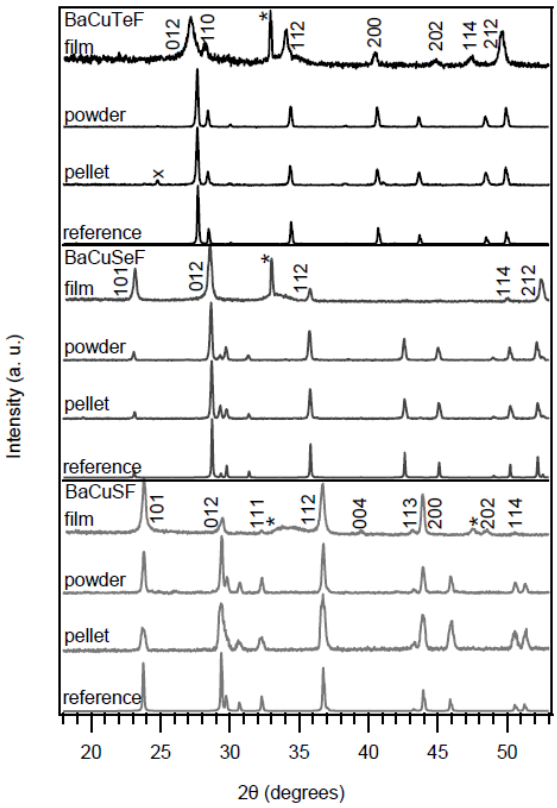

FIG. 4.1 BaCuChF x-ray diffraction patterns of thin film, powder, pellet samples, and simulated XRD patterns. Stars denote Si substrate peaks. A cross denotes BaF_2 impurity peak.

4.3 Results and discussion

4.3.1. Powders and pellets

Syntheses of BaCuChF powders by solid state reaction between binary precursors in sealed ampoules has been previously reported,[12,13] but this method led to chalcogen-poor samples with trace oxygen impurities. These problems likely result from the oxidized binary precursors, high defect concentrations in the synthesized BaCuChF powders, and subsequent oxidation of these powders when exposed to air. Flowing H_2Ch gas syntheses of the BaCuSF and BaCuSeF compounds solves these problems. At elevated temperatures, the large excess of flowing H_2Ch gas strips away oxygen and minimizes the number of Ch vacancies in the resulting BaCuChF powder:

$$BaCO_3(s) + H_2Ch(g) \rightarrow BaCh(s) + CO_2(g) + H_2O(g) \qquad (4.1)$$

BaCuSeF powders contained excess Se, and a subsequent anneal in Ar was required to remove it. H_2Te decomposes above 0 ^oC, so it was not possible to synthesize BaCuTeF by this method. Nevertheless, the XRD data collected from all three BaCuChF powders were consistent with the reference patterns, and no significant impurity peaks were observed (Fig. 4.1). Unit cell parameters calculated from the measured data are all within 0.6% of published values.[14]

TABLE 4.1. Composition of BaCuChF pressed pellets (PP) and thin films (TF) measured using electron probe microanalysis. Ideal stoichiemtery has each element at 25 at. % and O at 0 at. %.

EPMA	BaCuSF		BaCuSeF		BaCuTeF	
at.%	PP	TF	PP	TF	PP	TF
Ba	25	25	24	26	21	24
Cu	25	22	25	23	20	20
Ch	24	21	25	24	21	22
F	24	26	24	24	34	26
O	2	6	2	3	4	7

EPMA data collected from the sintered BaCuChF pressed pellets are summarized in Table 4.1. From these data, elemental ratios of BaCuSF and BaCuSeF are found to be within one standard deviation of the expected values. There is a significant excess of F with respect to each of the other elements in the BaCuTeF pellets, which is consistent with the small amount of BaF_2 observed in the XRD pattern of the BaCuTeF pellet (Fig. 4.1). For all three BaCuChF materials, the oxygen concentration in the pressed pellets (2-4%) is comparable to the standard deviations of the EPMA experiments (2-4%).

TABLE 4.2. Binding energies of the core levels and the valence band maxima of BaCuChF pellets. For the Ch atoms, S $2p_{3/2}$, Se $3d_{5/2}$ and Te $3d_{5/2}$ binding energies are reported.

BE (eV)	BaCuSF	BaCuSeF	BaCuTeF
Ba $3d_{5/2}$	779.88	779.86	780.03
Cu $2p_{3/2}$	932.53	932.50	932.80
Ch	161.15	53.51	572.11
F 1*s*	684.08	684.11	684.14
VBM	0.30	0.20	0.10

TABLE 4.3 Composition of BaCuChF pressed pellets (PP), and decapped (d) or sputter-cleaned (s) thin films (TF) measured using x-ray photoemission spectroscopy. Ideal stoichiemtery has each element at 25 at. % and O at 0 at. %.

XPS	BaCuSF		BaCuSeF		BaCuTeF	
at.%	PP	TF(s)	PP	TF(d)	PP	TF(s)
Ba	25	37	26	26	21	30
Cu	14	13	17	28	12	18
Ch	17	26	13	27	23	26
F	15	16	13	16	11	19
O	27	9	30	3	30	5
C	2	0	2	0	4	0

Binding energies of the XPS core levels of the BaCuChF pressed pellets are summarized in Table 4.2. The Cu 2$p_{3/2}$ and the F 1*s* binding energies in BaCuChF are close to those in Cu_2S (932.6 eV),[15] Cu_2Se (932.5 eV),[16] Cu_2Te (932.94 eV),[17] and BaF_2 (684.2 eV),[18] due to the similar crystallographic and electronic environments. Compositions measured by XPS (Table 4.3) demonstrate that the surfaces of the BaCuSF and BaCuSeF pellets are Ba-rich, whereas the surface of the BaCuTeF pellet is Ba- and Te-rich; each of the samples was found to contain approximately 30 at. % O. Oxidation results in high-binding-energy satellites for the Te 3*d* peaks (Fig. 4.2a), and a low-binding-energy component for the O 1*s* peak (Fig. 4.2b). These features are consistent with the presence of TeO_2. TeO_2 peaks are not present in the XRD patterns of the BaCuTeF pellets (Fig. 4.1), indicating a thin oxide layer on the BaCuTeF surface. Similarly, the S 2*p* and Se 3*d* peaks have high-binding-energy shoulders, and the corresponding O 1*s* peaks have low-binding-energy components, indicating the presence of S-O and Se-O bonding interactions on the BaCuSF and BaCuSeF surfaces, respectively. The S- and Se-shoulders in the BaCuSF and BaCuSeF XPS spectra are much weaker than the TeO_2 peaks in the BaCuTeF spectrum, which may be rationalized by considering Gibbs free energies of different phases of Ch-O compounds. In the vicinity of the synthesis temperature (527 ^oC) TeO_2 exists in solid phase, whereas all S- and Se oxides exist in gas phase.[19] Therefore, solid Te-O layer may form on the surfaces during the flowing synthesis, whereas S-O and Se-O layers may form only after the

synthesis, when the samples are exposed to the atmosphere. Since the BaCuChF surfaces are Ba-rich (Table 4.3), it is likely that Ba-O is also present at the BaCuChF surfaces. BaO satellites do not appear in the XPS, probably since the binding energies of the Ba $3d_{5/2}$ peaks in BaO and BaCuChF are very similar. Clearly, the BaCuChF grain boundaries are oxidized, and our previous electrical transport measurements are consistent with this result.[8] The BaCuChF surfaces are also contaminated with atmospheric carbon-containing molecules, which is evident from a broad C 1*s* peak at 284.58 eV (Fig. 4.2c). A broad O 1*s* peak at 531.35 eV (Fig. 4.2b) also indicates the presence of $O_xC_yH_z$ species on the surface. These two lines were not sufficiently intense to perform a deconvolution to determine their origin more precisely. A low-intensity component of the C 1*s* peak at 289.37 is consistent with the C 1*s* line in $BaCO_3$ at 289.4 eV.[20] This may be a result of using $BaCO_3$ precursors in the BaCuChF flowing-gas synthesis, or a consequence of the reaction of Ba-rich grain boundaries with atmospheric CO_2.

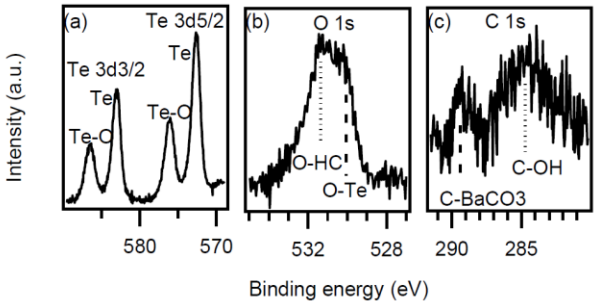

FIG. 4.2 X-ray photoemission spectra of Te 3*d*, O 1*s* and C 1*s* core levels in BaCuTeF pressed pellets. The surfaces contain some oxygen- and carbon-based species.

XPS VB spectra of all three BaCuChF are shown in Fig. 4.3, and the binding energies of the VBM are listed in Table 4.2. The three VB spectra are similar to each other; their spectral features are assigned on the basis of the partial density of states calculated using density functional theory (DFT).[13,21] Spectral positions of the peaks predicted by DFT and measured by XPS agree well, but their relative intensities are not consistent with each other. For example, F 2*p* and Cu 3*d* peaks are predicted to have similar magnitude, but XPS measurements indicate that the Cu 3*d* peak is much stronger

(Fig. 4.3). This can be explained by the larger x-ray ionization cross section of *d*-states compared to *p*-states. The position of the surface Fermi level decreases across the BaCuSF - BaCuSeF - BaCuTeF series in agreement with bulk Fermi level positions trend calculated from the experimental concentration of free holes along with the DFT density of states.[22] However, the XPS results are generally higher than the theoretical prediction, which is likely caused by the bending of BaCuChF bands downward at the surface. This band bending may be result from the surface oxidation mentioned earlier. Work functions of the polished BaCuChF pellets could not be reliably determined by UPS because of the presence of atmospheric adsorbates on the surfaces.

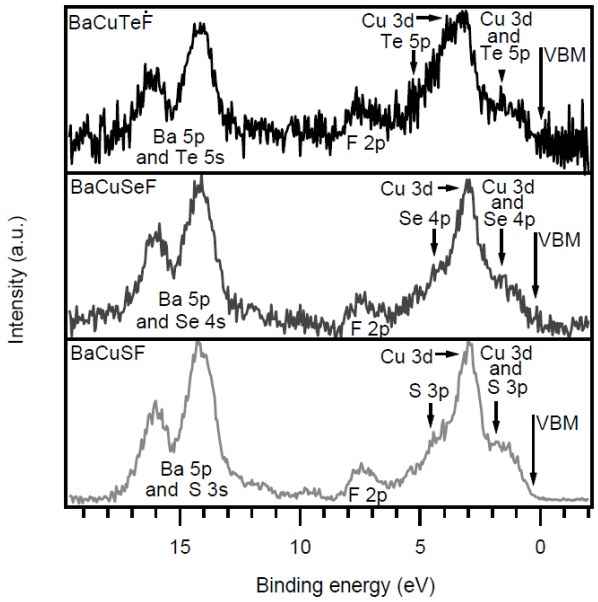

FIG. 4.3 X-ray photoemission spectra of the valence band of BaCuChF pellets. The peaks are assigned based on density functional theory calculations.

4.3.2. Thin films

The composition of the BaCuChF thin films on Si (001) measured by EPMA is shown in Table 4.1. All the samples are nearly stoichiometric, despite the fact that the BaCuTeF target was F-rich. We attribute the decrease of the F content in the BaCuTeF thin films largely to the low ablation efficiency of the BaF_2 impurity because of its high band gap. The concentration of oxygen in all BaCuChF thin-film samples was higher

than in the pellets, probably due to the higher surface-to-volume ratio. The films are somewhat Cu-poor. Cu vacancies likely generate free holes, leading to *p*-type nature of BaCuChF demonstrated by positive thermopower. Seebeck coefficients for the thin films on fused silica were 335 μV/K for BaCuSF, 255 μV/K for BaCuSeF, and 80 μV/K for BaCuTeF. BaCuTeF thin films on *a*-SiO_2 had a Hall mobility of 0.52 cm^2/Vs, concentration of free holes of $2.2x10^{20}$ cm^{-3} , resulting in a conductivity of 30 S/cm. The Hall coefficient could not be reliably determined for polycrystalline BaCuSF and BaCuSeF samples, but their conductivities were 0.3 S/cm and 0.001 S/cm respectively. Thin films of 200-nm thickness were on average 75% transparent to 500-2500 nm light. Reflection-corrected transmission $T/(1-R)$ was ~90% in this spectral range.

As shown in Fig. 4.1, the thin film XRD patterns have no impurity peaks, but they are shifted to smaller 2θ values than the powder XRD patterns, indicating larger unit cells. We attribute the unit cell expansion to the stress imposed by creation of native defects during thin film deposition. The increase of the unit cell volume is consistent with the results of the density functional theory defect calculation that will be published elsewhere. A similar increase of the unit cell parameters was reported for BaCuTeF thin films on fused silica[23] and BaCu(Se_xS_{1-x})F thin film solid solutions on MgO.[8]

According to XPS measurements, surfaces of poorly protected BaCuChF thin films were significantly oxidized and contaminated, so it was crucial to protect them from the influence of the atmospheric conditions. Four protection methods and their combinations have been investigated, including (i) deposition of a 1000-nm selenium capping layer, (ii) sealing in a vacuum package, (iii) direct transfer from the loadlock into a nitrogen-filled glove-bag for sealing, and (iv) storage in nitrogen atmosphere during the transportation. After a two-week storage, only the films that were protected with the Se capping layer and sealed in a vacuum package were largely free of surface oxide. The concentration of oxygen on the surface of these samples measured by XPS (Table 4.3) was close to the concentration of oxygen in the bulk measured by EPMA (Table 4.1). These results demonstrate that a 1000-nm Se capping layer provides sufficient protection for short periods of atmospheric exposure; similar findings have been reported for $CuInSe_2$ thin films.[24]

In the case of the BaCuSeF thin films, evaporation was sufficient to remove the Se capping layer from the surface, but decapped BaCuSeF thin film surfaces were F-poor. These films exhibited a Fermi level positioned 0.25 eV above the valence band maximum, a work function of 4.85 eV, and a resulting ionization potential of 5.10 eV. This is an average ionization potential because BaCuSeF thin films were polycrystalline. BaCuSeF pressed pellets reported previously had a similar Fermi level (0.3 eV), but lower work function (3.6 eV) and ionization potential (3.9 eV).[21] These differences are larger than experimental uncertainties and may result from different magnitudes of surface dipoles caused by different synthesis routes, different types of samples and different surface preparation protocols. Larger surface roughness of the pressed pellets compared to thin films may also contribute to smaller work functions of the pellets. Regardless of the reason, the BaCuSeF ionization potentials reported here and previously are smaller than those of related $Cu_{2-x}Se$ (5.35 eV)[25] and $CuInSe_2$ (5.65 – 6.10 eV).[26,27] The difference in ionization potentials between BaCuSeF and other Cu-Se-based materials may also be caused by the upward VB shift associated with the transfer of charge from Ba-F layers to the Cu-Se layers in the aniosotropic BaCuSeF structure. The ionization potential of BaCuSeF is larger compared to BaSe (4.7 eV),[28] as expected from more ionic nature of BaSe. The anisotropic layered crystal structure of BaCuSeF also results in polar surfaces, which may lead to a reconstruction and change the ionization potential of BaCuSeF.

In the cases of BaCuTeF and BaCuSF thin films, no heating conditions were found to completely remove the Se capping layer. Sputter-cleaning removed most of the residual Se, but changed the shape of Cu *LMM* Auger line and resulted in preferential removal of light Cu and F atoms. Subsequent heating restored the expected shape of Cu *LMM* line, but it did not significantly change the surface composition (Table 4.3). Resulting low work functions (3.2 - 3.5 eV) are not intrinsic for BaCuSF and BaCuTeF, because the surfaces of the samples were destroyed by the sputter-cleaning, as confirmed by low work functions of sputtered BaCuSeF surfaces. From these results, we conclude that capping and subsequent removal of S and Te layers should be a better way to prepare representative BaCuSF and BaCuTeF surfaces.

4.3.3. Interfaces

Metal phthalocyanines (ZnPc, CuPc, NiPc, *etc.*) are used in optoelectronic devices, often in direct contact with the anode.[10,29] We chose ZnPc for the interfacing experiments, because ITO/ZnPc interfaces have already been studied by XPS,[10] and these experiments provide good comparisons for the present work. CuPc is more commonly used in OLEDs, but using ZnPc prevents interference of the XPS Cu core level signals from CuPc and BaCuChF. Since the HOMO of CuPc and ZnPc and the VB of $Cu_{1.7}Se$ and BaCuSeF have similar character,[21,30] published $Cu_{1.7}Se$/CuPc UPS interfacing experiments[11] may be also compared to this work.

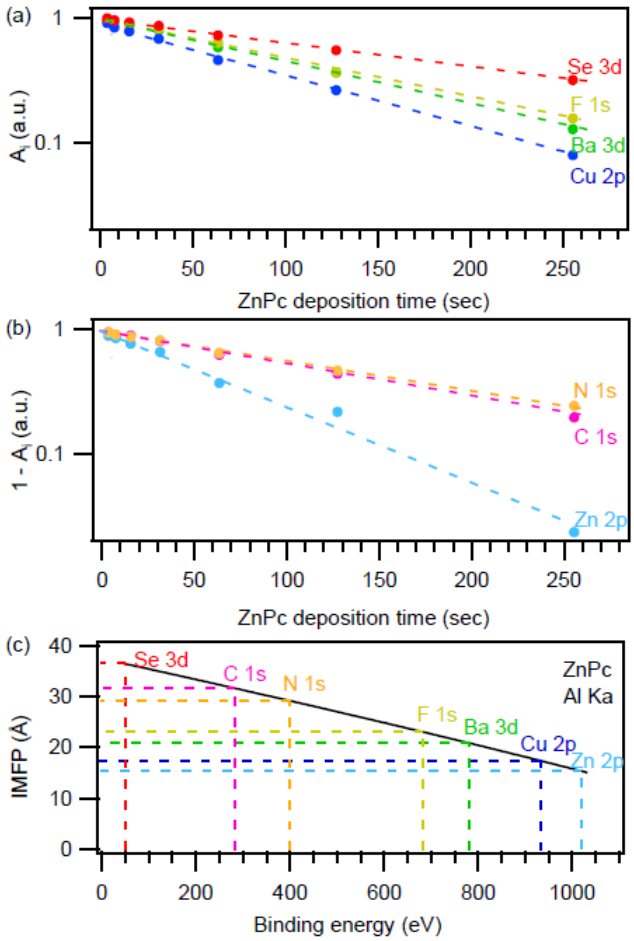

FIG. 4.4 (a) Normalized area under the BaCuSeF XPS, and (b) one minus normalized area under the ZnPc XPS peaks. c) Inelastic mean free path of photoelectrons in ZnPc as a function of their binding energy for Al *K*α excitation radiation. Dashed color-coded lines are guides for the eye.

Stepwise deposition of ZnPc on the decapped BaCuSeF surfaces resulted in intensity attenuation of the BaCuSeF spectra along with increase of intensity of the ZnPc spectra. Normalized area under the BaCuSeF XPS peaks, and one minus normalized area under the ZnPc XPS peaks, are shown in Fig. 4.4a and Fig. 4.4b as a function of ZnPc deposition time. The high-binding-energy peaks change intensity faster than the low-binding-energy peaks, which is consistent with the energy dependence of the inelastic mean free path of photoelectrons in ZnPc (Fig. 4.4c). This consistency indicates that there is no interdiffusion at the BaCuSeF/ZnPc interface.

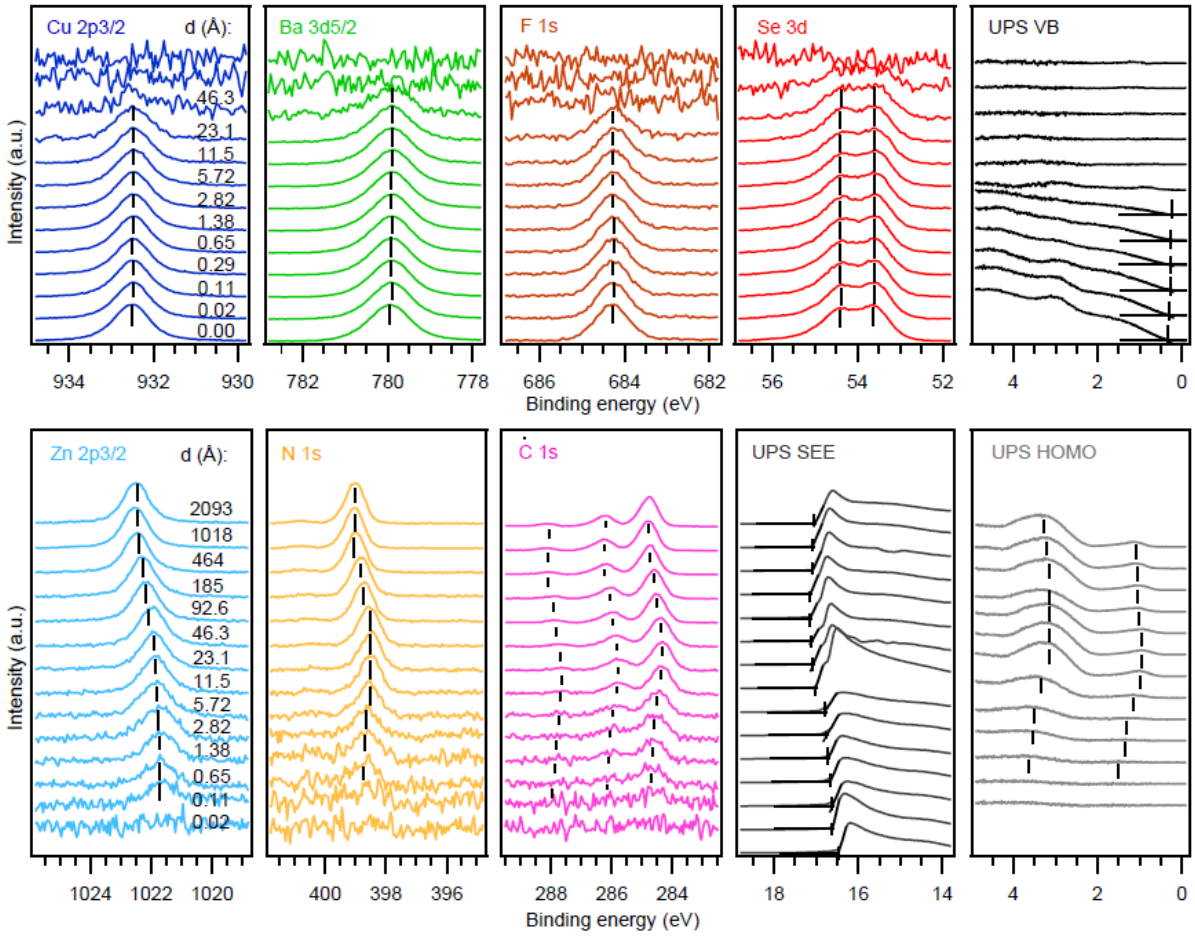

FIG. 4.5 Photoemission spectra of BaCuSeF and ZnPc for different steps of the interfacing experiment. ZnPc thicknesses indicated in the first panel are the same for all other panels in a row. The vertical lines indicate binding energies used to plot Fig. 4.6. The color-coding is the same as in Fig. 4.4.

As shown in Fig. 4.5, the photoemission spectra shift as the BaCuSeF/ZnPc interface is formed, but their shapes do not change. The area under all core level spectra was normalized to 1 to make the shapes of the spectra more evident. No chemical reaction occurs at the BaCuSeF/ZnPc interface, because the C 1*s* peak has a characteristic line shape with three components for all ZnPc thicknesses.[31] The spectral positions of the XPS core level peaks of a thick ZnPc layer (1022.43 eV for Zn $2p_{3/2}$, 398.99 eV for N 1*s* and 284.76 eV for C 1*s* lines), its UPS HOMO binding energy (1.1 eV), and its work function (4.15 eV) all favorably agree with typical values reported in the literature for this material.[32] The BaCuSeF thin film spectra also do not show any evidence of a chemical reaction, and the XPS binding energies (Fig. 4.5) are consistent with those of the pellets (Table 4.2).

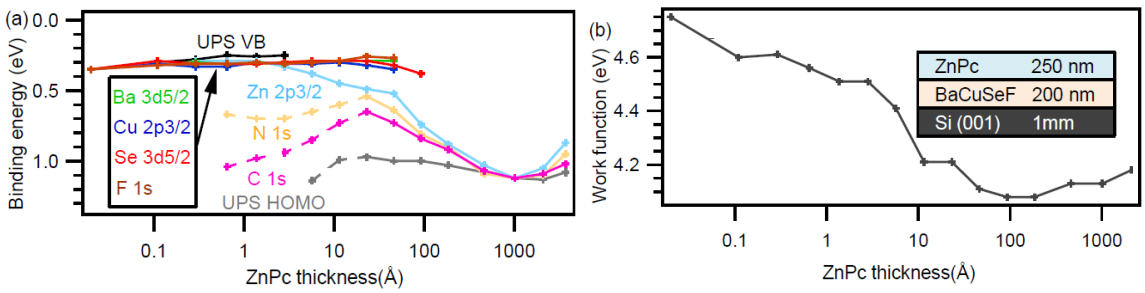

FIG. 4.6 (a) Binding energy of the VB of BaCuSeF and the HOMO of ZnPc measured by UPS and determined from different XPS core level spectra. (b) Work function of the BaCuSeF/ZnPc interface. Color-coded lines are guides for the eye and the dashed portion of the N, C, and HOMO lines below 25 Å represents the charge transfer shift. Note that the abscissa is logarithmic. The final configuration of the sample is schematically depicted in the inset.

The shift of the ZnPc XPS peaks with increasing thickness of the ZnPc layer is caused by a charge transfer. Starting from a thick ZnPc layer and moving toward the interface, the XPS core levels and UPS HOMO of ZnPc shift, in parallel, to lower binding energies, over the range of 100 - 1000 Å depending on the preparation of the BaCuSeF surface. Since no shift of the BaCuSeF electronic states is observed (Fig. 4.5), the charge transfer must occur to BaCuSeF surface states. The electrons transfer from N and C atoms, because the HOMO and 1*s* spectra of N and C shift to a higher binding

energy at a ZnPc coverage of less than 25 Å. Zn states do not contribute to the HOMO of ZnPc, thus the Zn $2p_{3/2}$ core level shifts to a lower energy below 25 Å. The secondary electron edge shifts to a higher binding energy with increasing ZnPc thickness, which corresponds to a lowering of the work function and to the proposed direction of the charge transfer. The summary of the changes of the binding energies and the work functions discussed above are shown in Fig. 4.6. We conclude that the transfer of valence electrons from individual ZnPc molecules into BaCuSeF surface traps leads to a non-parallel shift of the ZnPc electronic states, causes the change of the work function for coverage less than 25 Å, and results in an upward bending of the ZnPc states toward the interface.

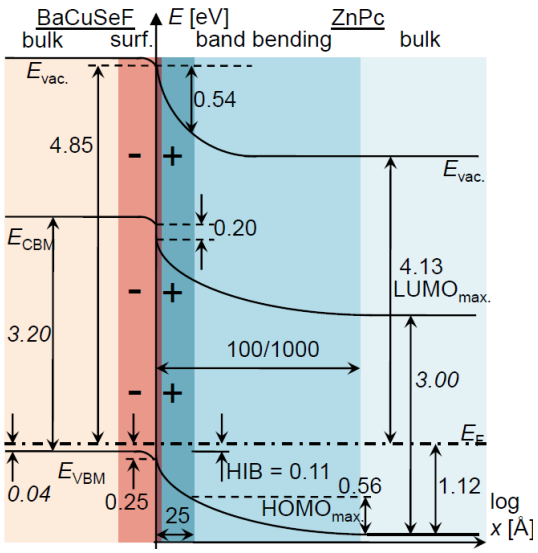

FIG. 4.7 BaCuSeF/ZnPc band diagram. The VBM/HOMO and the vacuum level alignments are found from the data in Fig. 4.6. The band gap values are taken from literature. The bulk Fermi level of BaCuSeF is calculated from the DFT density of states and the concentration of free holes. Note that the abscissa is logarithmic.

A detailed BaCuSeF/ZnPc band alignment diagram is presented in Fig. 4.7. The right-hand side (ZnPc side) of the diagram was plotted using averages of the data shown in Fig. 4.6. The left-hand side (BaCuChF side) consists of only two data points, “surface” (measured by XPS/UPS) and “bulk” (calculated from the BaCuSeF density of states and the carrier concentration)[22], so the horizontal axis on the left-hand side in Fig. 4.6 is

arbitrary. An offset between the conduction band (CB) of BaCuSeF and the lowest unoccupied molecular orbital (LUMO) of ZnPc was calculated using the BaCuSeF band gap value[22] and the ZnPc HOMO-LUMO energy difference[32] found in the literature. The hole injection barrier, found as the BE of the ZnPc HOMO onset at 25 Å coverage is only 0.11 eV. This barrier is lower than at the ITO/ZnPc interface[10] and at the oxygen plasma treated $Cu_{1.7}Se$/CuPc interface.[11] The alignment of BaCuSeF bands with ZnPc states is favorable for efficient hole extraction in photovoltaic devices. Therefore BaCuSeF may be a better anode for OLEDs and OPV devices than ITO and $Cu_{1.7}Se$. We believe that the low hole injection barrier and favorable band alignment is due to the absence of excess oxygen at the BaCuSeF/ZnPc interface. A similar result should be possible with other *p*-type Cu-Se-based materials, but only if their surfaces are protected from oxidation.

4.4 Summary

BaCuChF (Ch = S, Se, Te) powders synthesized from $BaCO_3$ precursors exhibit improved stoichiometries relative to similar powders synthesized by other routes. According to XPS measurements, the surfaces of BaCuChF pellets are oxidized upon exposure to atmospheric conditions. Deposition of a Se capping layer effectively limits this oxidation for BaCuSeF thin films. Dacapped BaCuSeF surfaces are free of O and C, F-poor, and have work functions of 4.85 eV. The BaCuSeF/ZnPc interface is chemically inert, exhibiting a hole injection barrier of 0.11 eV. These properties should afford improved device performance for OLEDs and OPVs in comparison to those achieved with ITO and $Cu_{1.7}Se$ electrodes. Thin film deposition and interface fabrication must be carefully controlled for oxygen incorporation to realize optimum performance.

References

[1] M. D. Irwin, D. B. Buchholz, A. W. Hains, R. P. H. Chang, and T. J. Marks, Proc. Natl. Acad. Sci. U. S. A., **105**, 2783 (2008).

[2] S. Tokito, K. Noda, and Y. Taga, J. Phys. D **29**, 2750 (1996).

[3] H. Yanagi, M. Kikuchi, K.-B. Kim, H. Hiramatsu, T. Kamiya, M. Hirano, and H. Hosono, Organic Electronics **9**, 890 (2008).

[4] J. C. Scott, J. Vac. Sci. Technol. A **21**, 521 (2003).

[5] N. Papageorgiou, E. Salomon, T. Angot, J.-M. Layet, L. Giovanelli, and G. L. Lay, Prog. Surf. Sci. 77, 139 (2004).

[6] J. Tate, P. F. Newhouse, R. Kykyneshi, P. A. Hersh, J. Kinney, D. H. McIntyre, and D. A. Keszler, Thin Solid Films **516**, 5795 (2008).

[7] C.-H. Park, D. A. Keszler, H. Yanagi, and J. Tate, Thin Solid Films **445**, 288 (2003).

[8] A. Zakutayev, D. H. McIntyre, G. Schneider, D. A. Keszler, C.-H. Park, and J. Tate, submitted to Thin Solid Films.

[9] J. Fritsche, A. Klein, and W. Jaegermann, Adv. Eng. Mater. **7,** 914 (2005).

[10] Y. Gassenbauer and A. Klein, J. Phys. Chem. B **110**, 4793 (2006).

[1 1] H. Hiramatsu, I. Koizumi, K.-B. Kim, H. Yanagi, T. Kamiya, M. Hirano, N. Matsunami, and H. Hosono, J. Appl. Phys. **104**, 113723 (2008).

[12] H. Yanagi, J. Tate, S. Park, C.-H. Park, and D. A. Keszler, Appl. Phys. Lett. **82**, 2814 (2003).

[13] C.-H. Park, R. Kykyneshi, A. Yokochi, J. Tate, and D. A. Keszler, J. Solid State Chem. **180**, 1672 (2007).

[14] W. J. Zhu, Y. Z. Huang, F. Wu, C. Dong, H. Chen, and Z. X. Zhao, Mater. Res. Bull. **29**, 505 (1994).

[15] D. Brion, Appl. Surf. Sci. **5**, 133 (1980).

[16] D. Cahen, P. J. Ireland, L. L. Kazmerski, and F. A. Thiel, J. Appl. Phys. **57**, 4761 (1985).

[17] B. Späth, K. Lakus-Wollny, J. Fritsche, C. S. Ferekides, A. Klein, and W. Jaegermann, Thin Solid Films **515**, 6172 (2007).

[18] A. Gauzzi, H. J. Mathieu, J. H. James, and B. Kellett, Vacuum **41**, 870 (1990).

[19] I. Barin, F. Sauert, E. Schultze-Rhonhof, and W. Shu Sheng. *Thermochemical Data of Pure Substances* (VCH, New York, 1993).

[20] A. B. Christie, J. Lee, I. Sutherland, and J. M. Walls, Appl. Surf. Sci. **15**, 224 (1983).

[21] H. Yanagi, J. Tate, S. Park, C.-H. Park, D. A. Keszler, M. Hirano, and H. Hosono, J. Appl. Phys. **100**, 083705 (2006).

[22] A. Zakutayev, R. Kykyneshi, G. Schneider, D. H. McIntyre, and J. Tate, submitted to Phys. Rev. B.

[23] R. Kykyneshi, D. H. McIntyre, J. Tate, C.-H. Park, and D. A. Keszler, Solid State Sci. **10**, 921 (2008).

[24] T. Schulmeyer, R. Hunger, A. Klein, W. Jaegermann, and S. Niki, Appl. Phys. Lett. **84**, 3067 (2004).

[25] D. F. Marron, T. Glatzel, A. Meeder, T. Schedel-Niedrig, S. Sadewasser, and M. C. Lux-Steiner, Appl. Phys. Lett. **85**, 3755-3757 (2004).

[26] S. Siebentritt, U. Rau, *Wide-Gap Chalcopyrites*, (Springer, Berlin, 2006).

[27] T. Schulmeyer, Ph.D. Thesis, Technische Universität Darmstadt, 2005

[28] R. J. Zollweg, Phys. Rev. **111**, 113 (1958).

[29] L. S. Hung and C. H. Chen, Mater. Sci. Eng., R **39**, 143 (2002).

[30] Z. Liu, X. Zhang, Y. Zhang, and J. Jiang, Spectrochim. Acta, Part A **67**, 1232 (2007).

[31] H. Peisert, M. Knupfer, T. Schwieger, and J. Fink, Appl. Phys. Lett. **80**, 2916 (2002).

[32] U. Weiler, T. Mayer, W. Jaegermann, C. Kelting, D. Schlettwein, S. Makarov, and D. Wöhrle, J. Phys. Chem. B **108**, 19398 (2004).

[33] A. Kahn, N. Koch, and W.Gao, J. Polym. Sci., Part B **41**, 2529 (2003).

CHAPTER 5

Band alignment at the BaCuSeF/ZnTe interface

A. Zakutayev, J. Tate, H. A. S. Platt, D. A. Keszler, A. Barati, A. Klein, W. Jaegermann.

Accepted to Applied Physics Letters

5.1 Introduction

One of the contemporary challenges of applied physics is the advancement of photovoltaic (PV) technologies. For example, development of *p*-type windows for *p*-*i*-*n* chalcogenide solar cells is currently needed to improve efficiencies. An ideal *p*-window layer would have (i) a high concentration of free holes for higher conductivity, (ii) a bandgap wider than the absorber, *i*-layer, (iii) a small valence-band (VB) offset relative to the absorber for facile hole extraction, (iv) a large conduction band (CB) offset relative to the absorber to reflect electrons, and (v) a chemically graded interface to limit the formation of interfacial states.[1] ZnTe is one studied *p*-window material in CdTe solar cells.[2,3] Cu and Cu_xTe_y also form Ohmic contacts to CdTe, but their band alignments are not ideal.[4,5]

Here we propose using chalcogen-based transparent conductors,[6] such as BaCuChF (Ch = S, Se, Te)[7,8] for anode applications in chalcogenide *p*-*i*-*n* PV devices. These materials have high concentrations of free holes (10^{18} – 10^{20} cm^{-3})[9,10] and tunable[10,11] wide[12] optical bandgaps (2.9 – 3.5 eV). BaCuChF are likely to form graded interfaces with the chalcogenide absorbers since these materials contain chalcogen atoms. However, to date, the band alignment of BaCuChF with inorganic compounds has not been studied. In this letter, we report x-ray- and ultraviolet-photoemission spectroscopy results (XPS/UPS) for BaCuSeF/ZnTe interfaces, and discuss possible applications of BaCuChF in chalcogenide solar cells based on CdTe, $Cu(InGa)Se_2$ (CIGS), and Cu_2ZnSnS_4 (CZTS) absorbers.

5.2 Experiment

BaCuSeF thin films (200 nm) were prepared by pulsed laser deposition (PLD) from stoichiometric BaCuSeF targets on Si (001) and amorphous SiO_2 substrates. BaCuSeF films were polycrystalline, single phase, *p*-type, and on average 75 % transparent over the wavelength range 400 - 2500 nm. The transparency is partly limited by the reflective losses (~ 15%) at the front surface. Bulk and surface compositions of the thin films were determined by electron probe microanalysis (EPMA) and XPS, respectively. BaCuSeF thin films were capped with 1000 nm of amorphous Se for

protection[13] during transportation from Corvallis, OR to Darmstadt, Germany. This protection was necessary, since uncapped BaCuChF surfaces were oxidized and contaminated,[14] which could have been a contributing reason for the poor performance of BaCuTeF in PV devices reported before.[15] For the *in-situ* interfacing experiments, 280-nm thick ZnTe layers were sequentially deposited on the BaCuSeF film at room temperature in a stepwise manner, and XPS/UPS were recorded after each step using the DAISY-SOL.[16] Details of these and similar experiments appear elsewhere.[14]

5.3 Results and discussion

The XPS and UPS spectra of the BaCuSeF/ZnTe interface are shown in Fig. 5.1. For a thick ZnTe layer (> 25 Å), BaCuSeF and ZnTe XPS peaks shift to higher binding energies (BE) with increasing ZnTe thickness, indicating downward VB bending of BaCuSeF caused by electron transfer to this material. The BE of the secondary electron edge (SEE) changes for low ZnTe thickness (< 25 Å), indicating the change of the work function (WF) due to change in an interface dipole. In this thickness range, the Te $3d_{3/2}$ and the Zn $2p_{3/2}$ XPS peaks do not shift in parallel. We attribute a strong shift of the Te $3d_{3/2}$ line at low coverage to the transfer of electrons from Te atoms. The Zn $2p_{3/2}$ peak does not show this charge-transfer shift, because Zn atoms do not contribute to the VB of ZnTe. Similar effect has been observed at the BaCuSeF/ZnPc interface.[14]

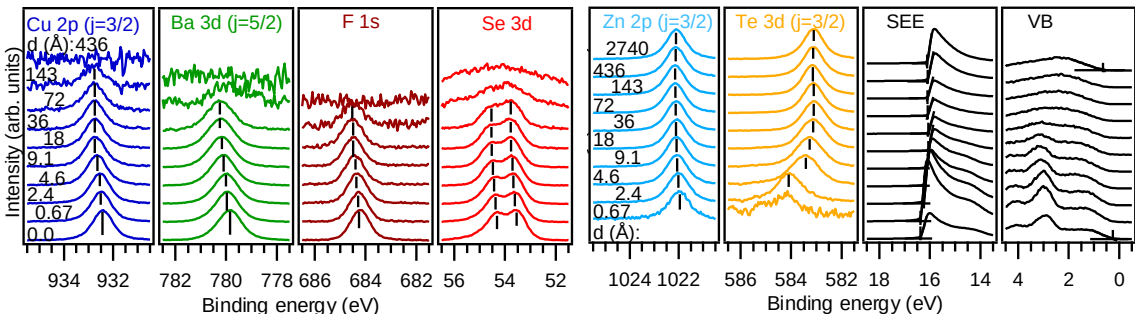

FIG. 5.1. Normalized photoemission spectra of the BaCuSeF/ZnTe interface. ZnTe thicknesses *d* are the same for all panels in a row. The vertical lines indicate binding energies used to plot Fig. 5.2.

There is interdiffusion at the BaCuSeF/ZnTe interface. In Fig. 5.1, the Cu $2p_{3/2}$ XPS peak is present at 143-Å ZnTe coverage, whereas the Ba $3d_{5/2}$ and F 1*s* peaks that have lower BE are absent. The bulk of ZnTe films is Te-poor by 4 at%, but the surfaces are Te-rich by 20 at%, so it is likely that Cu atoms diffuse into ZnTe and forms Cu-Zn-Te or Cu-Te phases. The interdiffusion layer has been confirmed using high-resolution STEM/EDX measurements that will be published elsewhere. Similar effect was also observed at the CdTe interfaces with Cu-containing back contacts.[4,5]

BaCuSeF and ZnTe VB BE and the WF as a function of ZnTe thickness are shown in Fig. 5.2. Decapped BaCuSeF surface has a VB BE of 0.32±0.10 eV, larger than for the thin film bulk deduced from measured carrier concentration and calculated density of states (0.04 eV). The WF is 4.85±0.05 eV, larger than for the pressed pellets measured by UPS (3.6 eV).[17] A thick ZnTe layer (280 nm) has a VB BE of 0.59±0.10 eV and a WF of 5.11±0.05 eV.

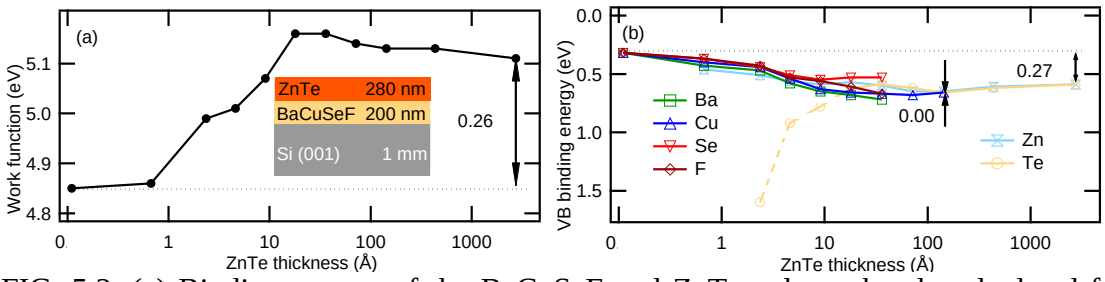

FIG. 5.2. (a) Binding energy of the BaCuSeF and ZnTe valence bands calculated from XPS core-level spectra. The dashed line represents the shift of Te $3d_{3/2}$ states due to charge transfer from Te atoms. (b) Work function of the BaCuSeF/ZnTe interface. The final configuration of the sample is schematically depicted in the inset.

Measured VB BEs and the WFs (Fig. 5.2) were used to establish band alignment of BaCuSeF and ZnTe before contact (Fig. 5.3a). After contact, BaCuSeF and ZnTe have the same VB BE (Fig. 5.2a), so the VB offset is 0.00±0.10 eV (Fig. 5.3b). The CB offset is 0.94±0.10 eV, as calculated from the BaCuSeF[12] and ZnTe[18] band gaps (Fig. 5.3c). The band bending of 0.27 eV (Fig. 5.2a) and the change of the WF of 0.26 eV (Fig. 5.2b) sum to a vacuum level shift of 0.53±0.10 eV (Fig. 5.3b). The higher vacuum level in ZnTe would correspond to an interface dipole with the negative end towards ZnTe. This direction is contraindicated by the direction of the BaCuSeF band bending and by the

high binding energy of the Te $3d_{3/2}$ line at low coverage (Fig. 5.2a), which both point to an opposite direction of the charge transfer. Possible reasons for the opposite direction of the charge transfer are the graded character of the interface or a large surface dipole contribution to the work function of decapped BaCuSeF, which is modified during interface formation. The latter is likely, as the measured ionization potential (E_{VAC}-E_{VB}) of BaCuSeF (5.2±0.15 eV) is much smaller, e.g., than that of $CuInSe_2$ (6.1 eV),[19] which has a similar VB structure.

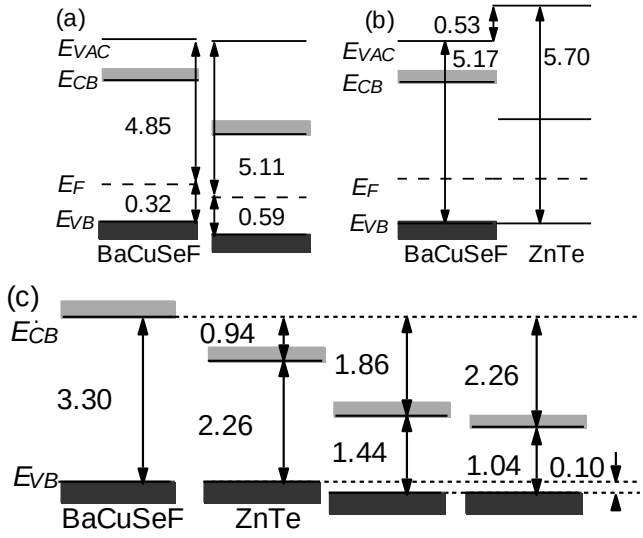

FIG. 5.3. Alignment of the energy levels of BaCuSeF and ZnTe (a) before and (b) after contact as measured by PES. (c) Band offsets of BaCuSeF with CdTe and $CuInSe_2$ calculated from the literature values of the band offsets of these materials with ZnTe. All energies are in eV.

The band alignment of BaCuSeF with the chalcogenide PV materials is shown in Fig. 5.3c. It was calculated from the ZnTe/CdTe and CdTe/$CuInSe_2$ band offsets using the transitivity rule.[20,21]BaCuSeF/CdTe and BaCuSeF/$CuInSe_2$ interfaces have VB offsets of 0.10±0.10 eV, and CB offsets of 1.86±0.10 eV and 2.26±0.10 eV, respectively. The small VB offsets are expected, because the Se 4*p* - Cu 3*d* repulsion in BaCuSeF is stronger than the Te 5*p* - Cd 4*d* repulsion in CdTe, and the VB character of BaCuSeF is similar to that of $CuInSe_2$.[17] The VB character of Cu_2ZnSnS_4 is more similar to BaCuSF than BaCuSeF, so the two sulfides constitute a good match for CZTS solar cells.[22]

BaCuChF interfaces with ZnTe, CdTe, $CuInSe_2$, and Cu_2ZnSnS_4 are likely to have similar interdiffusion because of the similar chemical compositions of II-VI, (I-III)-VI_2 and (I_2-[II-IV])-VI_4 semiconductors.

Overall, BaCuChF materials with appropriate surface protection or fully *in-situ* processing should make good *p*-type contacts in chalcogenide *p-i-n* solar cells. In addition, BaCuSeF has the potential to replace the Cu or $Cu_{2-x}Te$ back contact in CdTe PV devices, due to its better band alignment with CdTe. Finally, BaCuChF are transparent enough to be used in tandem chalcogenide solar cells. Related LaCuOCh materials[23,24] are also promising for these applications, since the VB characters of BaCuChF and LaCuOCh are similar.[17]

5.4 Summary

In summary, we have measured the VB offset between BaCuSeF and ZnTe by XPS/UPS. There is no measurable VB discontinuity and the interface is graded, which makes BaCuSeF an ideal *p*-type contact to ZnTe. A small VB offset and a similar chemistry of ZnTe, CdTe, and $CuInSe_2$ suggest that BaCuSeF is likely to make a good *p*-layer for the chalcogenide *p-i-n* solar cells.

References

[1] W Jaegermann, A Klein, and T Mayer, Advanced Materials **21**, 4196 (2009).

[2] B. Spath, J. Fritsche, A. Klein, and W. Jaegermann, Appl. Phys. Lett. **90**, 062112 (2007).

[3] A. Barati, A. Klein, and W. Jaegermann, Thin Solid Films **517**, 2149 (2009).

[4] B. Späth, K. Lakus-Wollny, J. Fritsche, C.S. Ferekides, A. Klein, and W. Jaegermann, Thin Solid Films **515**, 6172 (2007).

[5] G. Teeter, J. Appl. Phys. **102**, 034504 (2007).

[6] J. Tate, P. F. Newhouse, R. Kykyneshi, P. A. Hersh, J. Kinney, D. H. McIntyre, and D. A. Keszler, Thin Solid Films **516**, 5795 (2008).

[7] H. Yanagi, J. Tate, S. Park, C.-H. Park, and D. A. Keszler, Applied Physics Letters **82**, 2814 (2003).

[8] C.-H. Park, R. Kykyneshi, A. Yokochi, J. Tate, and D. A. Keszler, Journal of Solid State Chemistry **180**, 1672 (2007).

[9] R. Kykyneshi, D. H. McIntyre, J. Tate, C.-H. Park, and D. A. Keszler, Solid State Sciences **10**, 921 (2008).

[10] C.-H. Park, D. A. Keszler, H. Yanagi, and J. Tate, Thin Solid Films **445**, 288 (2003).

[11] A. Zakutayev, D. H. McIntyre, G. Schneider, D. A. Keszler, C.-H. Park, and J. Tate, provisionally accepted to Thin Solid Films.

[12] A. Zakutayev, R. Kykyneshi, G. Schneider, D. H. McIntyre and J. Tate, Phys. Rev. B **81** (in press)

[13] T. Schulmeyer, R. Hunger, A. Klein, W. Jaegermann, and S. Niki, Appl. Phys. Lett. 84, 3067 (2004).

[14] A. Zakutayev, J. Tate, H. A. S. Platt, D. Keszler, C. Hein, T. Meyer, A. Klein, J. Appl. Phys 107 (in press, manuscript number 007008JAP).

[15] J. A. Spies, R. Schafer, J. F. Wager, P. Hersh, H. A. S. Platt, D. A. Keszler, G. Schneider, R. Kykyneshi, J. Tate, X. Liu, A. D. Compaan, and W. N. Shafarman, Solar Energy Materials and Solar Cells **93**, 1296 (2009).

[16] J. Fritsche, A. Klein, and W. Jaegermann, Adv. Eng. Mater. **7,** 914 (2005).

[17] H. Yanagi, J. Tate, S. Park, C. -H. Park, D. A. Keszler, M. Hirano, and H. Hosono, J. Appl. Phys. **100**, 083705 (2006).

[18] S. J Fonash, *Solar Cell Device Physics* (Academic Press, 1981).

[19] T. Schulmeyer, Ph.D. Thesis, Technische Universität Darmstadt, 2005

[20] T. Schulmeyer, R. Hunger, M. Lebedev, W. Jaegermann, A. Klein, R. Kniese, M. Powalla, Thin Solid Films **480-481**, 110 (2005).

[21] K. Ellmer, A. Klein, and B. Rech, *Transparent Conductive Zinc Oxide* (Springer, 2008).

[22] J. Paier, R. Asahi, A. Nagoya, and G. Kresse, Phys. Rev. B **79**, 115126 (2009).

[23] K. Ueda, S. Inoue, S. Hirose, H. Kawazoe, and H. Hosono, Appl. Phys. Lett. **77**, 2701 (2000).

[24] H. Hiramatsu, K. Ueda, H. Ohta, M. Hirano, T. Kamiya, and H. Hosono, Appl. Phys. Lett. **82**, 1048 (2003).

CHAPTER 6

Defect physics of BaCuChF (Ch = S, Se, Te) wide-bandgap *p*-type semiconductors

A. Zakutayev, J. Tate and G. Schneider

In preparation for submission

6.1 Introduction

BaCuChF (Ch = S, Se, Te) is a family of wide-bandgap *p*-type semiconductors[1] suitable for *p*-contact applications in thin film chalcogenide solar cells[2] and organic light-emitting devices.[3] BaCuChF materials[4],[5] are isostructural with other *p*-type transparent conductors LnCuOCh (Ln = La, Pr, Nd)[6] and high-temperature superconductors LaFeOPn (Pn = P, As, Sb)[7] (Fig. 6.1). In 40-nm LaCuOSe thin films *p*-type conductivity is attributed to copper vacancies due to depth distribution of copper content observed by secondary ion mass spectroscopy.[8] However, there are no systematic studies on the origin of *p*-type conductivity in either BaCuChF or LaCuOCh.

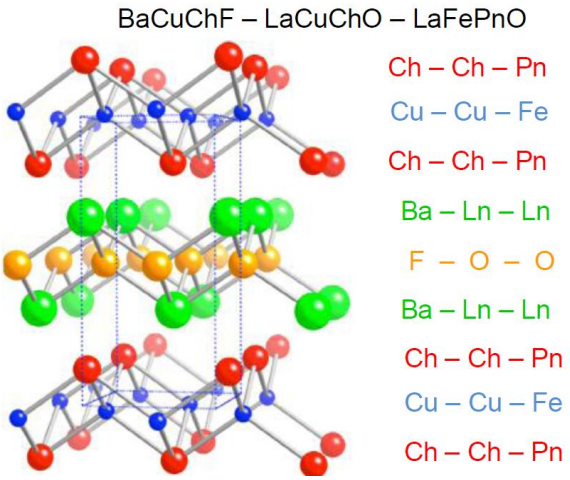

FIG. 6.1 Crystal structure of BaCuChF (Ch = S, Se, Te), LnCuOCh (Ln = La, Pr, Nd) and LaFeOPn (Pn = P, As, Sb).

Density functional theory (DFT) provides a theoretical way to examine the defect chemistry of the materials. It was used to explain the properties of intrinsic defects and extrinsic impurities in binary (CdTe,[9] In_2O_3,[10] ZnO[11,12]) and ternary ($CuInSe_2$,[13,14] $CuAlO_2$,[15,16] $CuSr_2O_2$[17]) compounds. Defect physics of quaternary semiconductors (such as Cu_2ZnSnS_4) is complex, since the cations can substitute for each other, and was reported only recently.[18,19] Mixed-anion quaternary semiconductors, such as BaCuChF and LaCuOCh have even larger variety of likely defects, because of possible disorder on both cation and anion sub-lattices.

We report a systematic study of the native point defects, defect complexes and oxygen impurities in BaCuChF (Ch = S, Se, Te). The aim of this work is to elucidate the origin of *p*-type conductivity in BaCuChF and explain a number of experimental observations. Using density functional theory, we found that copper vacancies in BaCuChF generate free holes and that increase of the carrier concenrtaion in the S-Se-Te series is due to reduced compensation of these acceptors by donor-like chalcogen vacancies. Transition levels of chalcogen vacancies are in agreement with experimental results, and can be used to explain sub-gap photoluminescence, optical absorption and persistent photoconductivity. Oxygen-related defects do not affect bulk properties, but surface oxidation affects the charge transport. Calculated equilibrium Fermi levels in BaCuChF are bound to a narrow pinning range close to the valence band maximum. Therefore, BaCuChF materials suitable for *p*-type transparent contact application, but it is difficult to fabricate field-effect transistors with BaCuChF channels.

The paper starts with theoretical and experimental details (Section II). Discussion of the results (Section III) is arranged as follows. First we consider phase stability of BaCuChF (A). Next, we discuss the physics of native point defects (B) and their optoelectronic properties (C). Finally, we address the oxygen-related defects (D) and various defect complexes (E). The paper ends with summary and conclusions (Section IV).

6.2 Methods

6.2.1. Theory

In this work we used the A_B^q defect notation, where A is an actually occupant of the site (V for a vacancy), B is a nominal occupant of the site (I for an interstitial site), and q is the charged trapped by the defect. For example, V_{Cu}^{-1} represents a singly-charged copper vacancy, Ba_I^{2+} represents a doubly-charged barium interstitial, and O_S^0 represents a neutral substitutional defect of oxygen on the sulfur site. Defect transition levels are denoted using $A_B^{q/q'}$ notation, where q and q' are initial and final charge states of the defect.

Formation enthalpy $\Delta H_{D,q}$ of a defect D in a charge state q depends on (i) the difference in the total free energies of the host material with and without the defect $E_{D,q}$-E_H calculated using DFT, (ii) the number n_a of atoms a removed from the host to create the defect and their chemical potential in the host $\Delta\mu_a$ with respect to that in the elemental substance ${\mu_a}^O$, and (iii) the Fermi level of the electrons E_F with respect to the energy of the valence band E_V:

$$\Delta H_{D,q}(E_F) = (E_{D,q} - E_H) + \sum_a n_a({\mu_a}^O + \Delta\mu_a) + q(E_V + E_F) \quad (1)$$

The value of the parameter ${\mu_a}^O$ and range of the variable $\Delta\mu_a$ was obtained considering formation enthalpies of possible impurities in BaCuChF as will be discussed below. We used self-consistent thermodynamic simulations[20] to obtain room-temperature equilibrium Fermi levels and corresponding concentration of defects and free charge carriers. Defect transition levels were obtained from the DFT defect calculation with fully-relaxed atomic positions. The energy cost to form a defect complex was calculated as a difference between the sum of formation enthalpies of the isolated defects and a formation enthalpy of a defect complex.[13]

To find defect formation enthalpies, we performed density functional theory (DFT) calculations using Perdew-Burke-Ernzerhof (PBE) general gradient approximation (GGA) and the projected augmented wave (PAW) method.[21] 400 eV energy cut-off was used. Charge density was calculated using the tetrahedron method over a Γ-centered 4x4x4 k-point mesh (k = 36 special points). 2x2x1 supercells with n = 32 atoms were used for all the calculations. Equilibrium GGA BaCuChF crystal lattice parameters (a= 4.149, c/a= 2.200 for BaCuSF, a= 4.271, c/a= 2.169 for BaCuSF, and a= 4.464, c/a= 2.128 for BaCuSF)[22] were fixed, and all the atoms were allowed to relax without any symmetry constraints during the calculation.

Results obtained using the supercell defect calculations were corrected due to (i) potential misalignment in reference and defect calculations, (ii) DFT band gap error, and (iii) defect band formation and filling caused by the finite supercell sizes (for the main defects only). [20] Potentials of the supercells with- and without the defects were aligned using Ba 5s states close to -30 eV as a reference. Conduction band minimum (CBM) and

not fully charged donor-like states were shifted up, so that the GGA gap matched the GW and experimental gaps (3.6 eV for BaCuSF, 3.3 eV for BaCuSeF, and 2.2 eV for BaCuTeF).[23] Valence band maximum (VBM) was not corrected, since no suitable shift was found to align all the calculated DOS peaks with experimental XPS spectra.[3] The image charge correction[24] was intentionally omitted (i) since its algorithm is not unique, and (ii) since interaction of charged defect occurs in highly doped semiconductors, like BaCuChF.[22]

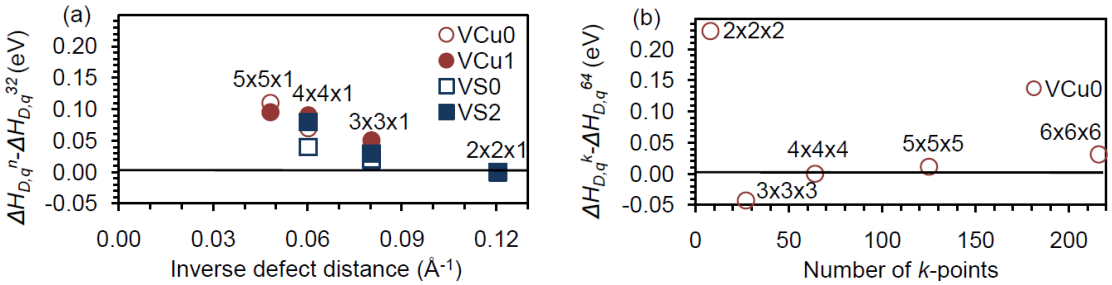

FIG. 6.2 (a) Formation enthalpy of V_{Cu} and V_{Ch} as a function of inverse distance between the defects relative to the n = 32 calculation. (b) Formation enthalpy of $V_{Cu}{}^{0}$ as a function of number of k-points relative to the k=64 calculation. The labels in (a) and (b) represent sizes of the supercells and divisions of the k-point meshes, respectively.

We checked the convergence of the defect calculation results using larger $n = m$ x m x 1 (m = 3, 4, 5) BaCuSF supercells and using finer $k = m$ x m x m (m = 5, 6) k-point meshes, keeping nk >1152. The difference in the formation enthalpies ($\Delta H_{D,q}{}^{n}$ - $\Delta H_{D,q}{}^{32}$) is shown in Fig. 6.2a as a function of inverse distance between the defects for the copper and sulfur vacancies. The deviation of the 2x2x1 supercell result from the extrapolated infinite supercell result is +0.20 eV. The difference ($\Delta H_{D,q}{}^{k}$ - $\Delta H_{D,q}{}^{64}$) is shown in Fig. 6.2b as a function of k for a neutral cooper vacancy. The deviation of the result obtained using a 4x4x4 k-point mesh is 0.05 eV smaller compared to the result from the 6x6x6 k-point mesh. Therefore, we estimate the total DFT energy uncertainty of the 2x2x1 supercell calculation with the 4x4x4 k-point mesh to be +0.25 eV.

6.2.2. Experiments

Photoluminescence (PL) experiments were performed in a temperature range of 80 – 300 ^{o}K on single-phase BaCuChF powders prepared by solid-state reactions,[4,5] and *c*-axis oriented BaCuChF thin films prepared by pulsed laser deposition (PLD) on MgO (001) substrates.[22,25] PL was excited using a N_2 laser (337 nm, 120 μJ, 20 Hz, 4 ns pulses) and measured using a spectrometer equipped with a CCD detector. The resulting PL spectra were fit using the sum of the Gaussian functions (more common in literature than Lorentzians) over a constant background. Optical absorption measurements were performed at room temperature on specially prepared S-poor BaCuSF thin films using a custom grating spectrometer.[22] To eliminate the effect of light interference on absorption spectra both transmittance and reflectance were included in the calculation.[26] Seebeck coefficient was measured at 3-5 ^{o}C temperature gradient using a custom-built setup. Concentration of free holes was determined from resistivity and Hall effect measurements on patterned BaCuChF thin films.[22] This concentration was used to calculate experimental bulk Fermi levels E_F^{Hall} using the DFT density of states and a Fermi-Dirac distribution.[23] Experimental surface Fermi levels E_F^{XPS} were measured using x-ray photoemission spectroscopy (XPS) on polished sintered BaCuChF pressed pellets exposed to monochromized Al *K*α radiation.[3]

6.3 Results and discussion

6.3.1. Phase stability

BaCuChF stability regions are limited by formation of elemental, binary and ternary impurities. Materials formation energies per formula unit ΔH_F^M used to calculate the stability region are summarized in Table 6.1. For BaO, BaCh and Cu_2O, theoretical ΔH_F^M calculated using DFT are in good agreement with experimental ΔH_F^M available in literature,[27] but the DFT results are somewhat smaller for BaF_2 and CuF. For Cu_2Ch, experimental ΔH_F^M obtained from the literature was used for the calculation of the stability region. For elemental, ternary and quaternary chalcogenides, experimental ΔH_F^M are not available in literature. For these materials, ΔH_F^M calculated using DFT decrease in the S-Se-Te series, which is consistent with experimental expectations.

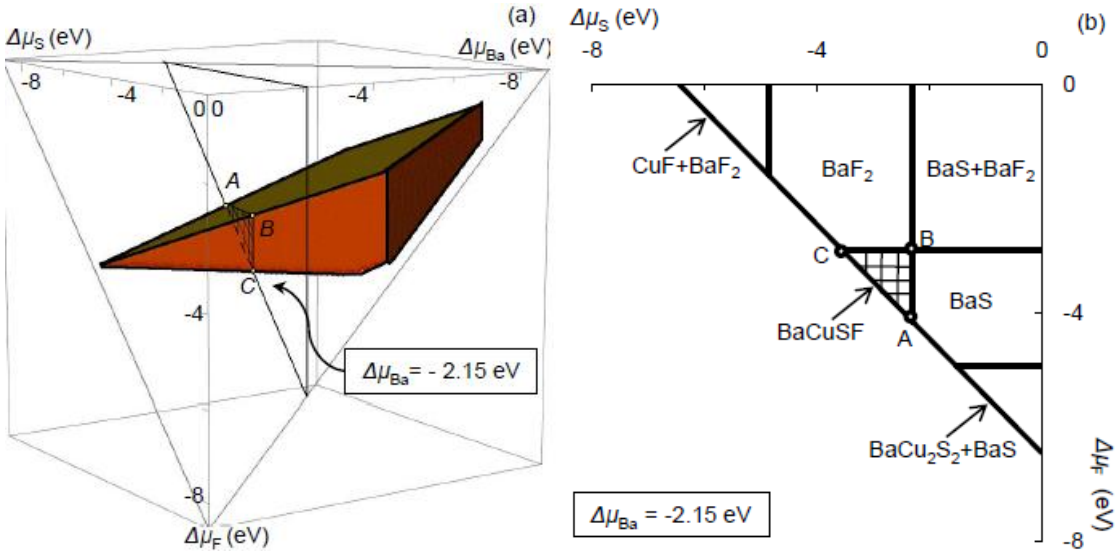

FIG. 6.3 (a) BaCuSF stability polyhedron (b) Crossection of the stability polyhedron by $\Delta\mu_{Ba}$ =0.25$\Delta H^{\mathrm{BaCuSF}}$ plane.

Stability regions for all three BaCuChF are qualitatively similar, so only BaCuSF will be discussed. Stability region of BaCuSF is limited to a 3D polyhedron by formation of Cu, BaS, BaF_2, CuF, $Cu_2S$and $BaCu_2S_2$ impurities (Fig. 6.3a). The polyhedron is located close to the (111) plane, which indicates that Cu-rich conditions are favorable for formation of phase-pure BaCuChF. Within the polyhedron, chemical potential of Ba can vary from -7.0 to 0.0 eV. We consider the crossection of the polyhedron by $\Delta\mu_{Ba}$ =0.25ΔH_F^{BaCuSF} = -2.15 eV plane, because Ba is the heaviest atom and its absolute content is the least likely to vary under any experimental conditions. Within the $\Delta\mu_{Ba}$ =0.25ΔH_F^{BaCuSF} plane, stability range of BaCuSF is limited by formation of Cu, BaS and BaF_2 impurities (Fig. 6.3b). This is consistent with experimental results, because BaS[3] and BaF_2[5] are the only impurities occasionally observed using XRD.

BaCuSF stability region within the $\Delta\mu_{Ba}$ =0.25ΔH_F^{BaCuSF} plane has three special points: (i) point "*A*" - Cu- rich/Ch-rich/F-poor condition, where BaCuSF is in equilibrium with Cu and BaS; (ii) point "*B*" – Cu-poor/Ch-rich/F-rich conditions, where BaCuSF is in equilibrium with BaF_2 and BaS; (iii) point "*C*" – Cu-rich/Ch-poor/F-rich conditions, where BaCuChF is in equilibrium Cu and BaF_2. We chose to calculate the defect formation enthalpies at the point "*A*", because Ch-rich conditions, such as flowing H_2Ch gas,[3] or addition of extra Ch[3,5] are typically used for the BaCuChF synthesis

experiments. For this reason we did not consider Ch-poor point "*C*". We did not consider Ch-rich/Cu-poor point "*B*" where formation enthalpy of copper vacancy is strongly negative and its concentration is larger than the concentration of available sites, which is physically unreasonable. Oxygen-related defects were calculated at the maximal O-rich conditions, assuming that BaCuChF is in equilibrium with BaO impurity phase. The values of $\Delta\mu_{Ba}$, $\Delta\mu_{Cu}$, $\Delta\mu_{Ch}$, $\Delta\mu_{F}$ and $\Delta\mu_{O}$ used for the calculation are summarized in Table 6.2.

TABLE 6.1 Calculated materials formation energies per formula unit ΔH_F^M

$-\Delta H_F^M$, eV	S	Se	Te
BaCuChF	8.60	8.28	7.98
$BaCu_2Ch_2$	5.20	4.54	3.95
BaCh	4.45	4.17	3.75
Cu_2Ch	0.82	0.55	0.44
Ch	3.91	3.51	3.05
Fluorides:	BaF_2:7.97;CuF:1.59		
Metals:	Ba:1.92;Cu:3.73		
Gasses:	F_2:3.6;O_2:8.4		
Oxides:	BaO:5.75;Cu_2O:1.32		

TABLE 6.2 Chemical potential difference $\Delta\mu_a$ used for the defect calculations

$-\Delta\mu_a^M$, eV	S	Se	Te
Ba	2.15	2.07	2.00
Cu	0.00	0.00	0.00
Ch	2.34	2.10	1.74
F	4.11	4.11	4.25
O	3.60	3.68	3.76

6.3.2. Native point defects

Calculated formation enthalpies of acceptor-like ($q \leq 0$) and donor-like ($q \geq 0$) defect in BaCuChF at E_F=0 (Eq. 2.1) are given in Table 6.3. The lowest energy defects for all three BaCuChF compounds are acceptor-like V_{Cu}^{-1} and donor-like V_{Ch}^{+2}. Therefore, V_{Cu}^{-1} is the most likely source of unintentional *p*-type conductivity in BaCuChF. Large formation enthalpies of all the other point defects can be understood

from Eq. 2.1. The formation enthalpies of the defects depend on (i) the energy needed to distort the bonds (1st term), (ii) chemical potential of the involved elements (2nd term) and (iii) type and charge of the defect (donor/acceptor) and the Fermi energy (3rd term). Defects have large formation enthalpies if at least one of these terms is large. The 1st term is large if large atoms are added/removed (V_{Ba}, Ba_I) or if the ionic radii mismatch is large (Ba_{Cu}, Cu_{Ba}, F_{Ch}, Ch_F). The 2nd term is large if reactive elements (small $|\mu_a^O|$, Table 6.1) are removed from the cell (V_F, V_{Ba}, Ch_F, Cu_{Ba}, O_F), if benign elements (large $|\mu_a^O|$, Table 6.1) are added to the cell (Cu_{Ba}, S_F, Cu_I, S_I, O_{Ch}, O_I), or if the synthesis conditions (Table 6.2) are not favorable (F_I). All the defects but V_{Cu} and V_{Ch} satisfy at least one of these conditions.

TABLE 6.3 Formation enthalpies of acceptor-like (*a*-) and donor-like (*d*-) vacancies, interstitials, substitutional defects, and the energy costs to form defect complexes in BaCuChF at E_F=0.

Material	BaCuSF			BaCuSeF			BaCuTeF		
$\|q\|$	0	1	2	0	1	2	0	1	2
a-V_{Cu}	0.34	0.22		0.27	0.13		0.18	-0.02	
a-V_{Ba}	3.04	2.61	2.61	2.89	2.43	2.03	2.43	1.95	1.87
d-V_F	4.61	0.63		4.09	0.88		3.46	0.53	
d-V_{Ch}	5.58	3.16	-0.01	4.20	2.69	0.09	3.35	2.49	0.20
a-Cu_{Ba}	4.42	3.88		4.52	3.78		4.33	4.27	
a-Ch_F	3.78	3.43		4.16	4.36		4.65	4.16	
d-F_{Ch}	4.23	0.74		3.77	1.00		3.54	1.60	
d-Ba_{Cu}	6.10	2.03		5.27	2.15		4.78	2.37	
a-F_I	1.66	1.52		1.59	1.54		1.52	1.46	
a-Ch_I	3.26	5.50	7.62	11.6	12.9	14.1	10.8	10.2	10.6
d-Ba_I	11.9	5.75	0.83	8.62	5.31	3.42	11.3	7.92	4.94
d-Cu_I	6.29	1.75		2.07	5.50		2.18	4.51	
a-O_F	1.48	1.16		1.39	1.14		1.03	0.80	
d-O_{Ch}	3.93	1.81		3.05	1.32		2.96	2.14	
a-O_{Ch}	3.93	2.58		3.05	2.38		2.96	2.02	
a-O_I	1.97	3.10	3.59	2.19	2.82	3.29	1.95	2.44	2.92
V_{Ch}+2V_{Cu}	-1.33			-1.21			-0.91		
V_{Ch}+F_I		-2.15			-1.98			-1.72	
V_{Ch}+V_{Cu}+F_I	-2.75			-2.57			-1.30		

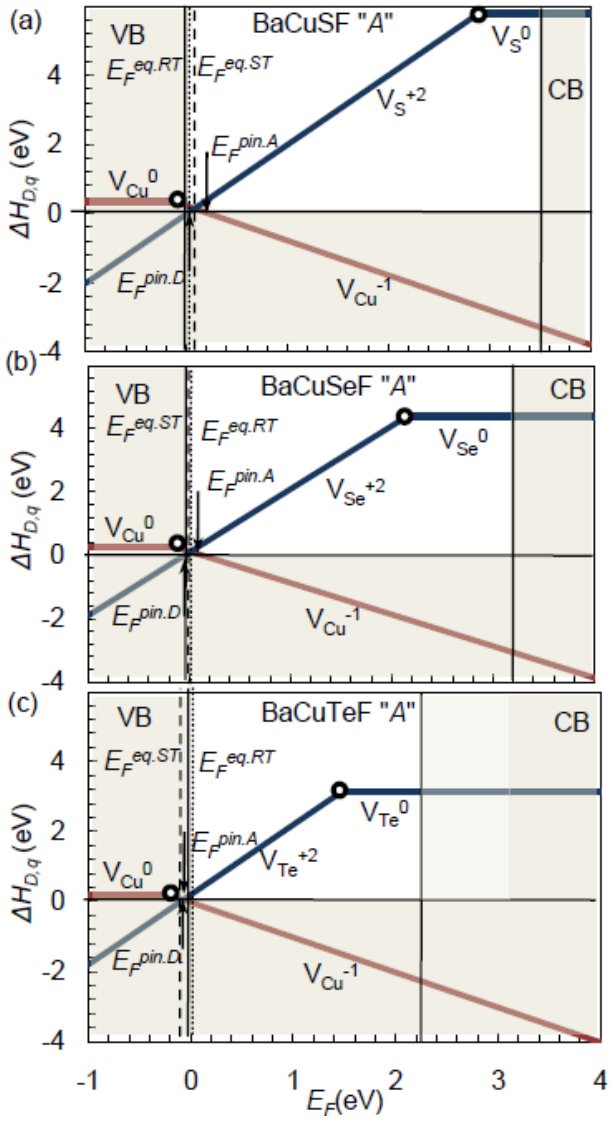

FIG. 6.4 Formation enthalpies of the lowest charge state of V_{Cu} and V_{Ch} as a function of Fermi energy for (a) BaCuSF, (b) BaCuSeF and (c) BaCuTeF. The empty circles at the kinks of the lines correspond to defect transition levels between different charge states. The equilibrium Fermi energies at 700 ^{o}C and 30 ^{o}C are indicated by dashed and dotted lines, respectively. The Fermi pinning levels are indicated by arrows.

In Fig. 6.4, the formation enthalpies for the lowest-energy charge states of V_{Cu} and V_{Ch} are shown as a function of the Fermi energy E_F. In the S-Se-Te series, formation enthalpy decreases for V_{Cu}^{-1} and increases for V_{Ch}^{+2}. One reason for this trend is increase on the absolute scale of E_V in Eq. 2.1. The increase of E_V in S-Se-Te series in BaCuChF should be similar to that in chalcopyrites due to similar degree of Ch *p* - Cu *d* repulsion in

the VB,[28] but weaker than that in II-VI binary chalcogenides[29]. The other reason for decreasing formation enthalpy of V_{Ch}^{+2} is decrease of the bandgap in the S-Se-Te series. Since BaCuSF band gap is larger, V_S^{+2} line intercepts the $E_F = 0$ axis lower than the V_{Se}^{+2} and V_{Te}^{+2} lines in BaCuSeF and BaCuTeF, respectively. This example illustrates how compensating defects are more likely to form in wide-bandgap semiconductors, which is a contributing reason for difficulty of doping transparent conductive oxides (TCOs).[30] High doping levels are easier to achieve in transparent conductors (TCs) with narrow forbidden electronic band gaps and wider optical band gaps, such as BaCuTeF,[23] $CuInO_2$[31] and In_2O_3[32]. In these materials, the defect chemistry and resulting transport properties are controlled by a narrow electronic gap, while the transparency is defined by the wider optical gap.[31]

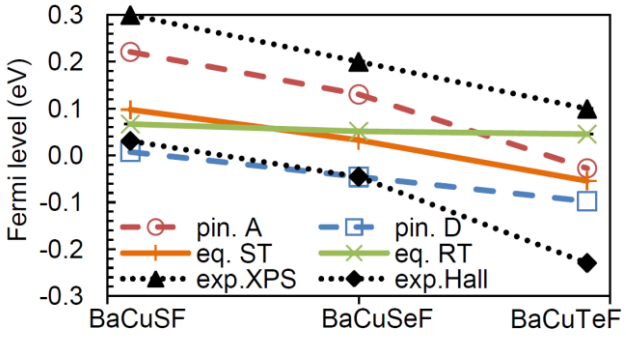

FIG. 6.5 Equilibrium Fermi levels at synthesis (700 ^{o}C) and room (30 ^{o}C) temperatures, donor and acceptor pinning Fermi levels, and experimental Fermi levels measured by XPS and calculated from Hall effect measurement results. The lines are guides to the eye.

Calculated theoretical equilibrium Fermi levels are shown as vertical lines in Fig. 6.4. At 700 ^{o}C synthesis temperature[3] equilibrium Fermi levels ($E_F^{eq.ST}$) in all three BaCuChF compounds fall close to the intercept of the V_{Cu}^{-1} and V_S^{+2} lines (Fig. 6.4). If E_F increases above $E_F^{eq.ST}$ formation enthalpy $\Delta H_{D,q}$ and concentration of V_{Cu}^{-1} decreases (Eq. 6.1), additional free holes appear to maintain charge balance, and E_F returns back to the intercept point $E_F^{eq.ST}$ at which the charges of V_{Cu}^{-1} and V_{Ch}^{+2} compensate each other. If E_F decreases below $E_F^{eq.ST}$, free holes disappear to compensate formation of new V_{Ch}^{+2}, and E_F returns back to the intercept point $E_F^{eq.ST}$. This mechanism of maintaining the charge balance indicates that BaCuChF are compensated semiconductors. Defect

compensation is also observed in other multicomponent semiconductors, such as ($2V_{Cu}^{-1}$+In_{Cu}^{+2}) in $CuGaSe_2$,[13] and (Cu_{Zn}^{1-}+Zn_{Cu}^{1+}) in Cu_2ZnSnS_4.[18]

Experimental Fermi levels in bulk and on the surface of BaCuChF are close to the valence band maximum and decrease in the S-Se-Te series.[3] Experimental and theoretical equilibrium Fermi levels are summarized in Fig. 6.5. Theoretical equilibrium Fermi levels are in qualitative agreement with the experimental results. One possible reason for the quantitative difference between the theoretical and the experimental Fermi levels is that we chose too Cu-rich chemical potential. Our choice predicts formation of Cu impurity (Fig. 6.3b), but it was never observed it in any experiments. The second possible reason is that the calculations did not include charged defect complexes with low formation enthalpies (Table 6.2). The third possible reason for the difference between the theoretical predictions and the experimental results is the residual +0.25 eV error in the calculated defect formation enthalpies. The fourth reason is that bulk Fermi levels were measured for BaCuChF thin films prepared by pulsed laser deposition (PLD) and surface Fermi levels were measured on the oxidized grain boundaries, but both of these conditions are far from the equilibrium assumed in the thermodynamic simulations.

Numerous experimental attempts to fabricate transparent field-effect transistors (TTFTs) with BaCuChF *p*-type channel had limited success.[33] Experimental difficulty in achieving high on/off ratios can be explained by the narrow Fermi level pinning range in BaCuChF. Pinning Fermi levels in BaCuChF are shown as arrows in Fig. 6.4. The downward arrow in Fig. 6.4 corresponds to V_{Cu}^{-1} acceptor pinning Fermi level ($E_F^{pin.A}$), and the upward arrow in Fig. 6.4 corresponds to V_{Ch}^{+2} donor pinning Fermi level ($E_F^{pin.D}$). Pinning Fermi levels are summarized in Fig. 6.5. The pinning range $E_F^{pin.A}$ - $E_F^{pin.D}$ inBaCuSF is narrow (0.2 eV) and it further decreases in the S-Se-Te series. In an applied electric field, when E_F increases to $E_F^{pin.A}$, formation enthalpy $\Delta H_{D,q}$ of V_{Cu}^{-1} becomes negative, so V_{Cu}^{-1} will spontaneously appear, keeping E_F pinned below $E_F^{pin.A}$. When E_F decreases to $E_F^{pin.D}$, V_{Ch}^{+2} will spontaneously appear, keeping E_F pinned above $E_F^{pin.D}$. Therefore, it is impossible to appreciably modulate E_F in BaCuChF by the electric field which explains our difficulty in fabrication of BaCuChF-based TTFTs with high on/off ratios.

We attempted to utilize the non-equilibrium character of the thin film growth to control the Fermi level and the concentration of free holes in BaCuChF thin films. To decrease $p^{exp.}$, we prepared 400-nm $BaCu_{1+x}ChF$ thin films using alternating pulsed laser deposition (PLD) technique.[22] Each $BaCu_{1+x}ChF$ sample consisted of 10 periods of alternating BaCuChF and Cu layers. The layers interdiffused during the growth at 400 ^{o}C. As the amount of excess Cu in $BaCu_{1+x}SF$ increased to x=0.05, both resistivity ρ and Seebeck coefficient S increased by about a factor of 5, but for larger x, ρ and S started to decrease. The decrease in ρ and S for large x was attributed to formation of Cu-related impurity bands, manifested by moderate sub-gap optical absorption. Formation of similar impurity bands was also observed for the $BaCu_{1+x}SeF$ and $BaCu_{1+x}TeF$ thin films with large x, but no Cu XRD diffractions peaks were observed in any $BaCu_{1+x}ChF$ samples. We conclude that it is difficult to control the concentration of free holes in BaCuChF using both equilibrium and non-equilibrium synthesis approaches.

6.3.3. Optoelectronic properties

Results of the temperature-dependent photoluminescence (PL) measurements are shown in Fig. 6.6 (a-c). The inset in Fig. 6.6c depicts the PL experimental setup. PL bands E_A, E_B, E_C , and E_D are present in the spectra of BaCuSF and BaCuSeF thin film (Fig. 6.6a and 6.6b). Relative intensity of these bands changes with temperature. In addition, persistent photoconductivity (PPC) with characteristic decay times on the order of minutes is observed for BaCuSF (Fig. 6.6b, inset) and BaCuSeF thin films samples. At all temperatures, a strong PL band E_O and a weak shoulder E_C are present in the spectra of the BaCuSF powder aged for 5 years in ambient room atmosphere (Fig. 6.6c). Therefore, this band is attributed to recombination through oxygen-related defects. No PL was observed for the BaCuTeF thin films or powders. Absorption spectra of S-poor BaCuSF thin film is shown in Fig. 6.6d. The inset of Fig. 6.6d depicts the experimental measurement setup. Intensity of the sub-gap absorption peak E_A decreases as the sample ages in air. Spectral positions of the experimentally observed PL and absorption peaks are summarized in Fig. 6.7b and 6.7d.

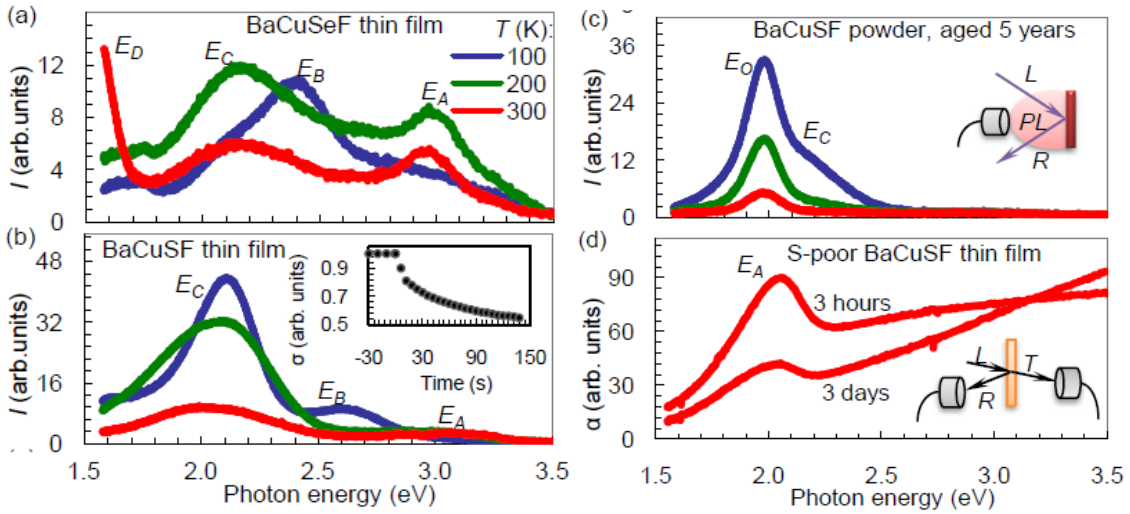

FIG. 6.6 Photoluminescence spectra of (a) BaCuSeF thin film, (b) BaCuSF thin film and (c) aged for 5 years BaCuSF powder measured at different temperatures.(d) Optical absorption spectra of a S-poor BaCuSF thin film measured 3 hours and 3 days after removal from vacuum. Insets: (b) normalized conductivity of BaCuSF thin film after the light exposure, (c and d): schematics of the experiments

The points of change of slope in the lines in Fig. 6.4 correspond to V_{Cu} and V_{Ch} defect transition levels calculated from data in Table 6.3. $V_{Cu}^{0/-1}$ transition level is below the valence band maximum E_V. Therefore, for any E_F in the gap V_{Cu} will be charged. With increasing E_F, doubly-charged V_{Ch}^{+2} state changes to the neutral V_{Ch}^{0} state, so V_{Ch} is a "negative *U*" center, similar to V_O in ZnO and V_{Ch} in chalcopyrites.[34] All the V_{Ch} transition levels ($V_{Ch}^{0/+2}$, $V_{Ch}^{0/+1}$ and $V_{Ch}^{+1/+2}$) and $O_S^{0/+1}$ transition level are deep in the gap. Positions of these transition levels with respect to BaCuChF band edges are summarized in Fig. 6.7a and 6.7c

We attribute PL, absorption and PPC observed in BaCuChF samples to optical recombination and absorption through deep donor-like defect levels. The proposed PL model is schematically shown in Fig. 6.7e. A positively-charged donor level traps a photo-excited electron by electrostatic attraction, and this trapped electron radiatively recombines with a free hole from the valence band. Similarly, absorption peak is caused by optical transition of the electrons from the valence band to charged deep donor-like defects. Finally, PCC is caused by slow relaxation of donor-like defects to their equilibrium charge state after light exposure was removed.[34]

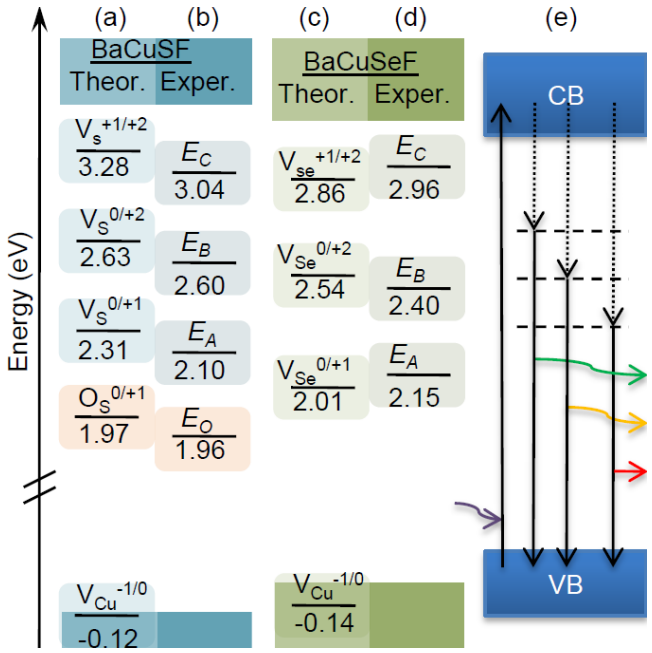

FIG. 6.7 (a and c) Theoretical defect transition levels and (b and d) experimental spectral positions of the photoluminescence and absorption peaks in (a and b) BaCuSF and (c and d) BaCuSeF. (e) Proposed mechanism of the photoluminescence.

The most likely donor-like defect that causes PL, absorption and PPC in BaCuSF and BaCuSeF thin films is a dominant donor-like defect, chalcogen vacancy V_{Ch}, and there are several supporting observations. First, the absorption peak E_A was observed only in a specially prepared S-poor BaCuSF samples. This peak decreased upon aging the thin film in air, most likely due to filling the chalcogen vacancies with oxygen. Second, observed PPC is a signature of chalcogen vacancies in other materials.[34] Third, E_O PL band appears only in the aged in air BaCuSF powders, and its spectral position agrees with the $O_{Ch}^{0/+1}$ transition level. Fourth, large tensile strain was observed experimentally in S-poor BaCuSF thin films compared to BaCuSF powders.[22] Theoretically, we found that addition of V_{Cu} induced compressive strain, and that V_{Ch} induces tensile strain compared to the reference calculation. Within the proposed model, we attribute appearance of the peak E_B at low temperature (Fig. 6.6a and 6.6b) to filling of the traps that correspond to E_A and E_C (Fig. 6.7b and 6.7d), but exact physical mechanism of recombination through the $O_{Ch}^{0/+2}$ transition level that corresponds to E_B remains unclear.

Spectral positions of PL and absorption peaks (Fig. 6.7b and 6.7d) are close to the calculated transition levels of V_{Ch} (Fig. 6.7a and 6.7c). Small deviation between theory and experiment has two possible reasons. First, theoretical transition levels were determined from the result of two fully relaxed defect calculations, for which the defect atomic configurations were different. This is not likely to be the case in the experimental absorption or emission process, since the atom relaxation happens much slower than photon emission.[34] Second, deep donor transition levels are affected by the DFT band gap underestimation, and can change depending on the calculation technique or the band gap correction method.[35] GW calculations would be required to eliminate this error, but they are too computationally expensive to perform at the present time.

The absence of the peaks in the BaCuTeF PL spectrum is attributed to a different character of the lowest conduction band in this material compared to BaCuSF and BaCuSeF. In BaCuTeF, the conduction band minimum (CBM) is composed of Cu and Ba atomic orbitals, whereas the CBM in BaCuSF and BaCuSeF has partly Ch character.[23] When the photoexcited electron in BaCuTeF relaxes to the lowest conduction band, it is spatially separated from tellurium vacancies and therefore cannot be trapped, and cannot recombine emitting a photon, as it happens in BaCuSF and BaCuSeF. Since PL in BaCuTe is not observed, the recombination must be happening fully nonradiatively.

6.3.4. Oxygen-related defects

BaCuChF surfaces are strongly oxidized when exposed to air,[3] necessitating *in-situ* processing to implement BaCuChF materials in chalcogenide thin film solar cells.[2] As shown in Fig. 6.4, BaCuChF surface Fermi levels measured by XPS (E_F^{XPS})[3] are larger than the bulk Fermi levels calculated from the experimental concentration of free holes in epitaxial BaCuChF thin films (E_F^{Hall})[22]. This indicates that the BaCuChF bands bend down towards the grain boundaries and may cause the scattering of the free holes. Experimental ratio in mobilities of free holes in polycrystalline and epitaxial BaCuTeF thin films is 27.[25] Since the ratio of average to in-plane effective mass is only 3,[23] a factor of 9 must come from the difference in the carrier mean free path. Therefore, grain boundaries have three times stronger effect of the charge carrier transport than the crystal

structure anisotropy in BaCuChF. Similar should hold for LaCuOCh with low mobility of free holes in polycrystalline samples. On the other hand, isostructural BiCuOCh has essentially the same mean-free path for both polycrystalline and epitaxial samples.[36] This may be caused by a smaller tendency of Bi to oxidize and by a better transport of holes through Bi-O grain boundaries compared to Ba-O and La-O grain boundaries. These observations give guidance for chemical design of new *p*-type transparent chalcogenides with high mobility of free holes in polycrystalline samples. Such materials may contain only cations like Bi, Ni, Cu, *etc.* that have naturally *p*-type conductive oxides (BiO, NiO, Cu_2O, *etc*).

Oxygen is a likely surface oxidant and bulk contaminant in BaCuChF materials,[3,5] but *p*-type doping with oxygen in related SrCuChF materials is difficult.[37] We calculated formation enthalpies of the most likely oxygen-related defects in BaCuChF (Table 6.3). We found that formation enthalpies of the oxygen-related defects are smaller compared to the dominant intrinsic defects and therefore they would not affect bulk BaCuChF transport properties. Even at the assumed O-rich/F-poor/Cu-rich conditions (Table 6.2), the concentration of the most likely oxygen-related defect O_F^{-1} in bulk BaCuChF (10^{15}-10^{17} cm^{-3}) is negligible compared to concentration of the main native point defects. At the other synthesis conditions (points "*B*" and "*C*" in Fig. 6.3b) O_{Ch}^{+1} and O_{Ch}^{-1} are more likely than O_F^{-1}, but their concentrations are still much smaller compared to those of the native point defects.

6.3.5. Defect complexes

BaCuChF materials have several possible defect complexes that are energetically favorable compared to the isolated defects. For example, a neutral $[V_{Ch}^{2+}+2V_{Cu}^{-1}]^0$ defect complex is more likely to form than non-interacting V_{Cu}^{-1} and V_{Ch}^{+2} (Table 6.3). Such defect complexes are likely, because at the equlibirium Fermi level formation enthalpies of V_{Cu}^{-1} and V_{Ch}^{2+} are low (Fig. 6.4) and the defect concentrations are large (10^{20}-10^{21} cm^{-3}). In addition, both defects are located in the same Cu-Ch layer of the BaCuChF crystal structure (Fig. 6.1). The $[2V_{Cu}^{-1}+V_{Ch}^{2+}]^0$ neutral defect complex will not affect the concentration of chare carriers, but would lead to lower charge carrier mobility due to

disorder in the Cu-Ch layers of BaCuChF crystal structure. Additional energy gain to form a defect complex comes from ordering of the defect complexes. For example, in $CuInSe_2$ and related chalcopyrites, ordered arrays of the defect complexes leads to formation of ordered defect compounds.[13]

Defect pairs in BaCuChF can also be formed by relaxation of substitutional defects. A substitutional defect F_{Ch} was found to relax far from its original location towards the Ba plane, so that the final configuration looks like a $[V_{Ch}^{+2}+F_I^{-1}]^{+1}$ defect complex and is similar to a Frenkel vacancy-interstitial pair in binary semiconductors. This defect complex is positively charged and can trap an electron in which case a deep energy level appears ~1 eV below the conduction band minimum. Large relaxation, Frenkel pair-like character and a deep gap state are all signatures of the impurity DX centers in binary semiconductors.[38] Recently, it was shown that intrinsic DX centers can form in mixed-cation $CuGaSe_2$ by large relaxation of Ga_{Cu} substitutional defect into $[Ga_I^{+1}+V_{Cu}^{-1}]^0$ defect pair that acts like a Ga_{DX} center.[39] Therefore, it is likely that in mixed-anion BaCuChF relaxed F_{Ch} substitutional defect can act as a DX center. Another way for the $[V_{Ch}^{+2}+F_I^{-1}]^{+1}$ pair to keep the chare balance is to pair up with V_{Cu}^{-1} and form a neutral $[V_{Ch}^{+2}+F_I^{-1}+V_{Cu}^{-1}]^0$. Both $[V_{Ch}^{+2}+F_I^{-1}]^{+1}$ and $[V_{Ch}^{+2}+F_I^{-1}+V_{Cu}^{-1}]^0$ defect complexes have negative formation enthalpy with respect to the isolated defects they are composed of. F_I defects are also known to have a low formation enthalpy in other wide-bandgap compounds.[40]

6.4 Summary and conclusions

We reported results of the DFT calculations of native point defects, defect complexes and oxygen impurities in BaCuChF semiconductors. Based on the calculation results, we propose a defect model that comprises of V_{Cu}^{-1} and V_{Ch}^{+2} defects to explain the unintentional *p*-type conductivity in BaCuChF and the increase of the conductivity in the S-Se-Te series. Proposed theoretical model is consistent with experimental results of transport, optical and photoemission spectroscopy measurements. Results of this work lead to a conclusion that extrinsic doping oif BaCuChF would be difficult, that these

materials are suitable for transparent *p*-type contact applications, but not suitable for fabrication of field-effect transistors with *p*-type channels.

References

[1] J. Tate, P. F. Newhouse, R. Kykyneshi, P. A. Hersh, J. Kinney, D. H. McIntyre, and D. A. Keszler, Thin Solid Films **516**, 5795 (2008).

[2] A. Zakutayev et.al, accepted to Appl. Phys. Lett.

[3] A. Zakutayev et.al, accepted to Journ. Appl. Phys.

[4] H. Yanagi, J. Tate, S. Park, C. -H. Park, and D. A. Keszler, Appl. Phys. Lett. **82**, 2814 (2003).

[5] C.-H. Park, R. Kykyneshi, A. Yokochi, J. Tate, and D. A. Keszler, J. Solid State Chem.**180**, 1672 (2007).

[6] K. Ueda, S. Inoue, S. Hirose, H. Kawazoe, and H. Hosono, Appl. Phys. Lett. **77**, 2701 (2000).

[7] Y. Kamihara, T. Watanabe, M. Hirano, H. Hosono, J. Am. Chem. Soc. **130**, 3296 (2008).

[8] H. Hiramatsu, K. Ueda, H. Ohta, M. Hirano, M. Kikuchi, H. Yanagi, T. Kamiya, H. Hosono, Appl. Phys. Lett. **91**, 012104 (2007).

[9] S. Lany, V. Ostheimer, H. Wolf, T. Wichert, Physica B: Condensed Matter **308,** 958 (2001)

[10] S. Lany and A. Zunger, Phys. Rev. Lett. **98**, 045501 (2007).

[11] C. G. Van de Walle, Phys. Rev. Lett. **85**, 1012 (2000).

[12] S. B. Zhang, S.-H. Wei, and A. Zunger, Phys. Rev. B **63**, 075205 (2001).

[13] S. B. Zhang, S.-H. Wei, A. Zunger, and H. Katayama-Yoshida, Phys. Rev. B **57**, 9642 (1998).

[14] S.-H. Wei and S.B. Zhang, J. Phys. Chem. Solids **66**, 1994 (2005).

[15] D. O. Scanlon, A.Walsh, and G.W. Watson, Chem. Mater. **21**, 4576 (2009)

[16] J. Robertson, K. Xiong, and S.J. Clark, Thin Solid Films **496**, 1 (2006).

[17] M. Nolan, Thin Solid Films **516,** 8130 (2008)

[18] S. Chen, X. G. Gong, A. Walsh, and S.-H. Wei, Appl. Phys. Lett. **96**, 021902 (2010).

[19] A. Nagoya, R. Asahi, R. Wahl, and G. Kresse, Phys. Rev. B **81**, 113202 (2010).

[20] C. Persson, Y.-J. Zhao, S. Lany, and A. Zunger, Phys. Rev. B **72**, 035211 (2005).

[21] G. Kresse, J. Furthmüller, Phys. Rev. B **54**, 11169 (1996).

[22] A. Zakutayev et.al, accepted to Thin Solid Films

[23] A. Zakutayev et.al, accepted to Phys. Rev. B

[24] G. Makov and M. C. Payne, Phys. Rev. B **51**, 4014 (1995)

[25] R. Kykyneshi, D.H. McIntyre, J. Tate, C.-H. Park, and D.A. Keszler, Solid State Sciences **10**, 921 (2008).

[26] Y. Hishikawa, N. Nakamura, S. Tsuda, S. Nakano, Y. Kishi, and Y. Kuwano, Jpn. J. Appl. Phys. **30**, 1008 (1991)

[27] D. R. Lide, *CRC Handbook of Chemistry and Physics* (CRC Press, 2004).

[28] J. E. Jaffe and Alex Zunger, Phys. Rev. B **27**, 5176 (1983).

[29] S.-H. Wei and A. Zunger, Appl. Phys. Lett. **72**, 2011 (1998).

[30] S. Lany, J. Osorio-Guillen, and A. Zunger, Phys. Rev. B **75**, 241203 (2007).

[31] X.Nie, S.-H.Wei, S. B. Zhang, Phys. Rev. Lett. **88**, 066405 (2002)

[32] A. Walsh, J. L. F. Da Silva, S.-H.Wei, C. Korber, A. Klein, L. F. J. Piper, A. DeMasi, K. E. Smith, G. Panaccione, P. Torelli, D. J. Payne, A. Bourlange, R. G. Egdell, Phys. Rev. Lett. **100**, 167402 (2008).

[33] R. Kykyneshi, Ph.D. thesis, Oregon State University (2007)

[34] S. Lany and A. Zunger, Phys. Rev. B **72**, 035215 (2005).

[35] S. Lany and A. Zunger, Phys. Rev. B **78**, 235104 (2008).

[36] A. Zakutayev, et. al., submitted to Appl. Phys. A

[37] H. Kabbour, L. Cario, S. Jobic, and B. Corraze, J. Mater. Chem. **16**, 4165 (2006).

[38] D. J. Chadi and K. J. Chang, Phys. Rev. Lett. **61**, 873 (1988).

[39] S. Lany and A. Zunger, Phys. Rev. Lett. **100**, 016401 (2008).

[40] A. Janotti, E. Snow, and C. G. Van de Walle, Appl.Phys. Lett. **95**, (2009).

CHAPTER 7

Summary

Wide-bandgap *p*-type BaCuChF (Ch = S, Se, Te) thin films and $BaCu(Ch_{1-x}Ch'_x)F$ thin film solid solutions were obtained by pulsed laser deposition at elevated substrate temperatures from alternating layers of BaCuChF and BaCuCh'F. Adjusting the thickness of the component layers varies the relative chalcogen content, which allows tunability of the film transparency and results in a conductivity change of more than three orders of magnitude. The tunability of the physical properties makes these chalcogen-based semiconductors potentially useful for engineering of optoelectronics applications. Lattice parameters of BaCuChF calculated using density functional theory agree with those previously reported for the powders. Deviations from Vegard's law are observed in $BaCu(S_{1-x}Se_x)F$ thin films with large sulfur content.

Double excitonic absorption peaks are observed in textured BaCuSF and BaCuSeF thin films. The excitonic doublet separation increases with increasing fraction of heavy chalcogen in the thin-film solid solutions, in good agreement with the spin-orbit splitting of the valence bands calculated by density functional theory (DFT). In BaCuSF and BaCuSeF, the excitons have large binding energies (95 meV and 65 meV, respectively) and can be observed at room temperature. A three-dimensional Wannier-Mott excitonic absorption model gives good agreement between the experimental and theoretical optical properties. Band gaps of BaCuSF and BaCuSeF calculated using the GW approximation agree with experiment. In BaCuTeF, transitions across the lowest direct energy gap and excitonic absorption are suppressed, extending its transparent range.

BaCuChF compounds oxidize when exposed to ambient atmosphere, but Se capping layers can be used to protect the surfaces outside of the vacuum chamber. Decapped BaCuSeF surfaces remain O- and C-free when the Se layer is evaporated, but they become F-deficient. These BaCuSeF surfaces have work functions of 4.85 eV and Fermi levels located 0.25 eV above the valence band maximum.

In-situ stepwise deposition of zinc phthalocyanine (ZnPc) on a BaCuSeF film surface produced a chemically inert interface with a hole-injection barrier of 0.11 eV, which is suitable for the applications in organic light-emitting and organic photovoltaic devices. *In-situ* formed *BaCuSeF/ZnTe* contact is characterized by a null valence-band

offset, a large conduction-band offset, and a chemically graded interface. By applying the transitivity rule for band offset and on the basis of similarities in chemical composition, BaCuSeF contact to chalcogenide photovoltaic absorber materials would be expected to have similar properties. Therefore, BaCuChF (Ch = S, Se, Te) materials are suitable as *p*-layers in *p*-*i*-*n* double-heterojunction solar cells fabricated with CdTe, $Cu(InGa)Se_2$, and Cu_2ZnSnS_4 absorbers.

Finally, the origin of *p*-type conductivity in BaCuChF materials was elucidated. Unintentional *p*-type conductivity in BaCuChF is explained by the presence of copper vacancies with transition levels in the valence band. These acceptor-like defects are partially compensated by donor-like chalcogen vacancies with the transition levels deep in the gap. Chalcogen vacancies also cause experimentally observed sub-gap photoluminescence, optical absorption and persistent photoconductivity in BaCuSF and BaCuSeF. In thermodynamic equilibrium, both copper and chalcogen vacancies have low formation enthalpies and are likely to form defect complexes among themselves and with fluorine interstitials. Calculated Fermi level pinning range in BaCuChF is narrow and close to the valence band maximum. This makes BaCuChF a suitable transparent *p*-type contact for optoelectronic applications, but hinters the attempts to fabricate transparent thin film transistors using this material. Oxygen-related defects do not affect bulk BaCuChF properties, but surface oxidation decreases mean free path of free holes by almost an order of magnitude.

In conclusion, BaCuChF thin films prepared by pulsed laser deposition are suitable for application as *p*-contact in PV devices and OLEDs because they have wide band gaps, tunable optical and electrical transport properties, and form good contact to organic and inorganic semiconductors used in optoelectronic devices. According to the results of the density functional theory defect calculations, BaCuChF materials are not suitable for *p*-channel applications in TFETs due to high concentration of free holes and narrow Fermi level pinning range caused by the presence of defects in these materials.

The obvious next research step is to implement BaCuChF wide-bandgap semiconductors into working PV cells and OLEDs. The best way to achieve working PV devices is to deposit all the layers *in-situ* by PLD to avoid Se capping steps and prevent

exposure to atmosphere. However, this approach would require developing the baseline devices and inserting BaCuChF functional layers into them. Proposed structures that avoid introducing Cd into the deposition chamber include SiO_2/ZnO:Al/Zn(OS)/SnS/BaCuChF/Cu with the SiO_2/ZnO:Al/Zn(OS)/SnS/Au baseline device, or similar structures based on new Cu_3PCh_4 absorbers, SiO_2:Na/Cu/BaCuChF/CIGS/Zn(OS)/ZnO:Al with a SiO_2:Na/Mo/CIGS/Zn(OS)/ZnO:Al baseline device or similar structures based on Cu_2ZnSnS_4 absorbers. Preliminary results indicate that SnS films prepared from SnS_2 target by PLD have very low concentration of free holes (10^{14} - 10^{16} cm^{-3}), so it may be possible to dope this material *n*-type and fabricate SnS homojunction solar cells with the aforementioned configuration. In addition to device fabrication and SnS doping studies, it would be beneficial to perform direct interfacing experiments of BaCuSeF with SnS, CIGS, CdTe and CZTS at the Darmstadt University of Technology (Germany) to directly evaluate the band line-up.

It would not be possible to use *in-situ* processing to achieve working OLEDs, because preparation of organic layers using PLD is difficult. Therefore, outside expertise in organic thermal evaporation may be necessary to advance this project. BaCuChF layers would have to be capped with Se and sent to the OLED collaborators for further processing.

It would be advantageous to increase the level of *p*-type doping in BaCuChF, but since the Fermi level pinning range in BaCuChF is narrow, it makes no sense to introduce extrinsic dopants. Therefore, PLD process conditions would have to be optimized to minimize the loss of Ch to achieve the maximum concentration of free holes. The most feasible way to achieve these favorable growth conditions is by developing and using Ch co-evaporation in the OSU PLD chamber. Another technological task is to develop a sputtering protocol to deposit BaCuChF materials. This would ease the transfer of the BaCuChF technology to industry.

Finally, the conclusions drawn from development of BaCuChF materials may to be extended to search for new ambipolar-dopable wide-bandgap semiconductors. Such materials would be usable for both active and passive applications. One approach to this problem would be to search for narrow-bandgap materials with forbidden lowest-energy

optical transitions and high formation enthalpies of native defects. A combination of these factors would lead to both easy electrical doping and high optical transparency. To achieve this goal, a combination of chemical intuition, physical logics and electronic struture theoretical screening would be required.

BIBLIOGRAPHY

A. B. Christie, J. Lee, I. Sutherland, and J. M. Walls, Appl. Surf. Sci. **15**, 224 (1983).

A. Barati, A. Klein, and W. Jaegermann, Thin Solid Films **517**, 2149 (2009).

A. Gauzzi, H. J. Mathieu, J. H. James, and B. Kellett, Vacuum **41**, 870 (1990).

A. Janotti, E. Snow, and C. G. Van de Walle, Appl.Phys. Lett. **95**, (2009).

A. Kahn, N. Koch, and W.Gao, J. Polym. Sci., Part B **41**, 2529 (2003).

A. Luque and S. Hegedus, *Handbook of Photovoltaic Science and Engineering* (John Wiley and Sons, 2003).

A. N. Banerjee, K. K. Chattopadhyay, Prog. Cryst. Growth Charact. Mater. **50,** 52(2005).

A. Nagoya, R. Asahi, R. Wahl, and G. Kresse, Phys. Rev. B **81**, 113202 (2010).

A. R. Beal, J. C. Knights, and W. Y. Liang, Journal of Physics C: Solid State Physics **5**, 3531-3539 (1972).

A. R. Beal, W. Y. Liang, J. Phys. C: Solid State Phys. **9**, 2459 (1976).

A. Walsh, J. L. F. Da Silva, S.-H.Wei, C. Korber, A. Klein, L. F. J. Piper, A. DeMasi, K. E. Smith, G. Panaccione, P. Torelli, D. J. Payne, A. Bourlange, R. G. Egdell, Phys. Rev. Lett. **100**, 167402 (2008).

A. Zakutayev, D. H. McIntyre, G. Schneider, R. Kykyneshi, D. A. Keszler, C-H. Park, and J. Tate, Thin Solid Films (2010), in press

A. Zakutayev, et. al., submitted to Appl. Phys. A

A. Zakutayev, J. Tate, H. A. S. Platt, D. A. Keszler, C. Hein, T. Mayer, Andreas Klein, Wolfram Jaegermann, J. Appl. Phys., (2010) in press

A. Zakutayev, J. Tate, G. Schneider, in preparation

A. Zakutayev, J. Tate, H.A. S. Platt, D. A. Keszler, A. Barati, A. Klein, W. Jaegermann, Appl. Phys. Lett., (2010) in press

A. Zakutayev, R. Kykyneshi, G. Schneider, D. H. McIntyre and J. Tate, Phys. Rev. B 81, 155103 (2010)

B. D. Cullity, S. R. Stock, Elements of X-Ray Diffraction (3rd Edition), Prentice Hall, Englewood Cliffs, NJ, 2001.

B. J. Gibbons, Y. Fan, A. T. Findikoglu, Q. X., Jia, D. W.Reagor, J. Vac. Sci. Technol., A **19,** 56(2001)

B. Späth, J. Fritsche, A. Klein, and W. Jaegermann, Appl. Phys. Lett. **90**, 062112 (2007).

B. Späth, K. Lakus-Wollny, J. Fritsche, C. S. Ferekides, A. Klein, and W. Jaegermann, Thin Solid Films **515**, 6172 (2007).

C. G. Granqvist, Sol. Energy Mater. Sol. Cells **91**, 1529 (2007).

C. G. Van de Walle, Phys. Rev. Lett. **85**, 1012 (2000).

C. Goyhenex, H. Bulou, J. P. Deville, G. Tréglia, Appl. Surf. Sci. **177,** 238 (2001).

C. Persson, Y.-J. Zhao, S. Lany, and A. Zunger, Phys. Rev. B **72**, 035211 (2005).

C.-H. Park, D. A. Keszler, H. Yanagi, and J. Tate, Thin Solid Films **445**, 288 (2003).

D. B. Chrisey, G. K. Graham, Pulsed Laser Deposition of Thin Films, John Wiley and Sons, New York, NY, 1994

D. Brion, Appl. Surf. Sci. **5**, 133 (1980).

D. Cahen, P. J. Ireland, L. L. Kazmerski, and F. A. Thiel, J. Appl. Phys. **57**, 4761 (1985).

D. F. Marron, T. Glatzel, A. Meeder, T. Schedel-Niedrig, S. Sadewasser, and M. C. Lux-Steiner, Appl. Phys. Lett. **85**, 3755-3757 (2004).

D. J. Chadi and K. J. Chang, Phys. Rev. Lett. **61**, 873 (1988).

D. O. Scanlon, A.Walsh, and G.W. Watson, Chem. Mater. **21**, 4576 (2009)

D.R. Lide, *CRC Handbook of Chemistry and Physics* (CRC Press, 2004).

E. Motomitsu, H. Yanagi, T. Kamiya, M. Hirano, and H. Hosono, J. Solid State Chem. **179**, 1668 (2006).

F. D. Murnaghan, Proc. Natl. Acad. Sci. U.S.A. **30,** 244(1944).

G. Kresse, J. Furthmüller, Phys. Rev. B **54**, 11169(1996).

G. Makov and M. C. Payne, Phys. Rev. B **51**, 4014 (1995)

G. Teeter, J. Appl. Phys. **102**, 034504 (2007).

H. Hiramatsu, I. Koizumi, K.-B. Kim, H. Yanagi, T. Kamiya, M. Hirano, N. Matsunami, and H. Hosono, J. Appl. Phys. **104**, 113723 (2008).

H. Hiramatsu, K. Ueda, H. Ohta, M. Hirano, M. Kikuchi, H. Yanagi, T. Kamiya, H. Hosono, Appl. Phys. Lett. **91**, 012104 (2007).

H. Hiramatsu, K. Ueda, H. Ohta, M. Hirano, T. Kamiya, H. Hosono, Appl. Phys. Lett. **82,** 1048(2003).

H. Hiramatsu, K. Ueda, H. Ohta, T. Kamiya, M. Hirano, Appl. Phys. Lett. **87**, 211107 (2005).

H. Hiramatsu, K. Ueda, K.Takafuji, H. Ohta, M. Hirano, T. Kamiya, H. Hosono, J. Appl. Phys. **94**, 5805 (2003).

H. Kabbour, L. Cario, S. Jobic, and B. Corraze, J. Mater. Chem. **16**, 4165 (2006).

H. Kawazoe, M. Yasukawa, H. Hyodo, M. Kurita, H. Yanagi, H. Hosono, Nature **389,** 939(1997).

H. Peisert, M. Knupfer, T. Schwieger, and J. Fink, Appl. Phys. Lett. **80**, 2916 (2002).

H. Yanagi, S. Ohno, T. Kamiya, H. Hiramatsu, M. Hirano, H. Hosono, J. Appl. Phys. **100**, 033717 (2006).

H. Yanagi, J. Tate, S. Park, C.-H. Park and D. A. Keszler, Appl. Phys. Lett., **82**, 2814 (2003).

H. Yanagi, J. Tate, S. Park, C.-H. Park, D. A. Keszler, M. Hirano, and H. Hosono, J. Appl. Phys. **100**, 083705 (2006).

H. Yanagi, M. Kikuchi, K.-B. Kim, H. Hiramatsu, T. Kamiya, M. Hirano, and H. Hosono, Organic Electronics **9**, 890 (2008).

H. Yanagi, S. Park, A. D. Draeseke, D. A. Keszler, and J. Tate, J. Solid State Chem. **175**, 34 (2003).

http://www.asiinstr.com/technical/dielectric%20constants.htm

I. Barin, F. Sauert, E. Schultze-Rhonhof, and W. Shu Sheng. *Thermochemical Data of Pure Substances* (VCH, New York, 1993).

J. A. Frantz, J. S. Sanghera, V. Q. Nguyen, S. S. Bayya, S. B. Qadri, and I. D. Aggarwal, Mater. Lett. **62**, 1582 (2008).

J. A. Spies, R. Schafer, J. F. Wager, P. Hersh, H. A. S. Platt, D. A. Keszler, G. Schneider, R. Kykyneshi, J. Tate, X. Liu, A. D. Compaan, W. N. Shafarman, Solar Energy Materials & Solar Cells **93**, 1296 (2009).

J. C. Scott, J. Vac. Sci. Technol. A **21**, 521 (2003).

J. E. Jaffe and Alex Zunger, Phys. Rev. B **27**, 5176 (1983).

J. E. Medvedeva: Europhys. Lett. **78,** 57004(2007).

J. F. Muth, R. M. Kolbas, A. K. Sharma, S. Oktyabrsky, J. Narayan J. Appl. Phys. **85**, 7884 (1999).

J. F. Wager, D. A. Keszler, and R. E. Presley, *Transparent Electronics* (Springer, 2007).

J. Fritsche, A. Klein, and W. Jaegermann, Adv. Eng. Mater. **7,** 914 (2005).

J. I. Pankove, *Optical Processes in Semiconductors* (Courier Dover Publications, Mineola, NY, 1975).

J. Narayan, A. K. Sharma, A. Kvit, C. Jin, J. F. Muth, O. W. Holland, Solid State Commun. **121,** 9(2001).

J. Paier, R. Asahi, A. Nagoya, and G. Kresse, Phys. Rev. B **79**, 115126 (2009).

J. Robertson, K. Xiong, and S.J. Clark, Thin Solid Films **496**, 1 (2006).

J. Tate, P. F. Newhouse, R. Kykyneshi, P. A. Hersh, J. Kinney, D. H. McIntyre, and D. A. Keszler, Thin Solid Films **516**, 5795 (2008).

K. Ellmer, A. Klein, and B. Rech, *Transparent Conductive Zinc Oxide* (Springer, 2008).

K. Ishida, Y Nakai, and H Hosono, J. Phys. Soc. Jpn. **78**, (2009).

K. Ueda, H. Hiramatsu, H. Ohta, M. Hirano, T. Kamiya, H. Hosono, Phys. Rev. B 69, 155305 (2004)

K. Ueda, H. Hiramatsu, M. Hirano, T. Kamiya, H. Hosono, Thin Solid Films **496**, 8 (2006).

K. Ueda, H. Hosono, N. Hamada, J. Phys.: Condensed Matter **16**, 5179 (2004)

K. Ueda, S. Inoue, H. Hosono, N. Sarukura, M. Hirano, Appl. Phys. Lett. **78**, 2333 (2001).

K. Ueda, S. Inoue, S. Hirose, H. Kawazoe, and H. Hosono, Appl. Phys. Lett. **77**, 2701 (2000).

L. A. Knauss, J. M. Pond, J. S. Horwitz, D. B. Chrisey, C. H. Mueller, R. Treece, Appl. Phys. Lett. **69,** 25(1996).

L. B. Freund and Subra Suresh, Thin Film Materials, Cambridge University Press, Cambridge, UK, 2003.

L. S. Hung and C. H. Chen, Mater. Sci. Eng. R **39**, 143 (2002).

M. D. Irwin, D. B. Buchholz, A.W. Hains, R. P. H. Chang, T. J. Marks, Proc. Natl. Acad. Sci. U.S A. **105,** 2783(2008).

M. Nolan, Thin Solid Films **516,** 8130 (2008)

M. P. Marder, *Condensed Matter Physics*, (John Wiley, New York,2000).

M. Shishkin, G. Kresse, Phys. Rev. B **75**, 235102 (2007).

M. Weinert, G. Schneider, R. Podloucky, J. Redinger, J. Phys.: Condens. Matter **21**, 084201 (2009).

M. Yasukawa, K. Ueda, H. Hosono, J. Appl. Phys. **95**, 3594 (2004).

MRS bsulletin, August 2000

N. Papageorgiou, E. Salomon, T. Angot, J.-M. Layet, L. Giovanelli, and G. L. Lay, Prog. Surf. Sci. 77, 139 (2004).

N. Peyghambarian, S. W. Koch, A. Mysorowicz, *Introduction to Semiconductor Optics*, (Prentice Hall, Englewood Cliffs, NJ, 1993).

N. Ueda, H. Maeda, H. Hosono, H. Kawazoe, J. Appl. Phys. **84**, 6174 (1998).

N. W. Ashcroft, N. D. Mermin, *Solid State Physics*, (Holt, Rinehart, and Winston, New York, 1976).

P. Blaha, K. Schwarz, G. Madsen, D. Kvasnicka, J. Luitz, WIEN2k, An Augmented Plane Wave + Local Orbitals Program for Calculating Crystal Properties (Karlheinz Schwarz, Techn. Universität Wien, Austria), 2001.

P. F. Newhouse, C.-H. Park, D. A. Keszler, J. Tate, P. S. Nyholm, Appl. Phys. Lett. **87**, 112108 (2005).

R. J. Zollweg, Phys. Rev. **111**, 113 (1958).

R. Kykyneshi, D. H. McIntyre, J. Tate, C.-H. Park, and D. A. Keszler, Solid State Sci. **10**, 921 (2008).

R. Kykyneshi, Ph.D. Thesis, Department of Physics, Oregon State University, USA, 2007.

R. Kykyneshi, Ph.D. thesis, Oregon State University (2007)

S. B. Zhang, S.-H. Wei, A. Zunger, and H. Katayama-Yoshida, Phys. Rev. B **57**, 9642 (1998).

S. B. Zhang, S.-H. Wei, and A. Zunger, Phys. Rev. B **63**, 075205 (2001).

S. Chen, X. G. Gong, A. Walsh, and S.-H. Wei, Appl. Phys. Lett. **96**, 021902 (2010).

S. J Fonash, *Solar Cell Device Physics* (Academic Press, 1981).

S. Lany and A. Zunger, Phys. Rev. B **72**, 035215 (2005).

S. Lany and A. Zunger, Phys. Rev. B **78**, 235104 (2008).

S. Lany and A. Zunger, Phys. Rev. Lett. **100**, 016401 (2008).

S. Lany and A. Zunger, Phys. Rev. Lett. **98**, 045501 (2007).

S. Lany, J. Osorio-Guilln, and A. Zunger, Phys. Rev. B **75**, 241203 (2007).

S. Lany, V. Ostheimer, H. Wolf, T. Wichert, Physica B: Condensed Matter **308,** 958 (2001)

S. Park, D. A. Keszler, M. M. Valencia, R. L. Hoffman, J. P. Bender, J. F. Wager, Appl. Phys. Lett. **80,** 4393(2002).

S. Shionoya, W. M. Yen, *Phosphor Hanbook*, (CRC Press, Boca Raton, FL, 1998).

S. Siebentritt, U. Rau, *Wide-Gap Chalcopyrites*, (Springer, Berlin, 2006).

S. Tokito, K. Noda, and Y. Taga, J. Phys. D **29**, 2750 (1996).

S.-H. Wei and A. Zunger, Appl. Phys. Lett. **72**, 2011 (1998).

S.-H. Wei and S. B. Zhang, J. Phys. Chem. Solids **66**, 1994 (2005).

T. Kamiya, K. Ueda H. Hiramatsu, H. Kamioka, H. Ohta, M.Hirano, H. Hosono, Thin Solid Films **486**, 98 (2005).

T. Schulmeyer, Ph.D. Thesis, Technische Universität Darmstadt, 2005

T. Schulmeyer, R. Hunger, A. Klein, W. Jaegermann, and S. Niki, Appl. Phys. Lett. **84**, 3067 (2004).

T. Schulmeyer, R. Hunger, M. Lebedev, W. Jaegermann, A. Klein, R. Kniese, M. Powalla, Thin Solid Films **480-481**, 110 (2005).

U. Ozgur, Ya. I. Alivov, C. Liu, A. Teke, M. A. Reshchikov, S. Dogan, V. Avrutin, S.-J. Cho, and H. Morkoc, J. Appl. Phys. **98,** 041301(2005).

U. Weiler, T. Mayer, W. Jaegermann, C. Kelting, D. Schlettwein, S. Makarov, and D. Wöhrle, J. Phys. Chem. B **108**, 19398 (2004).

W. J. Zhu, Y. Z. Huang, F. Wu, C. Dong, H. Chen, and Z. X. Zhao, Mater. Res. Bull. **29**, 505 (1994).

W. Jaegermann, A. Klein, and T. Mayer, Adv. Mater. **21**, 4196 (2009).

X.Nie, S.-H.Wei, S. B. Zhang, Phys. Rev. Lett. **88**, 066405 (2002)

Y. Gassenbauer and A. Klein, J. Phys. Chem. B **110**, 4793 (2006).

Y. Hishikawa, N. Nakamura, S. Tsuda, S. Nakano, Y. Kishi, and Y. Kuwano, Jpn. J. Appl. Phys. **30**, 1008 (1991)

Y. Kamihara, H. Hiramatsu, M. Hirano, R. Kawamura, H. Yanagi, T. Kamiya, H. Hosono, J. Am. Chem. Soc. **128,** 10012 (2006).

Y. Kamihara, T. Watanabe, M. Hirano, H. Hosono, J. Am. Chem. Soc.**130,** 3297(2008).

Y. P. Varshni, Physica **34**, 149 (1967).

Y. Zhang, G. M. Dalpian, B. Fluegel, S.-H. Wei, A. Mascarenhas, X.-Y. Huang, J. Li, L.-W. Wang, Phys. Rev. Lett. **96**, 026405 (2006).

Z. Liu, X. Zhang, Y. Zhang, and J. Jiang, Spectrochim. Acta, Part A **67**, 1232 (2007).

Z. Z. You and J. Y. Dong, Appl. Surf. Sci. **249**, 271 (2005).

APPENDICES

Appendix A. Pulsed laser deposition

A.1 Introduction

Pulse laser deposition (PLD) is a popular method for the thin film growth. This technique is based on the light-matter interaction: high energy density of the beam destroys the topmost layer of the target and resulting plume expands into a vacuum and condenses on a rotating substrate. (Fig. 1a) These laser pulses are repeated until the desired thickness of the film is reached. PLD has been widely used by researchers, especially for preparation of the thin films of novel and complex materials. PLD gained its recognition in early 1990s, mainly as the best tool to deposit high-temperature superconductors.[1]

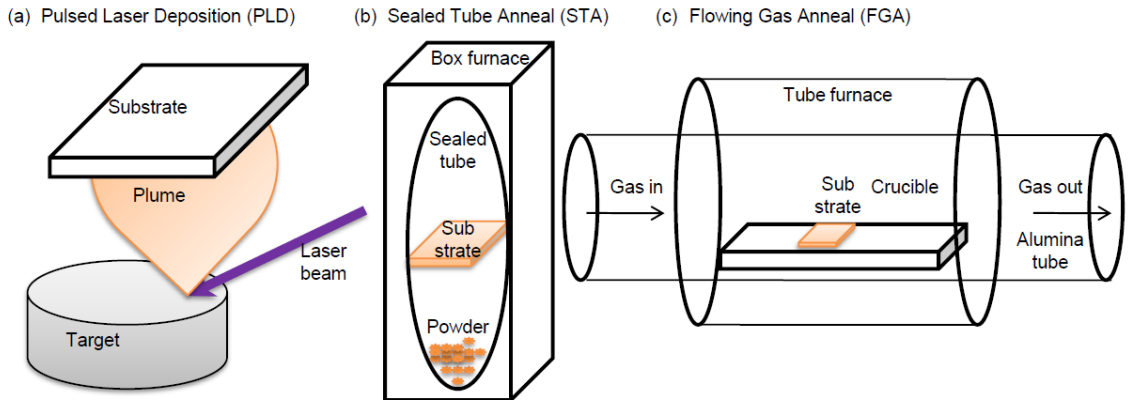

FIG. A.1 Thin film preparation methods: (a) pulsed laser deposition, (b) sealed tube anneal, and (c) flowing gas anneal

As any thin film deposition technique, PLD has its own advantages and disadvantages. The main advantages are simplicity, stoichiometric transfer of elements from the target to the substrate (in most cases), and ability to operate many chambers using one laser. Some disadvantages are small coating areas, presence of large particulates in the films and complexity brought by using the excimer lasers, such as high initial cost of the system, large area footprint and toxicity of the gases.

Overall, PLD is considered to be a great tool for research. Numerous reports are found in literature on preparation of metals,[2,3] oxides,[4,5] chalcogenides,[6] pnictides,[7,8] halides,[9] and mixed-anion compounds.[10,11] Nevertheless, the commercial applications of

PLD are limited to rare exceptions.[12,13] General overview of the PLD can be found in the book by Douglas B. Chrisey and Graham K. Hubler.[14]

PLD facilities at Oregon State University (OSU) consist of two deposition chambers. The first chambes, built by Thermionics from an OSU design, has a base pressure of 10^{-9} Torr and is mainly devoted to deposition of chalcogenides. The second chamber, designed and built by Neocera, has a lower base pressure of 10^{-7} Torr and is used for deposition of metals and oxides. Below these two chambers will be referred to as Thermionics and Neocera for simplicity. In both cases the vacuum is provided by combination of a turbomolecular pump with either oil-sealed (Thermionics) or dry (Neocera) mechanical pumps. The main reason that the Neocera base pressure is higher is that this chamber contains one rubber gasket (at the substrate mount), since it has to be completely vented to exchange the substrate. On the other hand, Thermionics chamber contains ConFlat (CF) flanges only and is equipped with a load lock for the substrate exchange. The load lock is a small vacuum chamber that can be isolated from the main system and vented/pumped in relatively short times. The substrate and the target for the PLD are inserted into the load lock and transferred into the main chamber without breaking the vacuum. This is a very important feature that helps to provide a low base pressure of the Thermionics chamber. Two PLD chambers share one Lambda Physic KrF excimer laser (248 nm, 30 ns pulse, up to 600 mJ/pulse). The pulsed beam is directed through the system of mirrors and lenses on the optical tower. More details about PLD at OSU can be found in thesis of previous students.[15,16]

A.2 PLD variables and parameters

PLD has many variables that influence the resulting films. The most important are substrate temperature, pressure in the chamber, laser fluence, laser repetition rate, target-substrate distance (Z), substrate positioning (X, Y) and number of laser pulses. PLD variables can be tuned continuously. In addition, there are several parameters of the PLD, such as types of the substrate, target and gas used in the deposition that have discrete values.

A.3 Substrate temperature

Substrate temperature is one of the most important variables of the thin film growth. It influences the crystallinity of the film and its phase composition. The film can be monocrystalline (epitaxial), polycrystalline or amorphous and have one phase (be pure) or multiple phases (contain impurities). At room temperature the films are usually amorphous (BaCuChF and ionic amorphous oxide semiconductors[17]) or polycrystalline (SnS, metals). Besides crystallinity, substrate temperature affects the adhesion of the film to the substrate. For example, elemental metals tend to stick better to warm substrates,[18] but there are some exceptions, for example Sn-metal. The deposition rate of the complex compounds usually decreases with increasing temperature. In some cases there is an upper temperature limit at which the film would either re-evaportate from the substrate due to phase transition (600^{o}C for SnS),[19] melting (232^{o}C for Sn, 221^{o}C for Se) or decomposition and loss of some of the elements (loss of S and Se at 500-600^{o}C in $SnZrCh_3$ thin films).[20]

In the Thermionics chamber the substrate is heated by irradiation of the quartz lamp and the substrate temperature on the substrate is determined using a thermocouple on the substrate mount, calibrated using the IR pyrometer. The upper temperature limit of the Thermionics chamber at OSU is 700 ^{o}C. In the NeoCera chamber, the resistive substrate heater is used, so the upper limit is higher (900 ^{o}C). In this case the temperature is measured by a type-*K* thermocouple. The upper temperature limits on both systems are high enough to grow thin films of BaCuChF and many other materials chalcogenides, but some oxides require higher deposition temperatures ($Y(MnIn)O_3$,[21] LaCuOCh[22])

For depositions at elevated temperatures it is important to provide a good and spatially uniform thermal contact of the substrate to the heating block on which it is mounted. This can be achieved by polishing the heating blocks and/or mounting the substrates on a heat spreader (for example a piece of Si wafer). The interference of light in the gap between a transparent substrate and the block or heat spreader is considered to be an indication of a good thermal contact.

In addition to substrate temperature, the ramp-down rate may be important for some materials. This rate has to be high enough that the film is not decomposed after the

deposition, but low enough that film does not crack from the thermal expansion coefficient mismatch with the substrate. The critical cooling rates for decomposition and cracking vary considerably depending on the stability and thermal expansion mismatch of the materials. In the OSU PLD chambers, the ramp rate can vary from as low as 0.1 ^{o}C/min to as high as 100 ^{o}C/min (limited by natural rate of cooling of the whole system) with a typical value of 10 ^{o}C/min.

A.4 Background Pressure and Target-Substrate Distance

Pressure inside of the chamber is the other important variable of PLD, because it defines a deposition regime. There are two regimes of depositions, referred to as molecular flow and viscous flow. In the molecular flow regime ($<10^{-2}$ Torr), the vacuum is high enough that the species from the target do not scatter off the gas molecules present in the chamber. Therefore the target-substrate distance is not as important variable as in the viscous flow regime. In the viscous flow regime ($>10^{-2}$ Torr), the interaction with gas molecules causes the plume to broaden. In this mode, the substrate is usually positioned in a narrow range close to the edge of the plume (inside or outside).[23] Larger distances may lead to very low growth rate, and lower distances may result in re-sputtering and deviation of the stoichiometry of the film from that of the substrate. In addition, both too large and too small distances may result in undesirable morphology of the films. For example, the density of Sn-Zr-Ch films significantly decreases at these conditions, as evaluated by means of optical microscopy.[20]

Thermionics and NeoCera chambers at OSU are designed to operate in the molecular flow regimes. Operation in the viscous flow regime (up to 1 Torr) requires special precautions, such as slowing down the rotation of turbomolecular pumps (500 Hz for Neocera and 17500 rpm for Thermionics) and almost full closing of their gate valves. In the Thermionics chamber, the target-substrate distance can range from 1.2" to 5" chamber and can be adjusted without venting it. In the Neocera chamber, in-situ adjustment (2" – 5" range) is not possible.

A.5 Laser energy density

Laser beam energy density (fluence) defines the amount of material transferred from a target to a substrate in one pulse. Below the deposition threshold (~0.5 J/cm^2 for chalcogenides) this amount is negligibly low. There is also an upper limit of the operational fluence at which the beam starts to separate small pieces of the target, damaging it and causing rough morphology of the film. This limit depends on the density of the target and its chemical composition. For a typical 80% dense chalcogenide target the upper limit is ~3 J/cm^2. On the other hand, metallic and oxide targets often require higher energy density for the effective deposition (2 - 5 J/cm^2). The KrF excimer laser at OSU provides output energy up to 600 mJ, but up to 50% of it is being lost in the beam-shaping aperture and in the mirrors of the optical tower. The remaining 300 mJ is further reduced by finite transmittance of the chamber entrance optical port (typically 60% after 200,000 pulses). For a typical size of the focused beam (0.04 cm^2) this energy translates into the maximal energy density of ~5 J/cm^2 at the target, which is sufficient for the deposition of metals, oxides and chalcogenides.

A.6 Laser repetition rate

Laser repetition rate defines the amount of time that the atoms may diffuse before the next portion of atoms comes. For typical PLD growth conditions, the surface diffusion mean free time of an atom to find a suitable crystal site[24] is much shorter than the typical time interval between the pulses (0.1 – 1.0 s). Nevertheless the laser repetition rate appears to be important for the epitaxial and polycrystalline thin film growth. This may have to do with other processes that occur on the substrate, such as bulk diffusion, grain growth, sintering and so on.

A.7 Substrate positioning

Substrate positioning (XY) is another important variable of the PLD. The PLD plume is much more directional than the sputtering plume. The flux of the species highly depends on the angle for any material.[14] For some compounds, such as $LaAlO_3$ the plume may also have a spatial variation of the content, but not for the others, such as $SrTiO_3$.[25] There are several ways to improve the spatial uniformity of the film, such as rotation of

the substrate (possible in Thermionics, but not in Neocera), offsetting the plume and the substrate axes (possible in both systems) and off-axis deposition, when the target and the substrate planes are not parallel to each other (not possible at OSU).

A.8 Substrate

Substrate type and substrate preparation are parameters of any thin film deposition technique, including PLD. Substrates can be single-crystalline (Si, MgO, $SrTiO_3$, Al_2O_3 etc), polycrystalline (Al_2O_3, metal foils), amorphous (glass, fused silica). Another important class of the substrates is polymeric materials, for example kapton. Crystal structure of the substrate is important as a growth template for ultra-thin layers. Thermal conductivity and thermal expansion coefficient of the substrates are also important, but only for the growth at elevated temperatures.

Characterization techniques also impose some constrains of the type of the used substrates. For example, if the films are to be characterized for the transport properties (Hall and Seebeck effects), one has to choose electrically-insulating substrates. In the case of characterization techniques that involve incoming (SEM) or outgoing (XPS) electrons, the substrate is preferred to be electrically conductive to prevent charging. If the films would undergo compositional analysis (EPMA), the substrate and the film have to contain no common elements to be analyzed.

The substrate has to be properly cleaned before the deposition. The cleaning protocol at OSU consists of ultrasonic treatment in methanol and water (about 30 min total), drying with the welding-grade nitrogen and pre-deposition bake in the vacuum chamber (30 min at the deposition temperature). If the film is deposited at room temperature, the bake is usually performed at the maximum temperature of the chamber for 30 min before the deposition. The substrates can be diced in custom shapes using the ESI μVIA laser tool at ONAMI building on HP campus. The same tool can be used for the custom fabrication of shadow masks for the deposition of films, contacts or thin-film devices.

A.9 Deposition gas

Deposition gas is also an important growth parameter. The choices include inert buffer gas (typically Ar), the reactive gas (O_2, H_2, H_2S etc.) or the mixtures (95%Ar - 5%H_2). The inert gas helps scattering and slowing down the particles in the plume, whereas the reactive gas species can be incorporated in the film during its growth. The purity of the gases is crucial for the purity of the films, so typically grade 5.0 or higher grades are used (99.999% purity or better). Another possibility is deposition without introducing the gas into a chamber. In this case, the deposition environment is mostly defined by the residual gases (mostly H_2) and the vapor of the most volatile component of the target heated by the laser beam (for example, S and Se in the case of chalcogenides). Some of the deposition gases, such as H_2S are very desirable, but toxic and therefore not used at OSU. Other ways exist to compensate for the loss of the elements during the deposition, such as co-deposition and co-evaporation. Co-deposition is performed by alternating ablation of various targets. Co-evaporation is often realized for the elements with low melting point and high vapor pressure, such as S and Se. At the present time, co-evaporation is not available at OSU PLD facilities, but it is high on the wish-list for future development of the Thermionics chamber.

A.10 Target

The kind and quality of a target makes a big difference in PLD. Typically, the target is a pressed pellet of a single-phase material, but occasionally mixed-phase targets[26] or targets with intentionally added volatile impurity phases (PbO in $PbTiO_3$,[27] Li_2O in $LiCoO_2$[28]) can be used. Large single crystals have been also used as targets in PLD.[29] Mixed-phase targets are not favored because they can undergo the phase change caused by parasitic heating during the deposition.

High density of the target usually translates in a good quality of the film. Target density of 80% of theoretical density of the material is usually sufficient. Lower density is not preferred, as it results in poor film quality and destruction of the target, as in the case of the 60%-dense $Y(MnIn)O_3$ targets.[20] This parameter seems to be not so crucial for other materials systems. For example stoichiometric BaCuChF films could be deposited using a 2 J/cm^2 laser beam and a ~65%-dense target without causing damage to it.

Before the deposition, the target is polished with sand paper (400-2000 grit) to remove its surface layer modified by a previous deposition run, until the uniformly-looking target surface is achieved. This is especially important for chalcogenide semiconductors (because of surface decomposition) and for refractory metals (because of the surface modification and "sparking" effect – ejection of micron-sized metal particles that look like sparks from the surface of a target). After the target is loaded into the chamber, it is pre-ablated with the laser beam to get rid of the surface atmospheric contamination (typically 1000 laser pulses for rotated target in the Thermionics chamber and 2000 or more laser pulses for rastered target in the Neocera chamber). After the preablation, the shutter opens and the deposition begins. It is possible to load up to 6 targets at a time in each of the chambers and switch between them without braking the vacuum. In the case of the Neocera chamber this switching can be performed by a computer and therefore very fine multilayers can be deposited, for example Cu/Ta multilayer[16] and Sn/Zr multilayers.[20]

References

[1] R. K. Singh and D. Kumar, Mater. Sci. Eng., R – reports, **22**, 113 (1998).

[2] T. J. Jackson and S. B. Palmer, J. Phys. D: Appl. Phys. **27**, 1581 (1994).

[3] J. Shen, Z. Gai, and J. Kirschner, Surf. Sci. Rep. **52**, 163 (2004).

[4] D. H. A. Blank, G. Koster, G. A. J. H. M. Rijnders, E. van Setten, P. Slycke, and H. Rogalla, J. Cryst. Growth **211**, 98 (2000).

[5] O. Y. Gorbenko, S. V. Samoilenkov, I. E. Graboy, and A. R. Kaul, Chem. Mater. **14**, 4026 (2002).

[6] M. Frumar, B. Frumarova, P. Nemec, T. Wagner, J. Jedelsky, and M. Hrdlicka, J. Non-Cryst. Solids **352**, 544 (2006), and other publications by the same group

[7] H. Hiramatsu, T. Kamiya, M. Hirano, and H. Hosono, Phys. C (Amsterdam, Neth.)**469**, 657 (2009).

[8] M. Sumiya and S. Fuke, Internet Journal of Nitride Semiconductor Research **9**, (2004).

[9] S. J. Henley, M. N. R. Ashfold, and S. R. J. Pearce, Appl. Surf. Sci. **217**, 68 (2003).

[10] M. Frumar and T. Wagner, Curr. Opin. Solid St. Mat. Sci. **7**, 117 (2003).

[11]J. Tate, P. F. Newhouse, R. Kykyneshi, P. A. Hersh, J. Kinney, D. H. McIntyre, and D. A. Keszler, Thin Solid Films **516**, 5795 (2008).

[12] V. Matias, B. J. Gibbons, A. T. Findikoglu, P. C. Dowden, J. Sullard, and J. Y. Coulter, IEEE Trans. on Appl. Superc., **15**, 2735 (2005).

[13] J. Hanisch, V. Matias, J. Rowley, R. Steenwelle, B. J. Gibbons, F. Grilli, and S. Ashworth, IEEE Trans. on Applied Superc. **17**, 3577 (2007).

[14] D. B. Chrisey and G. K. Hubler, *Pulsed Laser Deposition of Thin Films*, (Wiley-Interscience, 1994).

[15] R. Kykyneshi, Ph.D. thesis, Oregon State University, 2007

[16] P. F. Newhouse, Ph.D. thesis, Oregon State University, 2008

[17] H. Hosono, J. Non-Cryst. Solids **352**, 851 (2006).

[18] J. Tate, private communication

[19] R. Sharma and Y. Chang, J. Phase Equilib. Diffus. **7**, 269 (1986).

[20] A. Zakutayev, unpublished

[21] A. E. Smith, H. Mizoguchi, K. Delaney, N. A. Spaldin, A. W. Sleight, and M. A. Subramanian, J. Am. Chem. Soc. **131**, 17084 (2009).

[22] H. Hiramatsu, H. Ohta, T. Suzuki, C. Honjo, Y. Ikuhara, K. Ueda, T. Kamiya, M. Hirano, and H. Hosono, Cryst. Growth Des. **4**, 301 (2004).

[23] B. Gibbons, private communication

[24] G. Antczak and G. Ehrlich, Surf. Sci. Rep. **62**, 39 (2007).

[25] S. A. Chambers, private communication

[26] J. C. Lee, Y. W. Heo, J. H. Lee, and J. J. Kim, Thin Solid Films **518**, 1234 (2009).

[27] V. Bornand and S. Trolier-Mckinstry, Thin Solid Films **370**, 70 (2000).

[28] C. Julien, M. A. Camacho-Lopez, L. Escobar-Alarcon, and E. Haro-Poniatowski, Mater. Chem. Phys. **68**, 210 (2001).

[29] A. Marcu, T. Yanagida, K. Nagashima, H. Tanaka, and T. Kawai, J. Appl. Phys. **102**, 016102 (2007) and other publications by the same group

Appendix B. Thin film post-processing

B.1 Introduction

It is not possible to achieve a desired stoichiometry and/or phase of the films by *in-situ* PLD of some materials systems. Non-stoichiometric transfer in chalcogenides often results from the loss of chalcogen atoms. In this case, *ex-situ* processing is used to fix the stoichiometry and/or to form the desired phase. Overall, post-processing is not desirable, because it adds extra complexity to the thin film fabrication process by introducing its own process variables and parameters on top of those of the PLD. Other disadvantage of the *ex-situ* processing is a guaranteed surface contamination with the atmospheric carbon-containing molecules and a possible surface oxidation during the transport of the samples from the deposition chamber to the post-processing location.

Some *ex-situ* processing techniques available at OSU include sealed-tube anneal (STA, Fig. A.1b), flowing gas anneal (FGA, Fig. A.1c) and rapid thermal anneal (RTA, similar to Fig. A.1c). The last two processes are used in industry and thus are commercially viable for the thin film preparation. All three processes are relatively fast (10 - 30 min at temperature), because the amount of the material in the thin film is very small. However, CVA and FGA require additional time for preparation of the experiment: evacuation and sealing in the case of CVA, and inert gas purge before and after FGA.

Post-processing techniques are often used to sulfurize/selenize metallic and oxide sample to form chalcogenide semiconductors. If the process starts with a metallic precursor, the resulting chalcogenide film usually has poor morphology, because of the large increase in volume of the film during the process.[1] If the process starts with oxide precursor, this problem is less evident, but in some cases it is not possible to convert the oxide into a chalcogenide for thermodynamic reasons. Specifically, the reaction will not occur if the total free energy of the products is larger than the total free energy of the reactants under any achievable experimental conditions. This is thought to be the case for inability to convert Zr-O and Sn-Zr-O thin film precursors into respectively ZrS_2 and $SnZrS_3$ films under flowing H_2S gas.[2] On the other hand, this is easily possible for the Sn-SnS conversion.

B.2 Flowing gas anneal

Flowing gas anneal process setup (Fig. A.1c) consists of a sample in alumina crucible enclosed in alumina tube through which the process gas flows. The tube is positioned in the furnace that heats up the crucible during the process. The most common process gases are H_2S, H_2Se, CS_2 and Ar/H_2 mixture. The former three gasses are toxic and have to be dealt with carefully. The main variables of the flowing gas process are temperature, time, and gas flow rate. Before the process, the tube has to be purged with inert gas to get rid of residual oxygen.

Process temperature defines the rate at which the process happens and can be up to 900 ^oC in the systems at OSU that belong to D. Keszler's group (Gilbert 011 and 18). There are two other limits on the process temperature posed by the materials: (i) it has to be below the materials synthesis temperature, so that the film does not decompose, and (ii) it has to be lower than the decomposition temperature of the H_2S or H_2Se gases if they are used, so that they do not decompose rapidly and S or Se solids do not precipitate on the samples. The flow furnaces at OSU may have an axial temperature gradient,[3] so the sample has to be small enough and positioned in the middle of the furnace.

Process time is important, but not crucial for this process, since the amount of material in the film is small compared to the amount of flown gas. Usually, 30 min are more than sufficient to complete the thin film reaction at a reasonably high temperature (~500 ^oC). Longer processing times may be required for lower process temperatures and for the reactions with powder samples. Process gas flow rate is also not crucial for the thin film process, since under any flowrate amount of material in the gas is in a large excess compared to the amount of material in a thin film. However, there is experimental evidence that the flow rate may influence the dynamics of the grain growth, and affect the grain size of the resulting sample.[1]

The quality of the seal of the furnace in the FGA process is crucial for the preparation of chalcogenides. The flow furnace at OSU is sealed by a set of o-rings, therefore the protection form oxygen is not ideal. One way to solve this problem is by using the getters (for example, Zr powder) positioned in the crucible. In principle, this should decrease the chances of the thin film oxidation, but on practice it does not help to prevent oxidation of Sn/Zr multilayers.[2]

Ideal flowing gas system for preparation of chalcogenides and other oxygen-sensitive materials would have a good vacuum seal and a vacuum pump attached to the tube. In this case

the tube could be evacuated before starting the flowing gas process, which would improve the purity of the atmosphere and speed up the experiment by avoiding long purge times. Such a system is not available at OSU, but the substrate heaters inside of the vacuum chambers can be used for this purpose. Using the Neocera PLD chamber as a flow-furnace with low oxygen partial pressure allowed converting insulating solution-deposited TiO_2:Nb films into conductive *n*-type samples under the Ar/H_2 flow.[2] This was not possible in conventional flowing gas furnace in Gilbert 011. The use of the PLD chambers for this purpose is limited to Ar/H_2 gas, since H_2Ch gasses are not allowed in there.

B.3 Sealed-tube anneal

Sealed-tube anneal (STA) process consists of a thin film sample and powder of the desired stoichiometry, encapsulated in evacuated glass tube (Fig. 1b). The film and the powder are spatially separated by ~ 2 cm. The tube is placed in a box furnace and heated, so that the thin film and the powder equilibrate. Temperature and time are two important variables of this process. The temperature is usually close to the synthesis temperature of the material, and the time is relatively short (~30 min), since the amount of material in thin film is small. Relatively large length of the tube (~10 - 20 cm) may lead to undesired directional transport of elements inside of the tube, because two ends of the tube can be at different temperature due to the non-uniformity of the heating profile of the a box furnace. Therefore it is very important to position the tube in the middle of the furnace and keep this position fixed for a set of experiments.

Other factors that may influence the final result are residual pressure in the tube and amount of powder material. The requirements on the vacuum vary between 10^{-3} and 10^{-7} Torr, depending on the material. Amount of powder used for a sealed tube anneal of the film is typically 0.05 – 0.5 g, but any measurable amount would be larger than the mass of the film. Excellent example of the tube-sealing experiments with small single crystals are given in literature.[4]

There are two tube-sealing stations available at OSU. The first one has a sliding seal between an o-ring and a glass tube and is equipped with a mechanical pump. The second one with the stationary seal between a rubber o-ring and a glass tube, has a rotating swage-lock seal, a vacuum guard and is equipped with a turbo-molecular pump. The residual pressure of the

second system is considerably lower (10^{-7} Torr) than for the first system (10^{-3} Torr), therefore it is better for preparation of chalcogenides, which has been shown before by preparation of Cu_3TaS_4 thin films and $SnZrCh_3$ powders. More details of these experiments as well as more detailed description of the tube sealing stations can be found in dissertations of other students.[3,5,6]

B.4 Rapid thermal anneal

Rapid thermal anneal is the third post-processing technique available at OSU. It is similar to the flow-furnace anneal (Fig. 1c), except the heating and cooling process occur much more rapidly. The variables of this process are temperature, time, type of gas, ramp rates and purge time. More details about the process and some experimental thin film processing results can be found elsewhere.[7]

References

---

[1] H. A. S. Platt, Ph. D. thesis, Oregon State University, 2010 and private communication

[2] A. Zakutayev, unpublished

[3] P. F. Newhouse, Ph. D. thesis, Oregon State University, 2008

[4] R. F. Brebrick and R. S. Allgaier, J. Chem. Phys. **32**, 1826 (1960).

[5] A. P. Richard, Ph. D. thesis, Oregon State University, 2010

[6] D. Harada, M. S. thesis, Oregon State University, 2010

[7] R. Kykyneshi, Ph. D. thesis, Oregon State University, 2007

Appendix C. Characterization techniques

C.1 Introduction

Large number of experimental characterization techniques is available for the OSU users. A particular combination of them would be used depending on the required information and on the goals of the project. The experimental methods discussed briefly below are described in more details in other dissertations.[1,2,3,4,5]

C.2 Structural properties

The most common way to initially access the structure of the prepared material is x-ray diffraction (XRD). Comparison of experimental x-rays diffraction patterns to the patterns found in databases[6] allows determination of the phase and crystal structure of a sample. Two XRD diffraction machines are available at the Department of Chemistry at OSU. The first one, Rigaku Rapid is used for the thin film samples and single crystals. The second one, Rigaku Miniflex is used mainly for powders and epitaxial thin films. Epitaxial thin films can also be characterized more completely on the Bruker machine available in the Mechanical Engineering department. More discussion about XRD techniques is available in literature.[7,8] and is a Ph.D. thesis by R. Kykyneshi.[1]

C.3 Chemical composition

Composition of the samples is routinely measured by Electron Probe Micro-Analysis (EPMA). This is an electron-in – x-ray-out technique which is similar to energy-dispersive x-ray (EDX). If properly used, EPMA gives much more accurate values of the composition compared to conventional EDX. Two CAMECA EPMA tools are available at CAMCOR at the University of Oregon (UO): SX100 and SX50.

Both bulk and thin film samples can be measured by EPMA. As with any technique that involves electrons, insulating samples can charge during the experiments and therefore have to be grounded to a sample-holder. This can be accomplished by carbon-coating them by arc-evaporation at CAMCOR or by depositing thin film samples on conductive substrates (for

example, doped Si). More information about EPMA technique and the local facilities can be found elsewhere.[9]

C.4 Microscopy

Optical microscopy is a fast and easy-to-use tool of initial thin films characterization. It allows accessing the morphology of the films, its crystallinity and quality of the surfaces. The Leica DMRM microscope available at OSU provides a magnification of up to 150x which allows resolving the features of about 500 nm size. The microscope can work in bright- and dark-field modes, and in transmission- or reflection, and has a polarization capability. The microscope is equipped with the CCD camera to store the obtained images on the computer using the Leica Application Suite.

When sub-visible-wavelength resolution is required, other microscopy techniques have to be used for imaging. For example, Atomic Force Microscopy (AFM) utilizes a sharp (~10 nm) tip that is dragged over the surface of a sample (contact mode) or oscillates next to it (tapping mode). The AFM resolution is limited by a size of a tip and by vibrations of the microscope. Digital Instruments Multimode microscope is available at OSU (Gilbert hall).

Other scanning microscopy techniques, such as scanning electron microscopy (SEM) and tunneling electron microscopy (TEM) are available at CAMCOR (UO). SEM has similar resolution to AFM, but it can give atomic-weight contrast (back-scattering mode) and compositional contrast (EDX), in addition to surface morphology. TEM has all the aforementioned capabilities and better resolution, but it requires dedicated preparation techniques, such as cutting with focused ion beam (FIB). Similar set of instruments is available at the OSU microscopy facility.

C.5 Optical measurements

Optical absorption measurement is a standard characterization procedure for a semiconducting or insulating thin film. Optical transmittance and reflectance are measured and the absorption spectrum is calculated from these data. The absorption spectrum reveals the optical band gap of the thin film sample, which is defined by a spectral position of the strong absorption onset.[10] In addition to the optical band gap, thin film thickness and refractive index

dispersion can be determined using this technique. They can be found by modeling measured transmittance and reflectance spectra with the optical interference fringes. Optical absorption can also be used to find the band gaps of powders from the diffuse reflectance.[11]

Three optical spectrometers are available at the lab of Dr. McIntyre at OSU. The first one is a grating spectrometer. This is a custom-built system which gives a lot of freedom for its tuning and modification, but a typical run on it takes ~ 15 min. The grating spectrometer is also equipped with the integrating sphere for diffuse reflectance measurements of the powder samples. More information about it can be found elsewhere.[5] The second spectrometer (OceanOptics+custom design) is based on the fiber optics and features much shorter data acquisition times (~ 5 sec). Short acquisition times allows for 2D mapping of the optical properties of the samples with the resolution limited by a beam size, and is also ideal for studying the optical properties of small, plate-shaped single crystals. The accessible spectral range of the first two spectrometers is 200 - 2500 um. More information on this spectrometer can be found elsewhere.[4] The third spectrometer (Filmetrix) also uses fiber optics and has short acquisition time, but its spectral range is limited to 400 - 900 nm. The advantage of this system is its software control and analysis system that allows for easy modeling of the optical spectra and quick extraction of thickness and refractive index.

Thickness and refractive index of the samples can also be measured using the Metricon prism-coupling instrument. The measurement technique is based on the wave guiding of monochromatic 634 nm light generated by HeNe laser through the film. The absorption of the sample should be low at the working wavelength and the surface of the sample should be clean and uniform. If optical methods cannot be used to determine the thickness of the samples (for example in the case of thick metal films or low-band gap semiconductors), surface profilometry is a good technique to use. Alpha-Step 500 surface profiler available at the ECE cleanroom can also be used to confirm the results of the thickness measurements by optical means.

Photoluminescence (PL) measurement is another optical technique commonly used to characterize the samples. High-energy photons (higher than the band gap of the material) excite electron-hole pairs which later recombine. This recombination may happen through radiative transitions with emission of the lower-energy photons. Some of these photons escape from the sample and can be detected. This process is called photoluminescence and can be used to find the

band gap of a sample, and to find the energy spacing between the defect levels in the band gap and the valence/conduction bands.

At OSU, PL can be measured at Dr. Keszler's lab. The PL instrumentation includes two monochromators for excitation and emission light, so this setup is quite tunable. The system utilizes Xe and deuterium lamps as excitation sources and a photomultiplier tube as a detector. The disadvantages of the system are low intensity of the excitation sources, long data acquisition times and the absence of good protection from the straying light. Alternatively, a system at Dr. Rorrer's lab (Chemical Engeneering) can be used to measure PL. This system features an intense 337-nm monochromatic light from a nitrogen laser and a CCD multi-array detector, so weak PL signals can be excited and measured in relatively short times.

In the case of weak PL it is very important to eliminate the sources of parasitic photoluminescence in the system, such as vacuum grease, double-sided scotch tape, paper *etc*. A simple way to mount a sample without these materials is by using the Teflon tape of carbon double-sided sticky tabs (often used to mount SEM samples).

Each of the aforementioned optical measurements can be performed at low temperature. For optical absorption measurements, this allows studying the temperature dependence of the band gap and excitonic effects. For the PL measurements, low temperature usually increases the intensity of the signal by reducing the nonradiative recombination rate. Low temperature is achieved by performing the measurements in an optical cryostat. The MMR optical cryostat available for use at Prof. Tate's lab allows stabilizing the temperature in the 80 – 400 K range. More information of construction and operation of the cryostat can be found elsewhere.[3]

C.6 Transport measurements

Electrical transport techniques routinely used to characterize the thin film samples are resistivity, Hall effect and Seebeck effect measurement. Hall effect and resistivity can be measured simultaneously using a LakeShore Cryotronics Hall Measurement System in up to 20 KG magnetic field. These two measurements allow for calculation of the type of charge carriers (electrons or holes), their concentration and mobility.[12] The Hall effect of thin film samples is measured using the van der Pauw configuration which in theory allows measuring samples of arbitrary shape. However, on practice, the samples are preferred to have a square shape, or even

better, be patterned using a special mask with a cross-like opening for these measurements. The disadvantage of the Lakeshore system at OSU is that it does not have a built-in temperature variability, but custom-built plug-in can be used to access high temperatures. Low temperature measurements can be performed in the aforementioned MMR cryostat.

Temperature-dependent resistivity (but not Hall effect) can also be measured in the custom-built system with in-line geometry of four contacts. The system is based on a He closed-cycle refrigerator (CCR) and can cool down to about 10 ^{o}K. This system can also be used to measure the temperature dependent Seebeck effect. The setup for this measurement consists of two blocks made of Cu. The temperature difference between the blocks is established by applying potential difference across the resistor embedded in one of the blocks. The difference in temperature is measured by a differential thermocouple and the absolute temperature of the sample is measured by a simple thermocouple.

One important step for any transport measurements is preparation of contacts. Typically, this is done by thermal evaporation of the metals on the surface of the sample. The thermal evaporators are available in Prof. Tate's labs as well as in the ECE celanroom. In addition, for Seebeck measurement it is important to clean the surfaces of the Cu blocks, which can be done using sand paper and organic solvents, and to protect the film from scratching by the electrodes, which can be done using a soft indium foil spacer. More details on the transport measurements can be found elsewhere.[1]

C.7 Photoelectron spectroscopy

Photoelectron spectroscopy is an experimental characterization technique used to characterize surface and interfaces of the materials. This method allows measuring local chemical environment of the atoms and determining the band alignment of the solids. Photoelectron spectroscopy will be discussed in more details in the next appendix.

References

[1] R. Kykyneshi, Ph. D. thesis, Oregon State University, 2007

[2] P. F. Newhouse, Ph. D. thesis, Oregon State University, 2008

[3] J. Kinney, senior thesis, Oregon State University, 2007

[4] J. Russel, M. S. thesis, Oregon State University, 2010

[5] L. Kilcher, senior thesis, Oregon State University, 2003

[6] http://www.icdd.com/

[7] B. D. Cullity and S.R. Stock, *Elements of X-Ray Diffraction*, 3rd ed. (Prentice Hall, 2001).

[8] M. Birkholz, *Thin Film Analysis by X-Ray Scattering* (Wiley-VCH, 2006).

[9] http://www.uoregon.edu/~epmalab/

[10] J. I. Pankove, *Optical Processes in Semiconductors* (Courier Dover Publications, 1975).

[11] S. Shionoya and W. H. Yen, *Phosphor Handbook*, (CRC-Press, 1997).

[12] D. K. Schroder, *Semiconductor Material and Device Characterization*, (John Wiley and Sons, 2005)

Appendix D. Photoelectron spectroscopy

D.1 Introduction

Photoelecron spectroscopy (PES) experiments discussed in this work were performed at Darmstadt University of Technology under the supervision of Andreas Klein in the surface science division led by Wolfram Jaegermann. This work was supported by a stipend from the SFB 595 fellowship program.

D.2 Equipment

PES is a photon-in electron-out technique. It allows for analysis of composition, chemical bonding and electronic structure of surfaces and interfaces.[1] A typical laboratory-scale PES setup is schematically shown in Fig. D.1a. PES chamber is usually equipped with a source of x-ray- and/or ultraviolet photons, electron analyzer and detector enclosed in a vacuum chamber. Often the PES systems also include surface-preparation modules, such as reactive ion etch and/or plasma source. Since the photoelectrons have very short inelastic mean free path (0.5-10 nm),[2] PES measurements are very sensitive to any surface contamination. Therefore, all PES chambers have to provide ultra-high vacuum, so they are often equipped with load locks.[3]

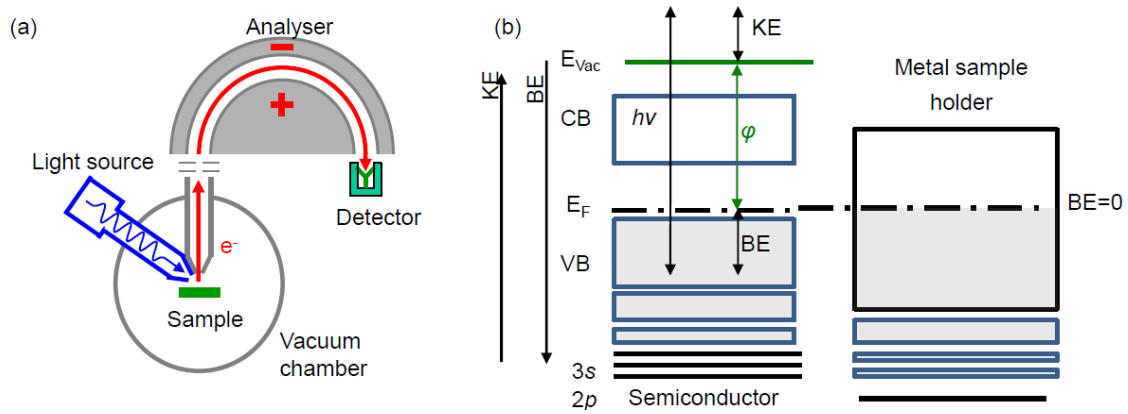

FIG. D.1 (a) A photoelectron spectroscopy (PES) system. (b) PES energy diagram (adopted from A. Klein)

D.3 Energy scale

Fig. D.1b shows the energy level diagram of a semiconducting sample in contact with the PES metallic sample holder. The photoelectrons that escape from the sample are counted as a function of their kinetic energy (KE). In PES, zero energy is defined to be at the Fermi level (E_F) of the apparatus. The E_F of the sample equilibrates with that of the PES instrument when they are brought into the contact through a metallic sample holder. The calibration of the instrument is typically done using the core level spectra or the Fermi edges of the clean surfaces of noble metals.[1] The reference XPS levels of atoms in various materials can be found in reference books[3] and electronic databases.[4]

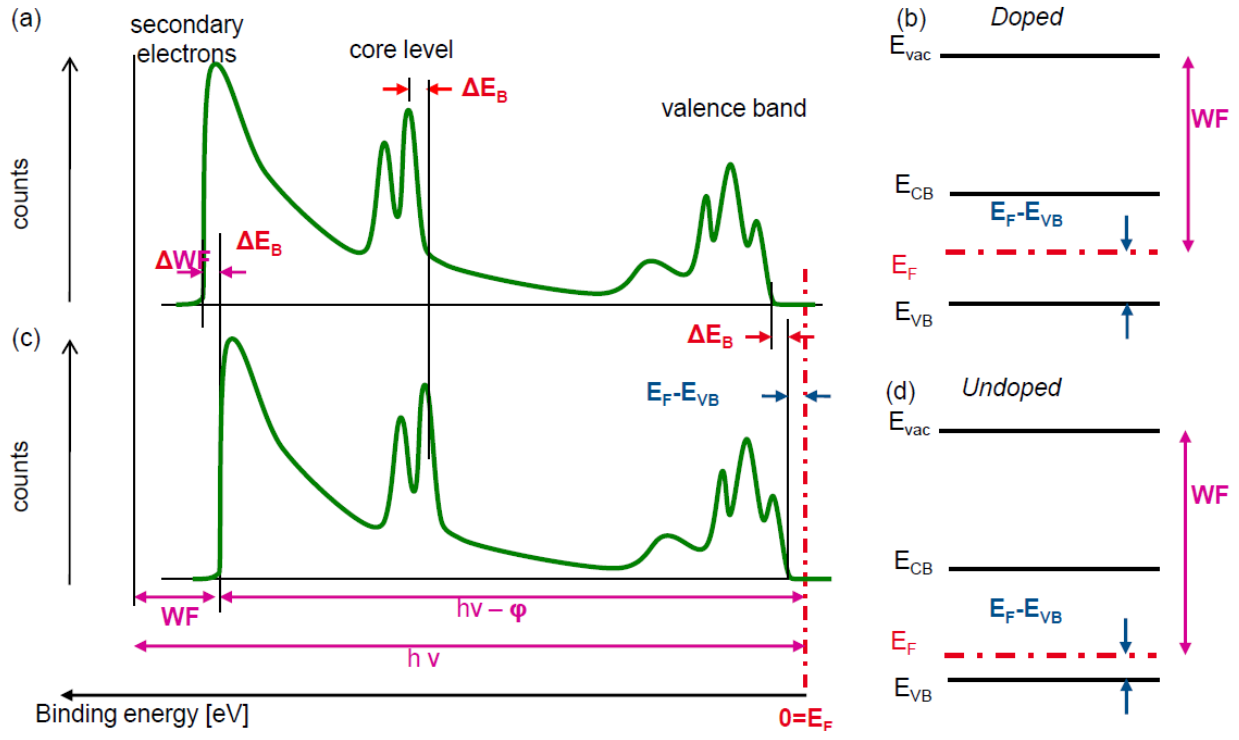

FIG. D.2 (a) Hypothetical PES spectra of the same sample with different Fermi levels and (b) corresponding band diagrams (adopted from A. Kelin)

Binding energy (BE) is more commonly used as a scale for the PES (Fig. D3a). The BE and the KE are related by the equation $h\nu$ = BE + WF + KE, where $h\nu$ is energy of incident photons, and WF is the work function of the material.[2] Therefore, by tuning the analyzer to

different KE one can access a range of BE. Theoretically, for a fixed monochromatic light source of the energy *hv*, the highest accessible BE is defined by *hv*-WF, when KE = 0. On practice, photoelectrons that have KE close to 0 are very slow and have a high probability of interaction with the matter. This interaction creates secondary electrons which show up as ~1/BE background of the PES signal (Fig. D.2a). The secondary electron edge (SEE) at BE=*hv*-WF is used to find the WF of the material. At the low BE, the PES spectra reflect the density of states at the valence band (VB). Having both the WF and the VB BE (E_F position above the VB), and knowing the band gap (E_g) one can plot a complete band diagram for a surface of a semiconductor (Fig. D.2b). In bulk, the band diagram may look different from the surface. If E_F in the semiconductor changes, for example due to doping, all the feature of the spectra will shift in parallel, as schematically shown in Fig. D.2c and Fig. D.2d.

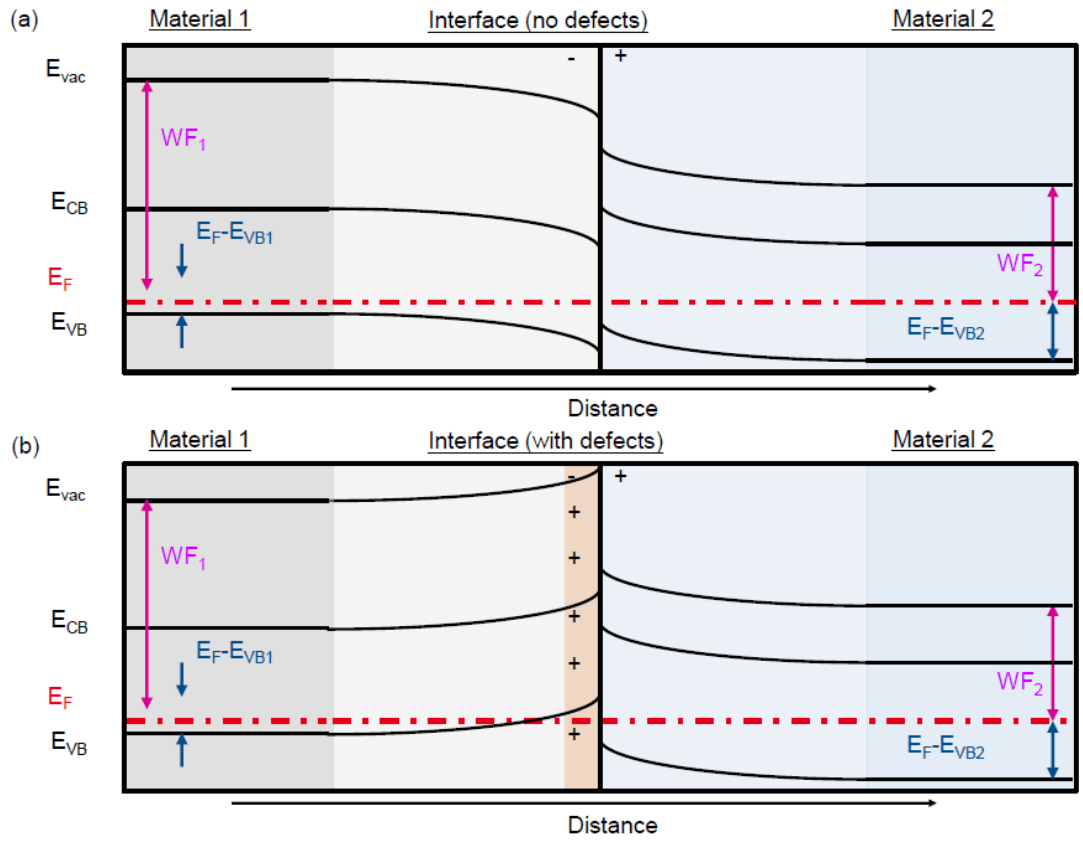

FIG. D.3 Examples of the band bending at the interfaces (a) with and (b) without the interface dipole

D.4 Band bending

Important concept related to PES is band bending (Fig. D.3). Band bending (Fig. D.3a) reflects the spatial variation of the free charges and often occurs at the interfaces with other material or at the interfaces with air/vacuum at the surface of the sample. However, the spatial charge redistribution does not always result in a wide depletion region. The charges can also be trapped at the localized defect states deep in the band gap of a semiconductor and form a local interface dipole (Fig. D.3b). Band bending is important phenomenon for the formation of the interfaces of the thin film optoelectronic devices.[5]

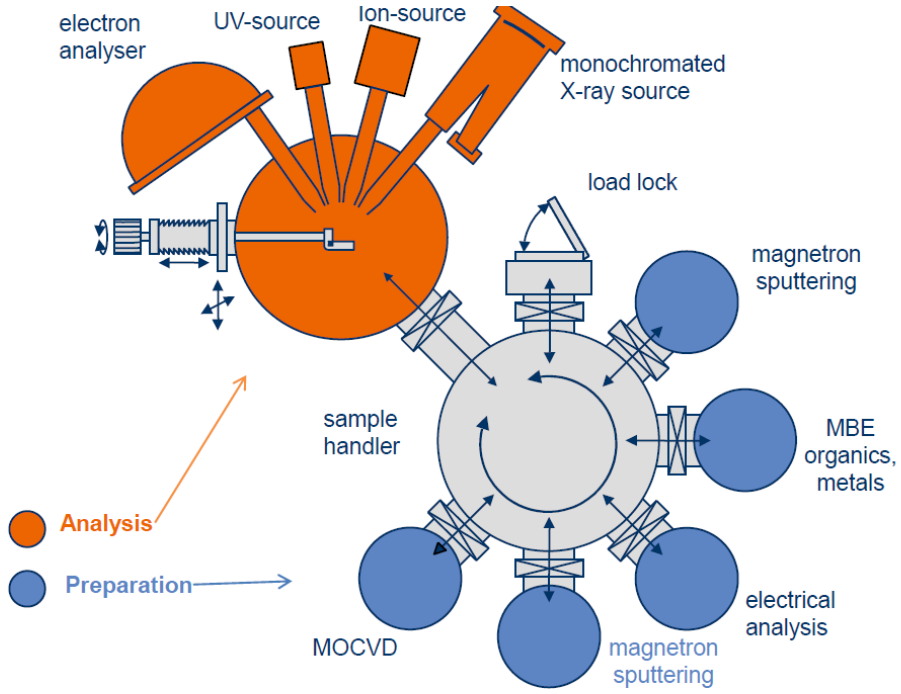

FIG. D.4 Schematic drawing of a cluster-tool (adopted from A. Kelin)

D.5 Surface sensitivity

PES is a surface-sensitive technique, so it allows studying surfaces and interfaces of the materials. High surface sensitivity also means that any surface contamination will affect the results. Therefore, proper surface preparation is crucial for successful PES experiments. Ideally, the sample should be prepared and studied without breaking the vacuum. This is often done in

cluster tools, as schematically shown in Fig. D.4. A typical cluster tool usually consists of multiple deposition chambers, a PES chamber, a surface preparation chamber, all connected by a vacuum transfer chamber. PES experiments reported in this work have been performed in a DAISY-SOL (Darmstadt Integrated System for SOLar energy research) cluster tool.[6] If the cluster tool is not accessible, surfaces protection and/or cleaning techniques have to be used, such as portable vacuum chambers, capping layers,[7] and scotch-tape protection of the surface.[8]

D.6 Interfacing experiments

A typical PES interfacing experiment is schematically shown in Fig. D.5. The interfacing experiment consists of the iterative cycles of deposition of a material on the substrate and PES measurement (Fig. D5a). The cycles are performed until no bending of the electronic states is observed (Fig. D.5a). At this point, the distance between the E_F and the VB (CB) defines the interface Schottky barrier for the holes (electrons), and the distance between the VB of two materials defines the VB offset.[9] CB offsets cannot be directly probed with PES, but one can calculate them knowing the band gaps of two materials.

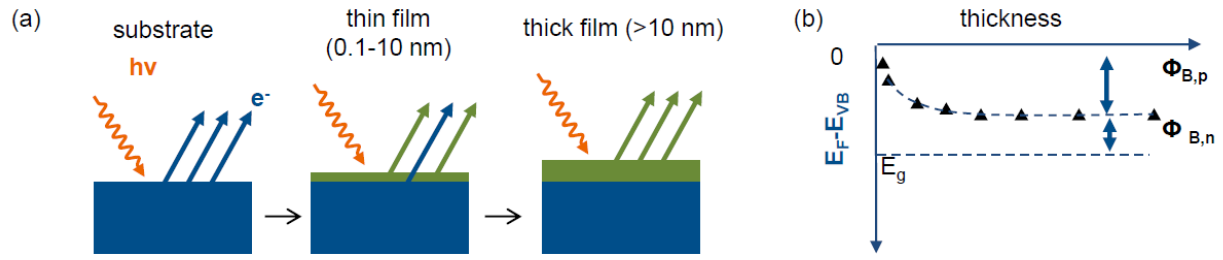

FIG. D.5 (a) Interfacing experiment sequence. (b) Determination of the Schottky barrier heights from the PES interacting experiment data. (adopted from A. Kelin)

The top-down approach to interfacing experiments is to prepare the layered sample and then sputter the top layer using the Ar ion beam and monitoring the shift of the core levels. However in many cases sputtering leads to changes of the surface composition and electronic structure, so this method is less favorable than the bottom-up approach described above. In the case of sputtering, workfunctions and hence vacuum level shifts cannot be reliably measured due

to the surface modification. UPS measurements used to determine the workfunction are much more surface sensitive than the XPS measurements used to calculate the band offsets. The top-down sputtering approach to the interfacing experiment is available at the Surface Analytical Facility at CAMCOR at UofO.

References

[1] A. Klein, T. Mayer, A.Thissen and W. Jaegermann, Bunsen-magazin **10,** 124 (2008)

[2] S. Tanuma, C.J. Powell, and D.R. Penn, Surface and Interface Analysis **17,** 911 (1991).

[3] J. F. Moulder, W.F. Stickle, P.E. Sobol, and K.D. Bomben, *Handbook of X-ray Photoelectron Spectroscopy*, (Physical Electronics, Inc., Eden Prairie, 1995)

[4] NIST X-ray Photoelectron Spectroscopy Database,http://srdata.nist.gov/xps/

[5] S. M. Sze, *Physics of Semiconductor Devices* (John Wiley & Sons, New York, 1981)

[6] J. Fritsche, A. Klein, and W. Jaegermann, Adv. Eng. Mater. **7,** 914 (2005).

[7] T. Schulmeyer, R. Hunger, A. Klein, W. Jaegermann, and S. Niki, Appl. Phys. Lett. 84, 3067 (2004).

[8] D. Johnson, private communication

[9] W. Mönch, *Electronic Properties of Semiconductor Interfaces*, (Springer-Verlag, Heidelberg, 2003)

Appendix E. Density functional theory calculations

E.1 Introduction

Density functional theory (DFT) is a powerful method to study the electronic structure of the materials. DFT is an *ab-initio* method, because it is based on basic principles of quantum mechanics and the input information is only the position of atoms (and the unit cell size for a solid). This method allows finding, self-consistently, the total free energy of the electronic system.[1,2] DFT is commonly used to calculate the thermodynamic properties of the matter (energetic of materials phases, defects, surfaces etc.) and its electronic structure (band structure, density of states, charge density, optical absorption *etc.*). DFT has two most-common approximation: local density approximation (LDA) and a number of general gradient approximations (GGA). The most widely used GGA is Perdew-Burke-Ernzerhof (PBE) GGA.[3] Other methods, such as GW take into account the self-interaction many-body effects which allows more accurate calculation of the properties of excited electronic states. For example, the GW method can correctly predict the band gaps of semiconductors whereas DFT fails to do so.[4] On the other hand, GW is currently not self-consistent, more computationally expensive and require results of the other methods to start the calculation.

E.2 Implementation

DFT algorithms are implemented in numerous software packages. Several of them are available for OSU users, such as Wien,[5] Flair,[6] and VASP.[7] Most of the results reported in this work have been obtained using VASP code. This package is much faster than Wien of Flair programs, because it utilizes the projector-augmented-wave (PAW) method with pseudopotentials. This means that only valence electrons are considered explicitly, and core electrons are replaced by an effective potential. GGA, LDA and GW are all implemented in VASP.

A big advantage of the VASP code is its simplicity and clarity of the input file system. There are 4 input files. The first file, POSCAR, contains information about the size and shape of the unit cell and positions of the atoms. This information can be found from a .cif file for a certain material found in crystallographic databases.[8] The second file, KPOINTS, defines the

mesh of *k*-points on which the calculation will be performed. The third file, POTCAR, contains information about pseudopotentials of the atoms in the calculation. The fourth file, INCAR, includes all the computational details. The output of the VASP consists of number of files. The most general and comprehensive output file, OUTCAR contains most of the information that can also be found in other output files in a more handy form. More information about the VASP code and its files can be found in the VASP manual.[9]

E.3 Defect computational details

Density functional theory can be used to calculate defect and carrier concentrations in a material. As a starting point of the calculation, defect formation enthalpies are obtained using the supercell approach.[10] A supercell consists of a few unit cells of a material with a defect in one of them. The size of the supercell is limited by the available computer memory, because the DFT calculations scale with the number of atoms (and with the number of *k*-points too). At present, the supercell with less than ~128 atoms can be calculated on the computer cluster of Dr. Schneider and Dr. Roundy at OSU.

One needs to check the convergence of the results with respect to the size of the supercell, the number of *k*-points used, and the cut-off energy (the latter is less important). Equilibrium DFT crystal lattice parameters have to be used, and they are different for GGA and for LDA. Within the defect calculation all the atoms must be allowed to relax without any symmetry constrains.

E.4 Defect computational corrections

Four corrections have to be applied to the DFT supercell calculation results to minimize the effect of the final size of the supercell, as described in mathematical terms in literature.[11]

Potentials of the supercell with- and without the defect have to be aligned using semi-core states projected on the atom far from the defect as a reference (RWIGS and LORBIT flags in the INCAR file). Alternatively, an average potential on the interstitial site far from the defect can be used (LVTOT flag in the INCAR file). Both of these numbers can be calculated using VASP, and more details are discussed in the manual.[9]

LDA and GGA chronically underestimates the band gaps of semiconductors and misplaces the transition metal atom levels, which affects the defect calculation results. A good approach do deal with both of these problems is to use LDA+*U* or GGA+*U* supercell calculations. *U* parameter in DFT+*U* calculations corresponds to the energy cost to place two electrons in one level in solid state materials (so called, Hubbard *U*). The choice of the *U* parameter in DFT+*U* is such, that the bandgap and the peaks in the density of states match the experimental or GW bandgap and the photoelectron spectroscopy results, respectively. If the DFT+*U* calculations were not performed, conduction band minimum (CBM) and not fully charged donor-like states have to be shifted up.

Additional energy of the electrons that comes from the defect band formation and filling has to be subtracted from the calculation result. This is unphysical for modeling the dilute defect concentrations. Band filling can be done using partial weights of the *k*-points from the IBZKPT file and the electron partial occupancies and eigenenergies from the OUTCAR file.

The image charge correction[12] has to be performed only if the concentration of defects in a supercell is higher than the equilibrium concentration of defects from the self-consistent thermodynamic simulations or from the experiment.

E.5 Chemical potentials

The algorithm described below closely follows the literature.[11] The aim of this explanation is to present the calculations in a more extended form and give an experimentalist's point of view on them.

To calculate formation enthalpies of defects, it is necessary to know the chemical potentials of the atoms. Chemical potential $\mu_a{}^M$ of an atom *a* in a compound *M* is smaller than the chemical potential $\mu_a{}^O$ of the same atom *a* in the elemental material *O*:

$$\mu_a{}^M = \mu_a{}^O + \Delta\mu_a = E_H{}^O + \Delta\mu_a \qquad \text{(E1)}$$

where $E_H{}^O$ is the total free energy per atom calculated using DFT and the difference $\Delta\mu_a$ <0 may vary within the range defined by 2 types of conditions:

(i) The sum of $\Delta\mu_a$ should be equal to the formation energy of the compound *M* per formula unit $\Delta H_F{}^M$:

$$\sum_a m_a{}^M \Delta\mu_a = \Delta H_F{}^M \quad \text{(E2)}$$

(ii) The sum of $\Delta\mu_a$ should be smaller than the formation energy of the impurities *I* per formula unit $\Delta H_F{}^I$:

$$\sum_a m_a{}^I \Delta\mu_a > \Delta H_F{}^I \quad \text{(E3)}$$

Condition (i) assures the formation of compound *M* and conditions (ii) restrains the formation of secondary phases. Formation energy per formula unit (Eq. 2-3) are calculated using:

$$\Delta H_F = E_H - \sum_a m_a \mu_a{}^O \quad \text{(E4)}$$

where m_a is the number of atoms of type *a*, and E_H is the total free energy per formula unit calculated using DFT. For an elemental compound with 1 atom per formula unit $\Delta H_F{}^O = \mu_a{}^O$.

E.6 Defect formation enthalpies

Formation enthalpy $\Delta H_{D,q}$ of a defect *D* in a charge state *q* depends on (i) the difference in the total free energies of the host material with and without the defect $E_{D,q}$-E_H (ii) the number n_a of atoms *a* removed from the host to create the defect and their chemical potential in the host $\Delta\mu_a$ with respect to that in the elemental substance $\mu_a{}^O$, and (iii) the Fermi level of the electrons E_F with respect to the energy of the valence band E_V:

$$\Delta H_{D,q}(E_F) = (E_{D,q} - E_H) + \sum_a n_a(\mu_a{}^O + \Delta\mu_a) + q(E_V + E_F) \quad \text{(E5)}$$

Parameter $E_{D,q}$ was the total free energy of the supercell calculation with *q* extra (missing) electrons for the acceptor (donors)-like defects. Parameters E_V and E_H were determined from the reference supercell calculation without the defects. The value of the parameter $\mu_a{}^O$ and range of the variable $\Delta\mu_a$ was obtained as discussed in section IIIA. Therefore, the only unknown variable of Eq.1 was E_F. The range of the variation of E_F is limited by the pinning Fermi level $E_F{}^{pin}$ at which $\Delta H_{D,q} = 0$ and the material does not exist.

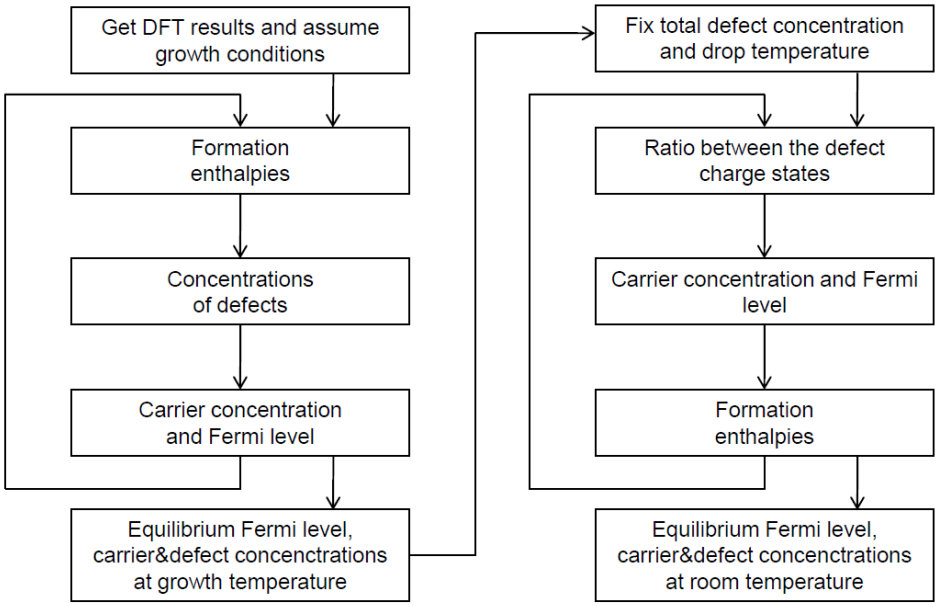

FIG. E.1 Algorithm of self-consistent thermodynamic simulations.

E.7 Thermodynamic simulations

The algorithm of self-consistent thermodynamic simulations is shown schematically, in Fig. E.1, and is discussed in more details below. The self-consistent thermodynamic simulations are used to obtain room-temperature equilibrium Fermi levels and corresponding concentration of free charge carriers of the material at synthesis temperature and room temperature. To start self-consistent thermodynamic simulations, it is assumed that $E_F = 0$ (*i. e.* Fermi level is at the valence band maximum). Concentration of defects $c_{D,q}$ on a site N_D at T_S exponentially depends on their formation enthalpy:

$$c_{D,q}(E_F, T) = N_D \exp[-\Delta H_{D,q}(E_F)/k_B T] \quad \text{(E6)}$$

Therefore, only the defects with the lowest $\Delta H_{D,q}$ will be present the material in appreciable quantities. Moreover, according to the charge neutrality principle only charged states of these lowest-energy defects will affect the concentrations of free holes p and electrons n:

$$p(E_F, T) - n(E_F, T) = \sum_{D,q} qC_{D,q}(E_F, T) \quad \text{(E7)}$$

For a p-type semiconductor $p - n \approx p$, so using the Fermi-Dirac distribution, E_F can be found numerically from the integral:

$$\int_{-\infty}^{E_V} \frac{D_{VB}(E)}{1+\exp[(E-E_F)/k_BT]}\,dE = p(E_F,T) \qquad \text{(E8)}$$

where $D_{VB}(E)$ is the number of states in the valence band per unit volume per unit energy (density of states) calculated using DFT. Similar relationships apply to an *n*-type semiconductor. Resulting E_F differs from the initial guess, so it is fed back into Eq.1 and Eq. (2-4) are repeated until the equilibrium Fermi level ${E_F}^{eq.ST}$, concentrations of defects ${c_{D,q}}^{eq.ST}$ and free holes $p^{eq.ST}$ are obtained self-consistently with the accuracy of better than 1 meV.

The total number of defects of a certain kind at room temperature T_R is the same as at the synthesis temperature because of kinetic barriers that arise due to non-adiabatic nature of a typical experimental cooling process. Therefore, at T_R the concentration of a defect D in a charge state q' is:

$${C_{D,q'}}^{RT}({E_F}^{RT},T_R) = \sum_q C_{D,q}^{eq.ST} \times \frac{\exp[-\Delta H_{D,q}({E_F}^{eq'})/k_BT_R]}{\sum_q \exp[-\Delta H_{D,q}({E_F}^{eq})/k_BT_R]} \qquad \text{(E9)}$$

Eq. 5 and Eq. (7-9) were solved self-consistently to find equilibrium Fermi level ${E_F}^{eq.RT}$, concentrations of defects ${c_{D,q}}^{eq.RT}$ and free holes $p^{eq.RT}$ at room temperature T_R, using the algorithm described above. (Fig. 7)

E.8 Defect transition levels

Transition level of defect D between charge sate q and q' is defined as E_F at which $\Delta H_{D,q} = \Delta H_{D,q'}$:

$${\varepsilon_D}^{q/q'} = \frac{E_{D,q} - E_{D,q'}}{q'-q} - E_V \qquad \text{(E10)}$$

where $E_{D,q}$ and $E_{D,q'}$ are the corresponding corrected defect formation enthalpies. Defect transition level ${\varepsilon_D}^{q/q'}$ affects the concentration of defects through Eq. 9, and hence concentration of free holes (Eq. 5) and Fermi level (Eq. 6). For example, acceptors with shallow transition level generate more free holes and push the Fermi level towards the valence band.

E.9 Defect complexes

Defect complexes consist of the point defect located close to each other. Defects of the opposite charge can gain energy by transferring electrons and forming neutral defect complexes. The energy cost δH_{DC} to form a defect complex *DC* is:

$$\delta H_{DC} = \Delta H_{DC} - \sum_{D} \Delta H_{D,q} \tag{E11}$$

Additional energy gain to form a defect complex comes from ordering of the defect complexes. For example, in $CuInSe_2$ and related chalcopyrites, ordered arrays of the defect complexes leads to formation of ordered defect compounds.[10]

References

[1] P. Hohenberg and W. Kohn, Phys. Rev. **136**, B864 (1964).

[2] W. Kohn and L. J. Sham, Phys. Rev. **140**, A1133 (1965).

[3] J. P. Perdew, K. Burke, and M. Ernzerhof, Phys. Rev. Lett. **77**, 3865 (1996).

[4] M. Shishkin, G. Kresse, Phys. Rev. B **75**, 235102 (2007).

[5] P. Blaha, K. Schwarz, G. Madsen, D. Kvasnicka, J. Luitz, WIEN2k, An Augmented Plane Wave + Local Orbitals Program for Calculating Crystal Properties (Karlheinz Schwarz, Techn. Universität Wien, Austria), 2001.

[6] M. Weinert, G. Schneider, R. Podloucky, J. Redinger, J. Phys.: Condens. Matter **21**, 084201 (2009).

[7] G. Kresse, J. Furthmüller, Phys. Rev. B **54**, 11169 (1996).

[8] http://www.icdd.com/

[9] http://cms.mpi.univie.ac.at/vasp/vasp/vasp.html

[10] S. B. Zhang, S.-H. Wei, A. Zunger, and H. Katayama-Yoshida, Phys. Rev. B **57**, 9642 (1998).

[11] C.Persson, Y.-J. Zhao, S. Lany, and A. Zunger, Phys. Rev. B **72**, 035211 (2005).

[12] G. Makov and M. C. Payne, Phys. Rev. B **51**, 4014 1995